Master's thesis

NTNU
Norwegian University of Science and Technology
Faculty of Natural Sciences
Department of Physics

Maxim Andresen Tjøtta

Superconductive transport in curved thin film ferromagnets

Diffusive superconductor - ferromagnet proximity systems under geometric curvature in 2 dimensions

Master's thesis in Physics (MScPhys)
Supervisor: Senior Researcher Sol H. Jacobsen
May 2024

NTNU
Norwegian University of
Science and Technology

Maxim Andresen Tjøtta

Superconductive transport in curved thin film ferromagnets

Diffusive superconductor - ferromagnet proximity systems under geometric curvature in 2 dimensions

Master's thesis in Physics (MScPhys)
Supervisor: Senior Researcher Sol H. Jacobsen
May 2024

Norwegian University of Science and Technology
Faculty of Natural Sciences
Department of Physics

NTNU
Norwegian University of
Science and Technology

Abstract

In this thesis, we are looking at the theoretical treatment of superconductor - ferromagnet (SF) and superconductor - ferromagnet - superconductor (SFS) proximity systems within a curved geometry. The systems considered are diffusive and treated in the quasiclassical approximation. We demonstrate the generation of long-range triplets (LRTs) in SF systems with a Rashba-Dresselhaus spin-orbit field in the xy-plane and in systems with a spin-orbit field in the z-direction. We then introduce the curvilinear formalism and discuss the potential for generating LRTs with geometric curvature. The system of an SF curved nanowire is solved numerically and demonstrated to generate LRTs. A curvature induced 0-π transition for an SFS nanowire is demonstrated numerically as well. We then give an introduction to the differential geometry of two dimensional (2D) surfaces, where an expression for the Christoffel symbols of a surface embedded in 3D space is derived. Several 2D surfaces are treated analytically within this formalism, including a *tunnel* surface, a *boomerang* surface and a Gaussian bump. The analytical results for these surfaces predict the generation of LRTs in these systems. The formalism for 2D curved surfaces is shown to work well for the numerical treatment of SF- and SFS- proximity systems. We plot the density of states of an SF tunnel system and show that this system is qualitatively equivalent to the 1D nanowire. For the SFS boomerang, we see indications that the charge current tends to be denser along the inner curvature of the system. We also demonstrate the possibility of having a vortex in the charge current for a boomerang SFS system, which could be indicative of a superconducting vortex.

Sammendrag

I denne avhandlingen tar vi for oss en teoretisk behandling av superleder-ferromagnet (SF) og superleder-ferromagnet-superleder (SFS) proksimitetssystemer for en krummet geometri. Systemene som undersøkes er diffusive og behandles med en kvasiklassisk tilnærming. Vi demonstrerer genereringen av tripletter med lang rekkevidde (LRTer) i SF-systemer med et Rashba-Dresselhaus spinn-bane-felt i xy-planet og i systemer med spinn-bane-felt i z-retningen. Vi introduserer deretter den kurvilineære formalismen og diskuterer muligheten for å generere LRTer med geometrisk krumning. Systemet for en krummet SF nanoledning løses numerisk, og det vises at systemet kan gi opphav til LRTer. En krumningsindusert 0-π-overgang for en SFS nanoledning demonstreres også numerisk. Deretter introduseres differensialgeometrien for todimensjonale (2D) overflater, hvor vi utleder Christoffel-symbolene for en overflate plassert i tre dimensjoner. Flere 2D overflater behandles analytisk. Overflatene som behandles er en *tunnel*-overflate, en *boomerang*-overflate og en Gaussisk hump, og vi utleder analytiske grunnlag for at disse overflatene kan generere LRTer. Formalismen for 2D krummede overflater vises å fungere bra for numeriske utregninger for SF- og SFS- systemer. Vi plotter tilstandstettheten for et SF tunnel-system og viser at dette systemet er kvalitativt ekvivalent til en 1D nanoledning. For SFS boomerang-systemet ser vi indikasjoner på at ladningstrømmen er tettere langs den indre krumningen. Vi demonstrerer også muligheten for å ha virvling i ladningsstrømmen for et boomerang SFS-system, noe som kan indikere muligheten for superledende virvlinger.

Preface

This project was written as a 60 credits master thesis, at the end of a two years Master in Physics (MSPHYS) at the Norwegian University of Science and Technology (NTNU). Throughout this project I have learned several new formalisms, a new programming language and gained insight into a whole new area of research. I have learned more in a year than I thought possible. This would not be possible without the aide of several great people, and some special thanks are therefore in order. First of all I would like to thank my supervisor Sol Jacobsen for welcoming me into her research group and introducing me to the world of curvature and superconductors. Your enthusiasm for this area of research has definitely rubbed off on me, and I am excited to follow the development of curvature in SF system in the years to come. Secondly, I would like to thank Kjell Heinrich for being a good friend and study partner throughout the writing of this thesis. I am very grateful for all our interesting discussions on physics and the company you have provided during this year. Next, I would like to thank Morten Amundsen and Henning Hugdal for their invaluable input to my research during our discussions with Sol's research group. I would also like to thank QuSpin center of excellence for providing a welcoming and enjoyable environment for me to write my thesis, and Sigma2 AS for letting me use their supercomputer Saga for my computational tasks. Last, but not least, I would like to thank my partner Tina Heier for endlessly cheering me on during the highs and lows of my work. This work would not be possible without you.

Notation and units

This thesis follows the usual convention of mathematical notation for the most part. Vectors are denoted by bold notation, $\boldsymbol{v}$, and unit vectors are denoted by a hat and bold notation, $\hat{\boldsymbol{v}}$, in order to not confuse unit vectors with operators and matrices. Partial derivatives are often simplified as $\frac{\partial v}{\partial x} = \partial_x v$, and the gradient is denoted by $\nabla = \hat{\boldsymbol{x}}_1\partial_1 + \hat{\boldsymbol{x}}_2\partial_2 + \hat{\boldsymbol{x}}_3\partial_3$. The Einstein summation convention is thoroughly used throughout this thesis, meaning that repeated indices should be summed over, i.e. $\nabla = \sum_{i=1}^{3} \hat{\boldsymbol{x}}_i\partial_i = \hat{\boldsymbol{x}}_i\partial_i$.

Matrices are denoted by their size. 2×2 matrices are underlined, $\underline{A}$, 4×4 matrices are hatted, $\hat{A}$, and 8×8 matrices are checked, $\check{A}$. Sums or products between matrices of different sizes should be interpreted as taking the Kronecker product between the matrix with the lowest dimensionality and the fitting identity matrix, I, before doing the operation. For example, $\check{A} + \hat{B} = \check{A} + \underline{I} \otimes \hat{B}$ and $\check{A}\underline{B} = \check{A}(\hat{I} \otimes \underline{B})$. The the matrices

$$\underline{\sigma}_x = \begin{pmatrix} 0 & 1 \\ 1 & 0 \end{pmatrix}, \quad \underline{\sigma}_y = \begin{pmatrix} 0 & -i \\ i & 0 \end{pmatrix}, \quad \underline{\sigma}_z = \begin{pmatrix} 1 & 0 \\ 0 & -1 \end{pmatrix}, \tag{1}$$

denote the three Cartesian Pauli matrices in spin space, and the matrices

$$\underline{\tau}_x = \begin{pmatrix} 0 & 1 \\ 1 & 0 \end{pmatrix}, \quad \underline{\tau}_y = \begin{pmatrix} 0 & -i \\ i & 0 \end{pmatrix}, \quad \underline{\tau}_z = \begin{pmatrix} 1 & 0 \\ 0 & -1 \end{pmatrix}, \tag{2}$$

denote the Cartesian Pauli matrices in Nambu space. The Pauli matrices in spin space can be written compactly by using the Pauli spin-vector $\underline{\boldsymbol{\sigma}} = \hat{\boldsymbol{x}}_i\underline{\sigma}_i$. The Pauli matrices in Nambu space are sometimes written in their 4×4 extension, defined by $\hat{\tau}_i = \underline{I} \otimes \underline{\tau}_i$. We define the commutator between two quantities A and B as $[A, B] = AB - BA$, and the anticommutator as $\{A, B\} = AB + BA$.

In this thesis, we use the second quantization formalism of quantum mechanics. In this formalism, we define c_i and $c_i^\dagger$ as the annihilation and creation operators for electrons with quantum numbers i, respectively. † denotes the adjoint operator. From these operators, we define the annihilation field operator as $\psi_\sigma(\boldsymbol{r}, t) = \sum_i \phi_i(\boldsymbol{r})c_i(t)$ and the creation field operator as $\psi_\sigma^\dagger(\boldsymbol{r}, t) = \sum_i \phi_i^*(\boldsymbol{r})c_i^\dagger(t)$. Here, $\phi_i(\boldsymbol{r})$ denotes the single particle wavefunction, and * denotes complex conjugation. The average of an operator A is denoted by $\langle A \rangle$.

We use natural units in this thesis. This means that the following fundamental physical constants reduce to unity [1]

$$\hbar = c = \epsilon_0 = \mu_0 = k_B = 1. \tag{3}$$

Here, c denotes the speed of light in vacuum, $\hbar$ denotes the reduced Planck's constant, k_B denotes Boltzmann's constant, and μ_0 and ϵ_0 denote the vacuum permeability and permittivity, respectively. This system of natural units simplifies most of the expressions in this thesis, and makes interpretation of results more intuitive.

Contents

1 Introduction

Superconductor - ferromagnet (SF) proximity systems have the potential to change the way we process and manipulate information in electronic systems. The ferromagnet's ability to transport spin has already changed the way we process information [2]. In contact with a superconductor, the ferromagnet's ability to transfer information through spin is altered, and can be enhanced significantly. The reason for this is the so-called *proximity effect*, an effect through which the particles, and thus some of the properties, of the superconductor may leak through the SF interface and into the ferromagnet. Over the last decade, research has been conducted on these systems in various configurations and contexts, in order to enhance the transport properties or draw new mechanisms from the systems. In this context, this thesis is the first theoretical study of the effects of curvature on SF proximity systems in two dimensions (2D). Our expectations are that 2D curvature has the potential to bring forth new and exciting mechanics from SF systems. The main goal of this thesis is therefore to develop a formalism that allows us to describe diffusive transport of superconductive correlations in 2D curved ferromagnets. In order to do this, we first have to understand several underlying concepts. This thesis assumes a basic knowledge of quantum mechanics, especially the second-quantization formalism, and the microscopic theories of ferromagnets and superconductivity. In this chapter, we briefly explain the key mechanics behind ferromagnets, superconductivity and the proximity effect, and mention some technologies developed from these concepts. We then go on to introduce the effect of curvature on these systems, and motivate why we want to look at curvature in two dimensions.

This thesis is structured to give a progressive introduction to the world of superconductive transport in ferromagnets. The main tool used in this analysis is the Usadel equation, a diffusion-like equation for the quasiclassical Green's function in diffusive systems. Because of this, an introduction to the Keldysh formalism for Green's functions is given in chapter 2, ending in the derivation of the Usadel equation. In chapter 3, we introduce the concept of *long-range triplets*, the components of the Green's function with the ability to traverse ferromagnets over longer distances. Long-range triplets are fundamental for superconductive transport in ferromagnets, in SF proximity systems. These triplets can be generated through various means, for example through spin-orbit coupling or geometric curvature. In this thesis, we make our way through these methods of generating long-range triplets, starting out with spin-orbit coupling in chapter 3, 1D curvature in chapter 4 and 2D curvature in chapter 6. For each new way of generating long-range triplets, we introduce the relevant formalisms and tools needed for the discussion, such as curvilinear coordinates for 1D curvature and differential geometry for 2D surfaces. We discuss the strengths and weaknesses of each method, demonstrate analytically how they generate long-range triplets, and present numerical results to support our discussions.

1.1 Ferromagnets

Ferromagnets are materials in which localized electrons spontaneously align their spins in a specific direction. This spontaneous symmetry-breaking is referred to as a second-order phase transition, and occurs when lowering its temperature below a specific, material dependent temperature, called the Curie temperature. Ferromagnetism is a quantum mechanical effect, where neighbouring electrons interact with each other through spin-

alignment. This interaction is known as the exchange interaction. Thus, in the ferromagnetic phase, the spin-directions of electrons in these materials will align according to anisotropies specified by material parameters. This collective alignment of electrons will then induce an overall magnetic field in the material in the direction of alignment. This magnetic field is referred to as the exchange field, $\boldsymbol{h}$, and generally represents the order parameter of the phase transition [3].

Due to the exchange interaction between electrons in ferromagnets, propagation of a certain type of quasiparticle, called *magnons* or *spin waves* [4], is allowed to take place. In order to understand spin waves, consider an electron who's spin alignment is disturbed in some way. This electron will then disturb its neighbouring electrons, and thus the disturbance will propagate through the material as a wave. Spin waves occur when the collective alignment of the electrons is disturbed by a whole number of spin flips. In this way, spin waves may carry information through ferromagnetic materials. The field of study that considers the transport of spin waves is known as magnonics, which is a subfield of the broader category *spintronics* [2]. Spintronics as a field considers the transport of spin through whichever means possible. For example, in this thesis we study the transport of spin through superconducting correlations carried by itinerant electrons. Spintronics as a technology dates back to 1857, with the discovery of anisotropic magnetoresistance by Lord Kelvin [5]. Since then, spintronics has given rise to technologies such as tunneling- and giant- magnetoresistance [6], spin valves, quantum spin-hall effect [7], topological insulators [8] and racetrack memories [9]. These technologies are mainly used in storage and memory devices, such as hard drives, with the exception of the quantum spin-Hall effect, which has applications within quantum computation devices. It was discovered that superconductors in contact with ferromagnets have the potential to introduce spin-carrying particles with superconductive properties to the ferromagnet. These new particles have spin excitation lifetimes of several magnitudes higher than those of normal metals, and thus alters and enhances the spin transport properties of the ferromagnet significantly [10]. Because of this, there has been a lot of effort in optimizing the proximity effect and the transport of superconducting correlations in ferromagnets [11], [12], [13]. These systems are referred to as superconductor - ferromagnet (SF) proximity systems, and the main focus in this thesis is on how we can use geometric curvature in SF systems to optimize spin-transport.

1.2 Superconductors

Superconductivity is a phenomenon that traditionally occurs when certain metals and alloys, such as aluminium, mercury or niobium-tin, undergo a second-order phase transition at very low temperatures (the critical temperature is $T_C \approx 4.2K$ for mercury) [14]. In the superconducting phase the electrical resistivity of the metal vanishes such that no energy is lost to heat dissipation during transport of electrons. In addition, the metal will fully expel all external magnetic fields through the Meissner effect. This happens because the superconductor will set up an internal magnetic field that fully cancels the external field, thus acting as a perfect diamagnet. We distinguish between two types of superconductivity based on their response to external magnetic fields. What we call *type I superconductors* ceases to be superconducting after the external magnetic field exceeds a certain critical strength. *Type II superconductors*, on the other hand, have two critical magnetic field strengths. After exceeding the first critical value, type II superconductors enter a phase in which some of the magnetic field is allowed to penetrate. This phase

also features superconducting vortices, whirls of supercurrents typically centered around impurities in the metal. Beyond the second critical value for the magnetic field strength, the superconducting phase is destroyed in the same fashion as for type I superconductors.

These properties make superconductors unique in terms of their potential to facilitate new and improved technologies. Technologies that involve superconductors include superconducting magnets, used in magnetic resonance imaging (MRI) machines, nuclear magnetic resonance (NMR) spectrometers and particle accelerators [15], and Josephson junctions, used in superconducting quantum interference devices (SQUIDs) and as qubits in quantum computing [16]. Another branch of superconducting technologies involves high-temperature (high-T_C) superconductors. These are superconductors with a critical temperature significantly higher than conventional superconductors (for example $T_C \approx 130K$ in the Hg-Ba-Ca-Cu-O system [17]). High-T_C superconductors typically see use in electrical power systems [18].

It took years for scientists to develop a physical theory for superconductivity, since its discovery by Heike Kamerlingh Onnes in 1911. It was first in 1950 when Ginzburg and Landau presented a macroscopic, phenomenological model for superconductivity [19], and in 1957, when Bardeen, Cooper and Schreiffer (BCS) composed their microscopic theory [20], that real progress was made. To this date the BCS theory for superconductivity is the main theory used for microscopic descriptions of conventional superconductors, and the theory that will be used in this thesis. Notably, the BCS theory fails to describe unconventional superconductors, for which there are several theories still developing today. For example, Anderson gave a theoretical description for high-temperature superconductors in 1987 [21], although this area of research is still far from being solved. In the BCS theory, superconductivity arises when electrons in a metal are attracted to each other through some attractive potential. Usually in metals, itinerant electrons are repelled by each other through the Coulomb potential, which is what makes superconductivity such a rare and special phenomenon. However, in conventional superconductors these electrons can be attracted to each other through lattice vibrations, also known as phonons. In this electron-phonon interaction, an electron will pull the heavy positive ions in the metal in its direction as it traverses the metal, leaving a trail with positive charge density. Another electron will then be attracted to this trail. Thus, the two electrons will form a bound state, known as a Cooper pair. In this model, it turns out that the most effective way for Cooper pairs to form is with oppositely pointing momenta, $\boldsymbol{k}$ and $-\boldsymbol{k}$, and in the singlet spin-state, $|S\rangle = \frac{1}{\sqrt{2}}(|\uparrow\downarrow\rangle - |\downarrow\uparrow\rangle)$. This implies that a Cooper pair has net zero momentum. It should be noted that the picture of Cooper pairs forming in superconductors is really a simplification of the actual physical processes behind superconductivity. In reality, Cooper pairs continuously break and re-form. Furthermore, excitations in the condensate causes so-called Bogoliubov quasiparticles to form [22]. These quasiparticles are energy-dependent superpositions of holes and electrons. Nevertheless, the Cooper pair picture makes it more convenient for us to describe superconducting phenomena, and is widely used as a symbol of the more complicated processes in superconductors.

Cooper pairs have bosonic properties. While a single electron has to obey the Pauli exclusion principle, Cooper pairs can all occupy the same state. This means that they obey Bose-Einstein statistics, indicating the possibility for a Bose-Einstein condensation to take place. A Bose-Einstein condensation occurs when all the bosons in a system occupy the ground state, but as mentioned, in superconductors there are still excitations from the ground state. Although a crossover between superconductivity and Bose-Einstein condensation has been verified experimentally [23], these two phenomena typically do not occur

together. Despite this, the superconducting condensate still gains interesting properties, namely that all the Cooper pairs gain the same phase over macroscopic distances. The distance of this phase coherence is called the coherence length, ξ. Furthermore, electrical resistance vanishes in superconductors because Cooper pairs are *protected* from scattering by the *superconducting gap*, $\Delta(\boldsymbol{r},t) = \lambda\langle\hat{\psi}_\uparrow(\boldsymbol{r},t)\hat{\psi}_\downarrow(\boldsymbol{r},t)\rangle$. The superconducting gap is related to the binding energy λ of the attractive potential, relative to the Fermi surface. The idea that the gap protects the Cooper pairs from scattering stems from the fact that the Cooper pairs reside within the Fermi sea. Thus, in order to scatter a bound electron, the superconducting gap must be overcome. But since there are no available states to scatter into, this is not possible, and hence scattering of Cooper pairs does not occur in superconductors. Since the superconducting gap vanishes in the normal metal phase, Δ is used as an order parameter for the phase transition from normal metal to superconductor. The superconducting gap parameter Δ is a complex quantity and is therefore often written in terms of its magnitude and phase, as $\Delta = |\Delta|e^{i\phi}$. The superconducting phase can generally be removed by a $U(1)$ gauge transformation. Therefore, one can assume that Δ is real in systems involving a single superconductor with a constant phase, without the loss of relevant physical information. In systems with multiple superconductors, such as Josephson junctions [16], the *phase difference*, φ, between the superconductors is a physically relevant quantity. In such systems, the phase difference is responsible for driving currents across the junction. An example of this is the 0-π transition in superconductor - normal metal - superconductor (SNS) Josephson junctions. This is a transition in which the current through the junction has a $\sin(\varphi)$ dependence, such that the current will change direction upon tuning the phase difference from 0 to π [24].

1.3 Proximity systems

When a superconductor is placed in contact with another metal, some of the Cooper pairs from the superconductor will leak into the other metal, and itinerant electrons will leak from the other metal to the superconductor. This effect, called the proximity effect, was first studied by Meissner and Holm in 1932, when they noticed the disappearance of resistivity in SNS systems [25]. This implies that we can transfer Cooper pairs into non-superconducting metals. The transport of Cooper pairs across the SN interface occurs via a mechanic called Andreev reflection [26]. In order to understand Andreev reflection, consider an electron attempting to leak from the normal metal to the superconductor, with energy less than $|\Delta|$. Since there are no available states at this energy in the superconductor, the electron has to pair up with an electron of opposite spin in order to leak through the interface. The other electron will thus reflect a hole back into the normal metal. Furthermore, this pair of electrons has to acquire the same phase, $e^{i\phi}$, as the condensate in the superconductor. The reflected hole therefore gains the conjugate phase $e^{-i\phi}$. This mechanic works reversely, through the transmittance of Cooper pairs into the normal metal. The result of these processes is the transmittance of phase-coherent electrons and holes into the normal metal [27], giving us particles with superconductive properties in the normal metal. Hence, transferring Cooper pairs to the normal metal will deplete the superconductor, affecting the pairing potential, which affects the critical temperature and the superconducting gap [11]. If the superconductor is large enough, this depletion is negligible. In this thesis, we will therefore assume the superconducting contacts to act as reservoirs, describing the superconductors by their bulk state.

In this thesis, we mainly consider SF and SFS systems [28]. These are systems in which

superconductors are placed in contact with ferromagnets, as described above. These types of systems have gained attention for their remarkable ability to transport and measure spin. This is surprising considering that superconductivity and ferromagnetism are inherently competing effects. For example, we recall that Cooper pairs form in the singlet spin-state $|S\rangle = \frac{1}{\sqrt{2}}(|\uparrow\downarrow\rangle - |\downarrow\uparrow\rangle$. The exchange field will transform a portion of these pairs into the triplet state $|T_1\rangle = \frac{1}{\sqrt{2}}(|\uparrow\downarrow\rangle + |\downarrow\uparrow\rangle)$, which also has zero net spin [29]. Since the singlet state and the zero-spin triplet consist of two electrons with oppositely aligned spin, the exchange field in the ferromagnet will break this pair due to a combination of the Zeeman effect and the Lorentzian force. The penetration depth of these states into the ferromagnet is typically of the order $\xi_F = \sqrt{D_F/|\boldsymbol{h}|}$, where ξ_F denotes the superconducting coherence length in the ferromagnet, D_F the diffusion constant and $\boldsymbol{h}$ the exchange field. This distance is generally not far into the ferromagnet, compared to the mesoscopic sizes of our systems. In order for the superconducting correlations to penetrate further we therefore need a way to convert the singlet states into triplet states with a finite net spin projection. Triplet states with a finite net spin projection consist of two electrons with the same spin alignment, and are thus not broken by the Zeeman effect or the Lorentzian force. Hence, these triplets decay over a distance of order $\xi_F = \sqrt{D_F/T}$, where T is the temperature of the material. Since the temperature in these systems is considered to be very low, the coherence length for these triplets is much longer than $\sqrt{D_F/|\boldsymbol{h}|}$. These types of triplet states are therefore referred to as *long-range triplets* (LRTs), for their ability to penetrate deeper into the ferromagnet [30]. Triplets with a net zero spin projection are referred to as *short-range triplets* (SRTs). Interestingly, because we are considering metals with a high impurity density the s-wave components (the components with spatial symmetry) of the triplets are dominating. Because of this the triplets are even in both spin and space, and hence have to be odd in time in order for the electrons to obey the Pauli principle. The result of this is triplets that are odd-in-time, a phenomenon that is known as *odd-frequency pairing* [31]. The first way to generate LRTs was to make the ferromagnetic region feature an exchange field with a spatially varying axis [32]. Later, it was found that spin-orbit (SO) coupling could generate LRTs [33]. Recently, curvature has been studied as a third way to achieve this effect [34].

1.4 Curvature

By curvature in the material, we mean a material that is physically curved in space in some way. Such curved materials can be manufactured with or without strain. The recent progress in the fabrication of nanomaterials with these qualities has led to research studying curvature more in-depth. There have been several studies on curved superconductors [35] [36], curved ferromagnets [37] and antiferromagnets [38] [39] [40]. In superconductors, curvature can be used to generate and control spin triplet Cooper pairs [41], which can, for example, be used to control 0-π transitions in Josephson junctions [42]. In magnetic systems, curvature is mainly used to manipulate the exchange field. The main way the exchange field is manipulated is through an effective, curvature-induced Dzyaloshinskii-Moriya interaction (DMI) and a magnetic anisotropy in the magnetic exchange energy. These interactions can be used for domain wall dynamics [43] [44], asymmetric spin-wave dispersions [45] and to allow skyrmions to exist in the ground state [46] [47], to name some applications. Curved magnetic systems are experimentally realizable using, for example, two-photon lithography [48], or electron beam lithography, where materials have

been manufactured at a size of 10 nm in thickness, $75 - 135$ nm in width and a length of 2 μm, with a curvature of $0.005 - 0.07$ nm^{-1} [49].

Recently, curvature has been studied in proximity systems such as SF, SFS and superconductor - antiferromagnet systems [50]. Here, curvature has been studied in ferromagnetic and antiferromagnetic helical wires in contact with a superconductor, where it was shown that generation of LRTs is possible in such systems [51] [52]. In the antiferromagnetic helical wire, curvature facilitates the measurement of the compensation of the interface. Furthermore, curvature has been shown to induce a chirality-dependent spin polarization of the superconducting correlations. In non-constant curvature in SFS nanowires we can, for example, obtain mixed chirality junctions, with possible applications in spin-triplet SQUIDs [53]. In this thesis we are generally interested in curvature as a means to create LRTs and control spin-transport in SF/SFS systems. Geometrically curving a ferromagnet in space, we can induce both a curvature dependent SO field and a spatially varying exchange field in the metal. Hence, we can achieve many of the same effects as inherent SO coupling or an inhomogeneous exchange field, through curvature. The advantages of curvature over the two other methods come from the increased flexibility we gain from being able to tune the curvature as we like. For example, through varying the curvature in a Josephson junction we can reverse the current, effectively inducing a 0-π transition, without changing the phase difference [54].

1.5 Diffusion in 2 dimensions

In this thesis, we will consider diffusive systems within a quasiclassical framework. For such systems, the Usadel equation describes the diffusion of superconductive correlations well. The Usadel equation is a diffusion-like equation in the form of a system of nonlinear differential equations [55]. For 1-dimensional SF- and SFS-systems, this equation has been studied extensively in various experimental and theoretical setups. However, in 2D far less work has been done on this topic. By 2D materials we refer to a thin film material, in which the thickness of the material in one direction is considered to be much smaller than in the other two directions, and not a monolayer material, such as graphene. 1D systems have been favored over higher dimensional systems since the Usadel equation takes the form of an ordinary differential equation (ODE) in 1D, while it turns into a partial differential equation (PDE) in higher dimensions. This makes the Usadel equation generally more difficult to solve in 2D than in 1D. Previous works on the 2D Usadel equation have mainly been numerical, due to its complexity [56], with the exception of some analytical results in quasi-1D limits [57]. In this thesis we will solve the general Usadel equation numerically, using the finite-element method. The reason we choose the finite element method over other PDE algorithms is because this method allows us to solve for a wider array of different geometries, than compared to the finite difference method, for example.

The novelty of this thesis lies in the description and calculation of the 2D Usadel equation under curvature. Previous works have studied the 2D Usadel equation in flat geometries, and the 1D Usadel equation under curvature, but never both in the same system. The main point of this thesis is therefore to develop a framework to facilitate for further studies on spin-transport in 2D curved SF systems, and consider basic examples of these systems numerically. Our expectation is that there are novel mechanics to be found and new possibilities to study in these systems. 2D curved systems could for example be used to stabilize racetrack memories. In racetrack memories skyrmions are

being created in thin films by an external magnetic field, then transported by an applied voltage. These skyrmions have an unfortunate drift velocity, meaning that they drift away from their tracks over longer distances [58]. Curving these racetracks could stabilize these skyrmions, since traversing steeper curvature costs energy. It has, for example, been shown by Kravchuk et al. (2018) [46] that there can be stable skyrmions in the ground state of curved systems. 2D curved SF systems could also be used to study dynamics in general relativity, through the anti-de-Sitter/conformal field theory correspondence [59]. In general, 2D curvature lets us study phenomena exclusive to higher dimensions such as magnetic flux, skyrmions, vortices and geodesics on surfaces, under curvature [60].

2 Green's functions

The dynamics of the systems we aim to describe in this thesis are physically quite complicated, and not necessarily intuitive to explain or dissect. Therefore, there have been created several formalisms that each allow us to more effectively approach these systems. Each formalism has its strengths, and carries its own set of assumptions about the system. For diffusive metals in the quasiclassical theory the Usadel equation, which builds on the Keldysh-formalism for Green's functions, is the main formalism used. The derivation of the Usadel equation, from basic principles, involves a series of approximations that are based on a set of assumptions and restrictions we enforce on our systems. In this section, the goal is therefore to carefully outline and motivate the assumptions and approximations that are made in the derivation of this equation. In order to do this we first have to introduce the Keldysh formalism for Green's functions [61].

2.1 Keldysh formalism in Nambu-Spin space

In quantum mechanics and condensed matter physics a mathematical concept known as the Green's function is of special importance. In general mathematics a Green's function, G, can be described as the impulse response of a given differential operator, $\hat{L}$, such that the Green's function is related to its corresponding differential operator through $\hat{L}G(\boldsymbol{r},\boldsymbol{r}') = \delta(\boldsymbol{r},\boldsymbol{r}')$, where $\delta(\boldsymbol{r},\boldsymbol{r}')$ is the Dirac's delta function. In other words, the Green's function can be viewed as the inverse function to its differential operator. One can already see how Green's functions could be relevant in solving physical systems and equations, but it turns out that their role in quantum mechanics, especially within the second quantization formalism, is more central than at first glance.

In the second quantization formalism, Green's functions take the form of averages of time-ordered sets of field operators [62]. We can define a general Green's function as

$$G_{\sigma\sigma'}(\boldsymbol{r},t,\boldsymbol{r}',t') = -i\langle T\{\psi_\sigma(\boldsymbol{r},t)\psi^\dagger_{\sigma'}(\boldsymbol{r}',t')\}\rangle, \tag{2.1}$$

where the time-ordering operator T ensures that the operators are applied consecutively in time, as follows

$$T\{\psi_\sigma(\boldsymbol{r},t)\psi^\dagger_{\sigma'}(\boldsymbol{r}',t')\} = \begin{cases} \psi_\sigma(\boldsymbol{r},t)\psi^\dagger_{\sigma'}(\boldsymbol{r}',t') & \text{if } t < t', \\ -\psi^\dagger_{\sigma'}(\boldsymbol{r}',t')\psi_\sigma(\boldsymbol{r},t) & \text{if } t > t'. \end{cases} \tag{2.2}$$

On this form, the Green's functions in quantum mechanics are seen to be related to the probability amplitude of a particle propagating from $(\boldsymbol{r},t)$ with spin σ to $(\boldsymbol{r}',t')$ with spin σ'. This means that we can describe most of the physical quantities that relate to the motion and interaction of particles in materials, from these Green's functions alone. In this thesis, we will use Green's functions to calculate the density of states (DoS), electrical charge current, and more. For these reasons, the main objective of this thesis centers around finding the Green's functions to the systems of our interest.

The Green's function of a differential operator is not necessarily unique, and any linear combination of solutions to the homogeneous equation is also a solution. It is therefore useful to define multiple Green's functions on the same form as (2.1) that correspond to different physical phenomena. There are multiple ways to do this, and in this thesis we will follow the Keldysh real-time formalism. We define the following Green's functions

$$G^R_{\sigma\sigma'}(\boldsymbol{r},t,\boldsymbol{r}',t') = -i\langle\{\psi_\sigma(\boldsymbol{r},t),\psi^\dagger_{\sigma'}(\boldsymbol{r}',t')\}\rangle H(t-t'), \tag{2.3}$$

$$G^A_{\sigma\sigma'}(\boldsymbol{r},t,\boldsymbol{r}',t') = +i\langle\{\psi_\sigma(\boldsymbol{r},t),\psi^\dagger_{\sigma'}(\boldsymbol{r}',t')\}\rangle H(t'-t), \tag{2.4}$$

$$G^K_{\sigma\sigma'}(\boldsymbol{r},t,\boldsymbol{r}',t') = -i\langle[\psi_\sigma(\boldsymbol{r},t),\psi^\dagger_{\sigma'}(\boldsymbol{r}',t')]\rangle, \tag{2.5}$$

where G^R and G^A are referred to as the retarded and advanced Green's function, respectively, and $H(x-x')$ is the Heaviside function. As can be interpreted from these expressions, the retarded Green's function describes propagation of particles forward in time, and thus depends on past events, while the advanced Green's function represents the time-reversed version of G^R, and is thus linked to anticipation of future events. G^K is referred to as the Keldysh Green's function, and describes the non-equilibrium properties of the system.

Since the BCS theory expresses superconductivity as averages over pairs of annihilation or creation operators, we need to extend the definition of the field operator ψ to account for the qualitatively different Green's functions that we want to describe. We therefore express our operators in Nambu-space, where the field operator is defined as

$$\Psi_1 = \begin{pmatrix}\psi_1\\ \psi_1^\dagger\end{pmatrix} \quad \text{and} \quad \Psi_1^\dagger = \begin{pmatrix}\psi_1^\dagger & \psi_1\end{pmatrix}. \tag{2.6}$$

In addition to this, we would like to be able to describe the mechanics of the field operators with respect to their spin. Therefore, we express Ψ in the conjoined Nambu$\otimes$Spin-space, as

$$\Psi_1 = \begin{pmatrix}\psi_{1\uparrow}\\ \psi_{1\downarrow}\\ \psi^\dagger_{1\uparrow}\\ \psi^\dagger_{1\downarrow}\end{pmatrix} \quad \text{and} \quad \Psi_1^\dagger = \begin{pmatrix}\psi^\dagger_{1\uparrow} & \psi^\dagger_{1\downarrow} & \psi_{1\uparrow} & \psi_{1\downarrow}\end{pmatrix}, \tag{2.7}$$

where we have condensed the arguments of the field operators into subscripts, i.e. Ψ_1 should be read to mean $\Psi(\boldsymbol{r}_1,t_1)$. In this extended formalism, the retarded, advanced and Keldysh Green's functions now become 4×4 matrices, defined as

$$\hat{G}^R = \begin{pmatrix}\underline{G}^R & \underline{F}^R\\ \underline{F}^{R*} & \underline{G}^{R*}\end{pmatrix}, \tag{2.8}$$

$$\hat{G}^A = \begin{pmatrix}\underline{G}^A & \underline{F}^A\\ \underline{F}^{A*} & \underline{G}^{A*}\end{pmatrix}, \tag{2.9}$$

$$\hat{G}^K = \begin{pmatrix}\underline{G}^K & \underline{F}^K\\ -\underline{F}^{K*} & -\underline{G}^{K*}\end{pmatrix}, \tag{2.10}$$

where the 2×2 matrices in (2.8)-(2.10) describe the Green's functions in spin-space, and they all take the form

$$\underline{G} = \begin{pmatrix}G_{\uparrow\uparrow} & G_{\uparrow\downarrow}\\ G_{\downarrow\uparrow} & G_{\downarrow\downarrow}\end{pmatrix}. \tag{2.11}$$

Here, we have defined a new type of Green's function, $F_{\sigma\sigma'}(\boldsymbol{r},t,\boldsymbol{r}',t')$ as

$$F^R_{\sigma\sigma'}(\boldsymbol{r},t,\boldsymbol{r}',t') = -i\langle\{\psi_\sigma(\boldsymbol{r},t),\psi_{\sigma'}(\boldsymbol{r}',t')\}\rangle H(t-t'), \tag{2.12}$$

$$F^A_{\sigma\sigma'}(\boldsymbol{r},t,\boldsymbol{r}',t') = +i\langle\{\psi_\sigma(\boldsymbol{r},t),\psi_{\sigma'}(\boldsymbol{r}',t')\}\rangle H(t'-t), \tag{2.13}$$

$$F^K_{\sigma\sigma'}(\boldsymbol{r},t,\boldsymbol{r}',t') = -i\langle[\psi_\sigma(\boldsymbol{r},t),\psi_{\sigma'}(\boldsymbol{r}',t')]\rangle. \tag{2.14}$$

F is known as the anomalous Green's function. The anomalous Green's function involves averages over pairs of annihilation or creation operators, and is thus related to the superconducting gap. Hence, F describes the presence of Cooper pairs.

$\hat{G}^R$, $\hat{G}^A$ and $\hat{G}^K$ are ordered in a single 8×8 matrix $\check{G}$ in Keldysh-space, which we will refer to as the Green's function matrix or just the Green's function. It is given by

$$\check{G} = \begin{pmatrix} \hat{G}^R & \hat{G}^K \\ 0 & \hat{G}^A \end{pmatrix}. \tag{2.15}$$

The three Green's functions $\hat{G}^R$, $\hat{G}^A$ and $\hat{G}^K$ are not all independent, and can be shown to be related by

$$\hat{G}^A = -\hat{\tau}_z(\hat{G}^R)^\dagger\hat{\tau}_z, \tag{2.16}$$

$$\hat{G}^K = (\hat{G}^R - \hat{G}^A)\tanh\left(\frac{E}{2T}\right), \tag{2.17}$$

where equilibrium is required for (2.17) to hold [63]. Thus it is in general sufficient to only calculate one of the three Green's function matrices, when considering systems in equilibrium. In this thesis we will therefore focus on calculating $\hat{G}^R$.

2.2 The quasiclassical approximation

When describing Green's functions, it can be more useful to use center of mass coordinates, denoted by

$$\boldsymbol{R} = \frac{1}{2}(\boldsymbol{r}_1+\boldsymbol{r}_2), \quad \boldsymbol{r} = \boldsymbol{r}_1-\boldsymbol{r}_2, \quad T = \frac{1}{2}(t_1+t_2), \quad t = t_1-t_2. \tag{2.18}$$

The reason for this is that $\check{G}$ acts as a modulated wave packet, with $\boldsymbol{R}$ describing the coordinates of the envelope and $\boldsymbol{r}$ describing the coordinates of the internal oscillations. The scale of the internal oscillations is of the same order as the inverse Fermi wave vector, $\boldsymbol{k}_F^{-1}$. This is very small compared to the envelope, since the superconducting coherence length is generally much larger than $\boldsymbol{k}_F^{-1}$. Because of this, we can *remove* degrees of freedom from our equations, since we are mainly interested in the transport of particles over distances at the scale of the superconducting coherence length. We do this by taking an average over the relative coordinate $\boldsymbol{r}$. In practice, this is done by first conducting the coordinate transformations outlined in (2.18), then Fourier transforming the relative coordinates. The Green's function matrix then takes the form $\check{G}(\boldsymbol{R},T,\boldsymbol{p},E)$, where $\boldsymbol{p}$ and E thus refer to the momentum and energy of the internal oscillations, respectively [63].

The last step in simplifying the Green's function is to assume that the electron scattering processes in the metal are close to the Fermi surface. This assumption is justified through the fact that we are mainly studying materials at very low temperatures. At

low temperatures, most of the Fermi sphere is filled, and so scattering processes have to involve electrons close to the Fermi surface. Because of this, we can average over the relative coordinates by setting the value of the energy to the Fermi energy. Doing this gives us an expression for the so-called quasiclassical Green's function $\check{g}$, given by

$$\check{g}(\boldsymbol{R}, T, \boldsymbol{p}_F, E) = \frac{i}{\pi} \int d\epsilon_p \check{G}(\boldsymbol{R}, T, \boldsymbol{p}, E), \tag{2.19}$$

where $\epsilon_p = \frac{\boldsymbol{p}^2}{2m} - \mu$ is the kinetic energy relative to the Fermi level. The integral in this definition behaves poorly at higher energies. A cut-off frequency is therefore introduced in the integral to correct this issue. This is equivalent to confining $\check{G}$ to the Fermi surface, as can be seen from the relation

$$\check{G}(\boldsymbol{R}, T, \boldsymbol{p}, E) = -i\pi\delta(\epsilon_p)\check{g}(\boldsymbol{R}, T, \boldsymbol{p}_F, E). \tag{2.20}$$

This sequence of transformations and approximations of the Green's function matrix is known as the quasiclassical approximation. The term quasiclassical comes presumably from the fact that we have removed the wave mechanics from half of the coordinates of the Green's function. Thus we are treating one part of the system classically and the other part quantum mechanically.

We perform the quasiclassical approximation on all the elements in $\check{G}$. Doing this, we should be careful in taking the complex conjugate of $\check{G}(\boldsymbol{R}, T, \boldsymbol{r}, t)$. In defining $\check{g}(\boldsymbol{R}, T, \boldsymbol{p}_F, E)$ in terms of $\check{G}(\boldsymbol{R}, T, \boldsymbol{r}, t)$ we have performed a Fourier transform and added a complex prefactor. Taking the complex conjugate of $\check{G}(\boldsymbol{R}, T, \boldsymbol{r}, t)$, we should therefore reverse the sign of E in $\check{g}$, and reverse the sign of $\check{g}$ itself. This gives us the following definition of $\check{g}$

$$\check{g} = \begin{pmatrix} \hat{g}^R & \hat{g}^K \\ 0 & \hat{g}^A \end{pmatrix}, \tag{2.21}$$

where the 4×4 matrices take the form

$$\hat{g}^R = \begin{pmatrix} \underline{g}^R & \underline{f}^R \\ -\underline{\tilde{f}}^R & -\underline{\tilde{g}}^R \end{pmatrix}, \tag{2.22}$$

$$\hat{g}^A = \begin{pmatrix} \underline{g}^A & \underline{f}^A \\ -\underline{\tilde{f}}^A & -\underline{\tilde{g}}^A \end{pmatrix}, \tag{2.23}$$

$$\hat{g}^K = \begin{pmatrix} \underline{g}^K & \underline{f}^K \\ \underline{\tilde{f}}^K & \underline{\tilde{g}}^K \end{pmatrix}. \tag{2.24}$$

Here, we have used the *tilde-conjugate*, defined by

$$\tilde{g}(E) = g^*(-E). \tag{2.25}$$

Since $\check{g}$ should satisfy the normalization condition [61]

$$\check{g}\check{g} = \check{I} \tag{2.26}$$

in equilibrium, the components of $\check{g}$ should obey three normalization conditions

$$\hat{g}^R\hat{g}^R = \hat{I}, \quad \hat{g}^A\hat{g}^A = \hat{I} \quad \text{and} \quad \hat{g}^K\hat{g}^A + \hat{g}^R\hat{g}^K = 0. \tag{2.27}$$

2.3 The dirty limit

The materials to be considered in this thesis will all be assumed to have a high impurity density. Such materials are referred to as dirty metals. Dirty metals are characterized by having a scattering rate τ_{imp}^{-1} which is much greater than other energy scales in the system [64]. As a result from the frequent scattering, the direction of the momentum of the Green's function is randomized at any point in space. This means that $\check{g}$ becomes almost isotropic in momentum. We therefore expand the Green's function to first order in spherical harmonics, allowing us to split $\check{g}$ in one isotropic part and one anisotropic part,

$$\check{g} = \check{g}_s + \hat{\boldsymbol{p}}_F \cdot \check{g}_p. \tag{2.28}$$

Here, the s-wave component, $\check{g}_s$, denotes the isotropic part of $\check{g}$, while the p-wave component, $\check{g}_p$, denotes the anisotropic part. Due to the implications of the dirty limit, the isotropic part dominates, and we have $\check{g}_p \ll \check{g}_s$. This limit therefore allows us to simplify the equations describing the dynamics of our systems significantly.

The reason for considering systems in the dirty limit in this thesis, as opposed to consider so-called ballistic transport which entails clean metals, is twofold. The first reason is that taking the dirty limit allows for helpful approximations. For example, one does not need to calculate the anisotropic parts of the Green's function matrix in this limit. The other reason is that dirty metals are more practical to manufacture and conduct experiments on than clean metals.

2.3.1 The Usadel equation

With the quasiclassical formalism for Green's functions in Keldysh-space, we can now derive an effective equation of motion for $\check{g}$, in the dirty limit. The details of this derivation are very well documented, especially by previous theses written on this very subject [65] [66] [63] [67]. Furthermore, the details of this derivation are not necessary in order to follow the rest of the discussion in this thesis. Because of this, we only mention briefly the main steps and assumptions made in this derivation, for completeness of the discussion.

The derivation of the Usadel equation starts by operating with the free electron operator on the Dyson equation from both the left and right, giving us an equation of motion for the Green's function on commutation form. This equation involves both the Green's function matrix and the self-energy. The equation is then treated in the quasiclassical approximation, where the equation of motion is written in the mixed representation outlined in (2.18), then subjugated to a series of Fourier transforms. Along these steps, the assumptions made in section 2.2 are liberally applied in order to simplify the equation. This results in the so-called Eilenberger equation [68], given by

$$[E\hat{\tau}_z - \check{\Sigma}, \check{g}] + i\boldsymbol{v}_F \cdot \nabla_R \check{g} = 0. \tag{2.29}$$

Here, $\check{\Sigma}$ denotes the total self-energy of the Green's function matrix. The choice of what self-energies to include in $\check{\Sigma}$ depends on which material we are considering and what assumptions we have made. In this thesis we are dealing with superconductor-ferromagnet proximity systems in the dirty limit. As such, it is natural to include both the superconducting self-energy, given by

$$\check{\Sigma}_{SC} = \hat{\Delta} = \text{antidiag}(\underline{\Delta}, \underline{\Delta}^*), \quad \underline{\Delta} = \text{antidiag}(\Delta, -\Delta), \quad \Delta = \lambda\langle\psi_\uparrow\psi_\downarrow\rangle, \tag{2.30}$$

and the ferromagnetic self-energy for weak ferromagnets, given by

$$\check{\Sigma}_{FM} = \boldsymbol{h}\cdot\hat{\boldsymbol{\sigma}}, \quad \hat{\boldsymbol{\sigma}} = \text{diag}(\underline{\boldsymbol{\sigma}}, \underline{\boldsymbol{\sigma}}^*). \tag{2.31}$$

Since we are in the dirty limit we also need to include the self-energy for impurity scattering, given by

$$\check{\Sigma}_{imp} = -\frac{i}{2\tau_{imp}}\check{g} \tag{2.32}$$

in the Born-approximation for weak scattering [65]. As mentioned above, the scattering rate τ_{imp}^{-1} is considered to be much greater than the other energy scales in dirty metals. This fact is used, along with the approximation in (2.28), to simplify (2.29). The result is the Usadel equation, given by

$$iD_F\nabla_R\cdot(\check{g}_s\nabla_R\check{g}_s) = [E\hat{\tau}_z + \hat{\Delta} + \boldsymbol{h}\cdot\hat{\boldsymbol{\sigma}}, \check{g}_s]. \tag{2.33}$$

Here $D_F = \frac{v_f^2\tau_{imp}}{3}$ denotes the diffusion constant, $\boldsymbol{h}$ denotes the magnetic exchange field and $\hat{\boldsymbol{\sigma}}$ denotes the Pauli matrix vector. This equation only includes the s-wave component of the Green's function matrix. Because of this, the Usadel equation is not capable of describing transport of anisotropic Green's function, such as p-wave Green's functions. In order to describe such transport, other methods such as the Eilenberger equation or the Bogoliubov-de Gennes (BdG) method [69] must be used.

We mention here that the Usadel equation takes the form of a diffusion-like nonlinear differential equation. This equation is thus interpreted to describe the diffusion of electrons, holes and superconducting correlations in the material. We also note that (2.33) in reality describes 48 separate equations, due to the form of the 8×8 Green's function matrix. However, since we are only interested in systems in equilibrium, considering only the equation for $\hat{g}_s^R$ is sufficient, reducing the amount of equations to 16. The Usadel equation for $\hat{g}_s^R$ looks the same as for $\check{g}_s$,

$$iD_F\nabla\cdot(\hat{g}^R\nabla\hat{g}^R) = [E\hat{\tau}_z + \hat{\Delta} + \boldsymbol{h}\cdot\hat{\boldsymbol{\sigma}}, \hat{g}^R]. \tag{2.34}$$

Here, we have dropped the s-subscript, as all the Green's functions to be considered in this thesis will be s-wave. Furthermore, due to normalization conditions and symmetries, we can reduce this number down to 8 by introducing an appropriate parametrization, as we show in section 6.2.1. Tackling a system of 8 nonlinear differential equations is still a daunting task, and generally only solvable analytically under certain approximations. Therefore, numerical methods are generally preferred when dealing with the Usadel equation.

Finally, we note that the dimensionality of the system affects the Usadel equation in an important way. In 1D, (2.33) takes the form of an ordinary differential equation. In higher dimensions, however, it takes the form of a partial differential equation, which significantly complicates the equation. Therefore, the majority of the work on this equation so far has been done in 1 dimensional systems. This is one of the reasons why the 2-dimensional approach in this thesis is considered interesting, as it may illuminate novel properties and mechanics in SF proximity systems.

2.3.2 Boundary conditions

We need appropriate boundary conditions to accompany the Usadel equation. In this thesis we will use the Kupriyanov-Lukichev boundary conditions [70], given by

$$\hat{\boldsymbol{n}} \cdot \hat{g}_j^R \nabla \hat{g}_j^R = \frac{1}{2L_j\zeta_j}[\hat{g}_1^R, \hat{g}_2^R], \tag{2.35}$$

where L_j is the length of material j, $\hat{\boldsymbol{n}}$ is the normal vector to the interface, and $\zeta_j = \frac{R_B}{R_j}$ describes the ratio between the boundary resistance, R_B, and the bulk resistance in material j, R_j. The vacuum boundary condition is found by letting the boundary resistance go to infinity, which corresponds to setting the right-hand side of (2.35) to 0. The Kurpiyanov-Lukichev boundary conditions are a simplification to the more general Nazarov boundary conditions [71]. The simplification is made by taking the tunneling limit, $T_n \ll 1$, where the transmission probabilities at the interface, T_n, are assumed to be very small. The reasons for restricting us to this limit, and not using the more general Nazarov boundary conditions, are similar to the reasons for considering dirty metals. The Kupriyanov-Lukichev boundary conditions are simpler to work with, and represent physical systems that are easier to manufacture in experimental setups.

3 Generation of long range triplets

In section 1.3 we introduced the proximity effect in superconductor-ferromagnet (SF) systems. In this chapter, we will look further into how we can optimize the transportation of superconducting correlations into the ferromagnet. To begin this discussion, recall that Cooper pairs generally form in the singlet state, $|S\rangle = \frac{1}{\sqrt{2}}(|\uparrow\downarrow\rangle - |\downarrow\uparrow\rangle)$, in spin-space. When the Cooper pairs leak into the ferromagnet, the exchange field will cause several things to happen to these correlations. First off, the Zeeman interaction between the exchange field and the oppositely aligned spin states will shift the momenta of the two electrons in the Cooper pair, giving the Cooper pair a finite momentum $\boldsymbol{q}$. This spin splitting will thus alter the singlet state according to [29]

$$e^{i\boldsymbol{q}\cdot\boldsymbol{r}}|\uparrow\downarrow\rangle - e^{-i\boldsymbol{q}\cdot\boldsymbol{r}}|\downarrow\uparrow\rangle = \cos(\boldsymbol{q}\cdot\boldsymbol{r})|S\rangle + i\sin(\boldsymbol{q}\cdot\boldsymbol{r})|T_1\rangle\,, \tag{3.1}$$

where we have defined the triplet state with zero spin projection as $|T_1\rangle = \frac{1}{\sqrt{2}}(|\uparrow\downarrow\rangle + |\downarrow\uparrow\rangle)$. We thus end up with a mixture of singlet states and triplet states in the ferromagnet. This mixed state of singlet and triplets is referred to as an FFLO state, after Fulde, Ferrell, Larkin and Ovchinnikov [72] [73], and the process of creating FFLO states is referred to as *spin-mixing*. We note that although this is a triplet state, its total spin projection is still zero due to the two electrons being aligned oppositely in spin-space. The second effect of the exchange field on the Cooper pairs is to pull oppositely aligned electrons apart from each other, effectively destroying the Cooper pairs. This effect occurs due to a combination of the Lorentzian force and the Zeeman interaction. As a result, the singlet state and $|T_1\rangle$ correlations will only penetrate a short distance into the ferromagnet. Because of this, we call the $|T_1\rangle$ state correlations *short-range triplets* (SRTs). Thus, in order for the superconductive correlations to penetrate deep into the ferromagnet, we require these pairs to be aligned in the same spin-direction. Spin-states with this quality are triplet states in the form $|T_2\rangle = |\uparrow\uparrow\rangle$ or $|T_3\rangle = |\downarrow\downarrow\rangle$, and are referred to as *long-range triplets* (LRTs) due to their ability to penetrate further into the ferromagnetic region. The process of generating LRTs from singlets is outlined in figure 3.1.

LRTs are generated from SRTs through a process known as spin-rotation. This process occurs in the ferromagnetic region and can be achieved through three main mechanics:

(i) a spatially varying magnetic field;

(ii) spin-orbit coupling;

(ii) geometric curvature.

By a spatially varying magnetic field, we mean a field that changes its orientation spatially. A spatially varying magnetic structure will rotate the SRTs in spin space as it ventures through the ferromagnet, producing LRTs. This way of producing LRTs was the first method found for SF proximity systems [74] [30]. This method entails either producing ferromagnets with a spatially varying magnetic texture, such as a material with domain walls, applying an external magnetic field that varies in space or using materials with an inherently inhomogeneous magnetic field, such as holmium [75]. Magnetic domain walls can be unpredictable and difficult to control, an external magnetic field will affect the system in its own way and put restrictions on the types of systems one can study, and holmium is a rare material. Because of this, there was a desire to develop alternate

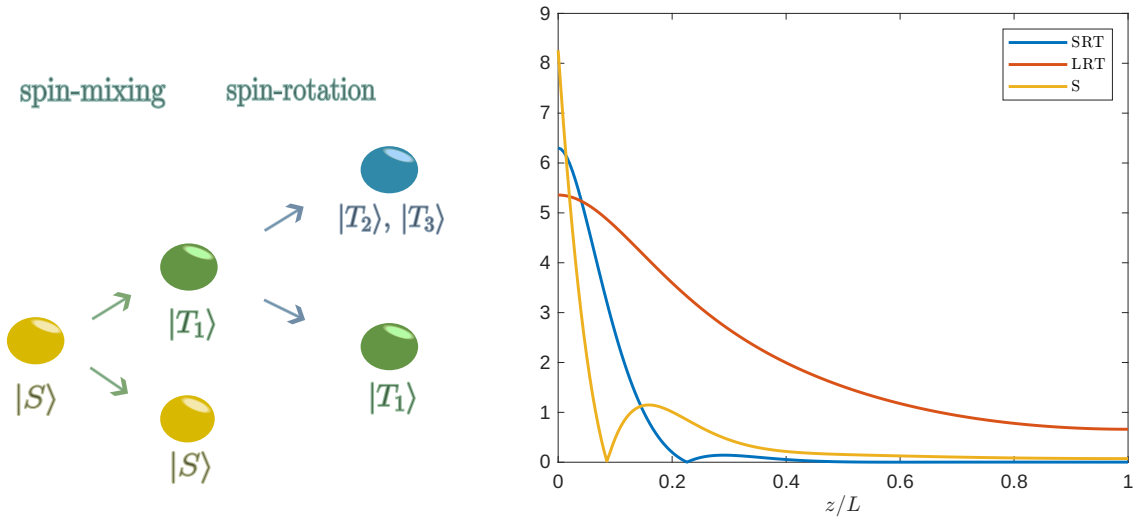

(a) (b)

Figure 3.1: (a) Spin-mixing visualized as the generation of SRTs from singlets, and spin-rotation as the generation of LRTs from SRTs. (b) Plot of the penetration of singlet states, LRTs and SRTs into the ferromagnetic region. This figure has been reconstructed from Linder & Robinson (2015) [10].

methods of generating LRTs. Another such method can be realized through inherent spin-orbit (SO) coupling in the material [33]. SO coupling can be induced in materials through various means, but is typically generated in materials with a broken inversion symmetry. The reason SO coupling works as a method for spin rotation is due to the fact that an electron will experience an effective magnetic field. This way, the electrons interact with a rotating magnetic field without there having to be a rotating exchange field in the material.

Recently, there has been discovered a third way of generating LRTs, namely through geometric curvature. Geometric curvature can induce both a spatially varying exchange field and SO coupling in the material, and can therefore be viewed as a combination of the first two mechanics. Thus, in order to understand how curvature generates LRTs, we must first understand how we can generate LRTs through the two aforementioned mechanics. In the introduction to chapter 4 we discuss how curvature can induce a spatially varying magnetic field. The rest of this chapter will be dedicated to understanding the effects of SO coupling on SF proximity systems.

3.1 Spin-orbit coupling

To begin the discussion on SO coupling,let us first consider an electron moving in an electric field, with zero external magnetic field. Although the external magnetic field is zero, the effective magnetic field is $\boldsymbol{B}_{eff} = \boldsymbol{B}_{ext} - \boldsymbol{v} \times \boldsymbol{E}$ due to the Lorentz transformation of the magnetic field, where $\boldsymbol{E}$ denotes the electric field [76]. Here, the velocity is assumed to be small compared to the speed of light, such that the Lorentz factor can be approximated to 1. Thus, due to relativistic effects, the moving electron experiences an effective magnetic field in the presence of an electric field. This magnetic field will now couple with the spin of the electron through the Zeeman interaction

$$\mathcal{H}_{SO} = -\underline{\boldsymbol{\mu}}_e \cdot \boldsymbol{B}_{eff} = \frac{egE}{4m^2}\underline{\boldsymbol{\sigma}} \cdot (\boldsymbol{p} \times \hat{\boldsymbol{n}}). \tag{3.2}$$

Here, $\underline{\boldsymbol{\mu}}_e = \frac{eg}{2m}\underline{\boldsymbol{S}}$ denotes the magnetic moment, $g \approx 2$ the g-factor, and $\underline{\boldsymbol{S}} = \frac{\boldsymbol{\sigma}}{2}$ the spin-vector of the electron. We have also defined the electric field $\boldsymbol{E} = E\hat{\boldsymbol{n}}$ in terms of its magnitude and direction. We can rewrite the cross product in (3.2) using the vector identity $\boldsymbol{A} \cdot (\boldsymbol{B} \times \boldsymbol{C}) = \boldsymbol{C} \cdot (\boldsymbol{A} \times \boldsymbol{B})$ twice, to get

$$\mathcal{H}_{SO} = \frac{egE}{4m^2}\boldsymbol{p} \cdot (\hat{\boldsymbol{n}} \times \underline{\boldsymbol{\sigma}}) = -\frac{1}{m}\boldsymbol{p} \cdot \underline{\boldsymbol{A}}. \tag{3.3}$$

Here we have defined the SO field $\underline{\boldsymbol{A}} = \alpha(\hat{\boldsymbol{n}} \times \underline{\boldsymbol{\sigma}})$, and the SO coupling constant $\alpha = -\frac{egE}{4m}$. In conjunction with the kinetic term, the Hamiltonian can now be written

$$\mathcal{H} = \frac{\boldsymbol{p}^2}{2m} - \frac{1}{m}\boldsymbol{p} \cdot \underline{\boldsymbol{A}} \approx \frac{1}{2m}(\boldsymbol{p} - \underline{\boldsymbol{A}})^2, \tag{3.4}$$

where we have ignored the $\underline{\boldsymbol{A}}^2$-term under the assumption that the SO field is weak. Equation (3.4) now corresponds to a charged particle moving in an SU(2) gauge field $\underline{\boldsymbol{A}}$. That is, we have effectively induced an SU(2) field in our system, via the SO coupling. Because of this SU(2) field, we require all physical quantities to be invariant under an SU(2) transformation. This is achieved by replacing the usual derivative with the gauge covariant derivative $\tilde{\nabla}$, such that [33]

$$\nabla v \to \tilde{\nabla} v = \nabla v - i[\underline{\boldsymbol{A}}, v] \tag{3.5}$$

becomes the new derivative.

The form of the SO field $\underline{\boldsymbol{A}}$ depends on the nature of origin of the electric field $\boldsymbol{E}$. In the context of SO coupling, such an electric field usually appears due to the breaking of inversion symmetry in the crystal structure of the material. An inversion asymmetry will induce an electric field in the crystal, and can give rise to two types of SO coupling. The first type of SO coupling comes from an inversion asymmetry near the interfaces of the material. If the material is sufficiently thin, this asymmetry may permeate the whole material. Such an asymmetry gives rise to so-called *Rashba spin-splitting* [77]. If we choose the z-axis as the layering direction, the SO field due to Rashba spin-splitting is given by

$$\underline{\boldsymbol{A}}_R = \alpha_R(-\underline{\sigma}_y, \underline{\sigma}_x, 0). \tag{3.6}$$

The second type of SO coupling arises due to *bulk inversion asymmetry*, i.e. inversion asymmetry in the bulk of the material. This gives rise to *Dresselhaus spin splitting*, which gives the SO field the form [78]

$$\underline{\boldsymbol{A}}_D = \alpha_D(\underline{\sigma}_x, -\underline{\sigma}_y, 0). \tag{3.7}$$

Here, α_R and α_D are referred to as the Rashba and Dresselhaus coupling strength, respectively. These coupling strengths are difficult to calculate in practise, and are therefore usually determined experimentally. In this chapter, we will consider both Rashba and Dresselhaus SO coupling in our systems. Defining the normal direction of a thin film surface as the z-direction, we get a general expression for the SO field

$$\underline{\boldsymbol{A}} = (\alpha_D\underline{\sigma}_x - \alpha_R\underline{\sigma}_y, \alpha_R\underline{\sigma}_x - \alpha_D\underline{\sigma}_y, 0). \tag{3.8}$$

We can also express α_R and α_D in polar notation, as

$$\alpha_R = \alpha sin(\theta_{SO}) \quad \text{and} \quad \alpha_D = \alpha cos(\theta_{SO}), \tag{3.9}$$

where $\alpha \equiv \alpha_R^2 + \alpha_D^2$ and θ_{SO} denotes the angle between the two SO fields. Inserting this into (3.8), we get

$$\underline{\boldsymbol{A}} = \alpha^2(cos(\theta_{SO})\underline{\sigma}_x - sin(\theta_{SO})\underline{\sigma}_y, sin(\theta_{SO})\underline{\sigma}_x - cos(\theta_{SO})\underline{\sigma}_y, 0). \tag{3.10}$$

Writing out the x- and y- components of $\underline{\boldsymbol{A}}$, we see that

$$\underline{A}_x = \alpha^2 \begin{pmatrix} 0 & e^{i\theta_{SO}} \\ e^{-i\theta_{SO}} & 0 \end{pmatrix} \quad \text{and} \quad \underline{A}_y = \alpha^2 \begin{pmatrix} 0 & ie^{-i\theta_{SO}} \\ -ie^{i\theta_{SO}} & 0 \end{pmatrix}. \tag{3.11}$$

This form of the Rashba-Dresselhaus SO field is often more useful to work with, as it allows us to interpret our results in terms of the geometric properties of the SO field. In Nambu-spin space, the SO field takes the form

$$\hat{\boldsymbol{A}} = \begin{pmatrix} \underline{\boldsymbol{A}} & 0 \\ 0 & -\underline{\boldsymbol{A}}^* \end{pmatrix}. \tag{3.12}$$

Here, we take care to note that although this form of the SO field is both hatted and bold, $\hat{\boldsymbol{A}}$ is to be considered as a 4×4 matrix with a vector structure, and not as a unit vector. Adding SO-coupling to the Usadel equation in (2.34), and writing out the full gauge covariant derivative, we now get

$$iD_F(\nabla(\hat{g}^R\nabla\hat{g}^R) - i[\hat{\boldsymbol{A}}, \hat{g}^R\nabla\hat{g}^R] - i\nabla(\hat{g}^R\hat{\boldsymbol{A}}\hat{g}^R) - [\hat{\boldsymbol{A}}, \hat{g}^R\hat{\boldsymbol{A}}\hat{g}^R]) = [E\hat{\tau}_3 + \hat{\Delta} + \boldsymbol{h}\cdot\hat{\boldsymbol{\sigma}}, \hat{g}^R]. \tag{3.13}$$

Here, we have applied the normalization conditions in (2.27) and assumed that the SO field is constant in space.

There is also another way to induce SO coupling in our materials. As we will discuss more in-depth in section 4.3, materials may be curved in a way that enforces a strain on the system. This strain gives rise to an electric field in the normal direction of the curvature, which in turn results in an SO coupling that is proportional to the curvature of the material. This is why we first discuss general SO coupling in flat systems.

3.2 Weak proximity limit

At the end of section 2.3.1 we mentioned that the Usadel equation is challenging to solve in the general case, due to its nonlinear nature. However, under certain assumptions we may simplify the equation, allowing us to interpret the equation analytically under these restrictions. Through understanding how the Usadel equation behaves in the restricted cases, we may extrapolate and gain some intuition for how we expect it to behave in the general case as well. In this section, we therefore aim to simplify the Usadel equation by restricting ourselves to systems where the proximity effect is weak. In such systems a lower portion of the Cooper pairs are able to penetrate the SF interface. We therefore expect the superconductive correlations to have a weak presence in the metal. For normal metals we have $\underline{g} = 1$ and $\underline{f} = 0$. The presence of superconductive correlations is denoted by the anomalous Green's function, $\underline{f}$. In weak proximity systems, the retarded Green's function therefore simplifies as

$$\hat{g}^R = \begin{pmatrix} 1 & \underline{f} \\ -\underline{\tilde{f}} & -1 \end{pmatrix}, \tag{3.14}$$

where the anomalous Green's function is considered to be small, such that $\underline{f} \ll 1$. Inserting this into the Usadel equation in (2.33), along with adding SO coupling through gauge covariant derivatives, we get

$$iD_F \begin{pmatrix} 0 & \hat{\nabla}^2 \underline{f} \\ \hat{\nabla}^2 \underline{\tilde{f}} & 0 \end{pmatrix} = \begin{pmatrix} 0 & 2E\underline{f} + \boldsymbol{h} \cdot \underline{\boldsymbol{\sigma}}\,\underline{f} - \underline{f}\boldsymbol{h} \cdot \underline{\boldsymbol{\sigma}}^* \\ 2E\underline{\tilde{f}} - \underline{\tilde{f}}\boldsymbol{h} \cdot \underline{\boldsymbol{\sigma}} + \boldsymbol{h} \cdot \underline{\boldsymbol{\sigma}}^* \underline{\tilde{f}} & 0 \end{pmatrix}, \tag{3.15}$$

where we have ignored terms of $\mathcal{O}(\underline{f}^2)$. Because of the matrix multiplications we have performed, and the form of the SO field in Nambu-spin space, given in (3.12), the gauge covariant derivatives have changed form, $\tilde{\nabla} \to \hat{\nabla}$, where we have defined

$$\hat{\nabla} v \equiv \nabla v - i\left(\underline{\boldsymbol{A}} v + v \underline{\boldsymbol{A}}^*\right). \tag{3.16}$$

Equation (3.15) describes the dynamics in the ferromagnetic region, since we have included the exchange field, $\boldsymbol{h}$, and set the superconducting gap to zero, $\hat{\Delta} = 0$. Taking the limit where $\underline{g} = 1$ and $\underline{f}$ is small is referred to as the weak proximity limit. From (3.15) we see that we have removed the nonlinear terms, effectively linearizing the Usadel equation. We also see that the equations for $\underline{f}$ and $\underline{\tilde{f}}$ have decoupled. It is therefore sufficient to only consider the equation for $\underline{f}$ from here on, since the equation for $\underline{\tilde{f}}$ can be found by taking the tilde-conjugate of the equation for $\underline{f}$. Inserting the derivative in (3.16) into (3.15), we get [63]

$$\begin{aligned} D_F \nabla^2 \underline{f} - 2iD_F(\underline{\boldsymbol{A}} \cdot \nabla \underline{f} + \nabla \underline{f} \cdot \underline{\boldsymbol{A}}^*) - D_F(2\underline{\boldsymbol{A}} \cdot (\underline{f}\underline{\boldsymbol{A}}^*) + \underline{\boldsymbol{A}} \cdot \underline{\boldsymbol{A}}\underline{f} + \underline{f}\underline{\boldsymbol{A}}^* \cdot \underline{\boldsymbol{A}}^*) \\ = -2iE\underline{f} - i\boldsymbol{h} \cdot (\underline{\boldsymbol{\sigma}}\,\underline{f} - \underline{f}\underline{\boldsymbol{\sigma}}^*), \end{aligned} \tag{3.17}$$

where we have assumed that $\underline{\boldsymbol{A}}$ is constant in space. This assumption holds for Rashba-Dresselhaus spin-splitting in Euclidean geometries, but is generally not correct for curved geometries. This equation describes the linearized Usadel equation.

In the absence of an SO field, equation (3.17) takes the form

$$D_F \nabla^2 \underline{f} = -2iE\underline{f} - i\boldsymbol{h} \cdot (\underline{\boldsymbol{\sigma}}\,\underline{f} - \underline{f}\underline{\boldsymbol{\sigma}}^*). \tag{3.18}$$

Since the strength of the exchange field in general is much stronger than the energy E (which is of the order of the temperature T), the superconductive correlations will thus decay over a distance $\sqrt{D_F/|\boldsymbol{h}|}$. This gives rise to short-ranged correlations. If, on the other hand, terms involving the exchange field would vanish, the correlations would decay over a much longer distance $\sqrt{D_F/T}$, giving rise to long-ranged correlations [33]. In order for the exchange field-terms to vanish, the correlations $\underline{f}$ must be perpendicular to $\boldsymbol{h}$. This motivates us to parameterize $\underline{f}$ accordingly, in terms of short-ranged- and long-ranged-components, in order to investigate the dynamics of spin mixing and rotation closer.

3.2.1 Spin parameterization

We would like to be able to study the development of LRTs and SRTs from the linearized Usadel equation. In order to do this, we express $\underline{f}$ in the spin-parameterization, given by [79]

$$\underline{f} = (f_0 + \boldsymbol{d}\cdot\underline{\boldsymbol{\sigma}})i\underline{\sigma}_y. \tag{3.19}$$

This parameterization expresses $\underline{f}$ in terms of its singlet component, f_0, and its triplet components, $\boldsymbol{d}$. Here, the part of the d-vector that is parallel to the exchange field $\boldsymbol{h}$, $d_\parallel = \boldsymbol{d}\cdot\hat{\boldsymbol{h}}$, refers to the SRT component of $\underline{f}$, while the perpendicular part, $d_\perp = |\boldsymbol{d}\times\hat{\boldsymbol{h}}|$, refers to the LRT component. This parameterization of $\underline{f}$ is therefore useful for our purpose as it allows us to directly study the dynamics of the different spin-components. Inserting (3.19) and (3.10) into (3.15), and explicitly doing the matrix multiplications, we get a set of four equations

$$\nabla^2 d_x - 4\alpha^2(\cos(\theta_{SO})\partial_y - \sin(\theta_{SO})\partial_x)d_z + 4\alpha^4\sin(2\theta_{SO})d_y - 4\alpha^4 d_x = -\frac{2i}{D_F}(Ed_x + f_0 h_x), \tag{3.20}$$

$$\nabla^2 d_y - 4\alpha^2(\cos(\theta_{SO})\partial_x + \sin(\theta_{SO})\partial_y)d_z + 4\alpha^4\sin(2\theta_{SO})d_x - 4\alpha^4 d_y = -\frac{2i}{D_F}(Ed_y + f_0 h_y), \tag{3.21}$$

$$\nabla^2 d_z - 4\alpha^2\cos(\theta_{SO})(\partial_x d_y + \partial_y d_x) - 8\alpha^4 d_z - = -\frac{2i}{D_F}(Ed_z + f_0 h_z), \tag{3.22}$$

$$\nabla^2 f_0 = -\frac{2i}{D_F}(Ef_0 + \boldsymbol{h}\cdot\boldsymbol{d}). \tag{3.23}$$

This is the general expression for the linearized Usadel equations in 3D ferromagnets. In one dimension, the gradient reduces to a derivative in the z-direction, since the layering direction was defined to point in the z-direction in section 3.1. Because of this, the derivatives in the x- and y-directions vanish, and the equations (3.20)-(3.23) simplify even further, as [63]

$$\partial_z^2\boldsymbol{d} - 4\alpha^4\Omega(\theta_{SO})\boldsymbol{d} = -\frac{2i}{D_F}(E\boldsymbol{d} + f_0\boldsymbol{h}), \tag{3.24}$$

$$\partial_z^2 f_0 = -\frac{2i}{D_F}(Ef_0 + \boldsymbol{h}\cdot\boldsymbol{d}). \tag{3.25}$$

Here, we have defined the SO interaction matrix, $\Omega(\theta_{SO})$, as

$$\Omega(\theta_{SO}) = \begin{pmatrix} 1 & -\sin(2\theta_{SO}) & 0 \\ -\sin(2\theta_{SO}) & 1 & 0 \\ 0 & 0 & 2 \end{pmatrix} \tag{3.26}$$

We can now begin to interpret some results from the equations in (3.24) and (3.25). First of all, there has not been made a choice for the direction of the exchange field in these equations, but we recall that $d_{srt} \equiv d_\parallel = \boldsymbol{d}\cdot\hat{\boldsymbol{h}}$ and $d_{lrt} \equiv d_\perp = |\boldsymbol{d}\times\hat{\boldsymbol{h}}|$ denotes SRTs and LRTs, respectively. Because of this, we see that (3.25) describes the generation of SRTs from the singlet state, due to the exchange field. We see that this process of spin-mixing is independent of the SO-field, as predicted in the introduction to this chapter. Furthermore, equation (3.24) describes the generation of LRTs from SRTs, due to the SO interaction matrix. We called this process spin-rotation. We see that spin rotation is not possible for $\theta_{SO} = n\pi/2$, for $n = 1, 2, 3...$, since $\Omega(\theta_{SO})$ diagonalizes for these values. This tells us that we need both Rashba and Dresselhaus SO fields, as well as a finite angle

between these two fields, in order to generate LRTs with SO coupling in the xy-plane. The form of $\Omega(\theta_{SO})$ also indicates that we need a finite exchange field in the xy-plane in order to generate LRTs.

Generally, the condition for spin rotation is that the SO field $\hat{\boldsymbol{A}}$ does not commute with the ferromagnetic self energy, $\boldsymbol{h}\cdot\hat{\boldsymbol{\sigma}}$ [80]. Hence, it should be noted that spin rotation is possible for pure Rashba SO coupling, if the orientation or structure of the SO field is different from that in (3.8). We will, for example, show that generation of LRTs is possible for a system with both an exchange field and SO field pointing in the z-direction [81].

If we look at the 3D equations in (3.20)-(3.23), the terms we removed in the transition from 3D to 1D systems all include first order derivatives of the d-vector components. These terms also describe generation of LRTs, but are damping like in nature. Following the discussion in Bergeret & Tokatly (2014) [33], we call this kind of spin rotation *precession*. This form of spin-rotation will therefore still be present in higher-dimensional materials with only one type of SO coupling.

3.3 Physical observables

The physical observables of interest in this thesis is mainly the density of states (DoS) and the charge current. Both can be expressed in terms of the retarded Green's function matrix, $\hat{g}^R$.

3.3.1 Density of states

The density of states $N(\boldsymbol{R}, E)$ is found from the spectral function, and is given by [61]

$$N_\sigma(\boldsymbol{R}, E) = \lim_{\boldsymbol{r}\to 0} -\frac{1}{\pi}\mathrm{Im}\{\underline{G}^R_{\sigma\sigma}(\boldsymbol{R}, \boldsymbol{r}, E)\}. \tag{3.27}$$

Expressing this in terms of the quasiclassical Green's function using (2.20), we get

$$D_\sigma(\boldsymbol{R}, E) = \mathrm{Re}\{\underline{g}^R_{\sigma\sigma}(\boldsymbol{R}, E)\}. \tag{3.28}$$

Here, we have defined the normalized density of states as $D(\boldsymbol{R}, E) = N(\boldsymbol{R}, E)/N_0$, where N_0 denotes the density of states at the Fermi surface. In this thesis we are generally not interested in the density of states of separate spin components. We may thus take the average in spin space

$$D(\boldsymbol{R}, E) = \frac{1}{2}\mathrm{Re}\{\mathrm{Tr}[\underline{g}^R(\boldsymbol{R}, E)]\}. \tag{3.29}$$

We note that the traces in these expressions are all taken with respect to the first quadrant in $\hat{g}^R$. Thus, these expressions for the density of states are for the electron-part of the quasiparticles. In order to find the density of states for the holes we should take the trace of the 4^{th} quadrant, given by $-\underline{\tilde{g}}^R$.

We may also express the density of states at zero energy in terms of the singlet component and the triplet vector from the spin parameterization in (3.19). Using the normalization condition $\hat{g}^R\hat{g}^R = \hat{\tau}_0$, we see that $\underline{g}^R\underline{g}^R = 1 + \underline{f}^R\underline{\tilde{f}}^R$. At zero energy, the tilde-conjugate reduces to a regular conjugate, giving $\underline{g}^R\underline{g}^R = (1 - |f_0|^2 + |\boldsymbol{d}|^2)\underline{I}$, after

writing $\underline{f}^R$ in the spin-parameterization. Thus, the density of states at zero energy is given by

$$D(\boldsymbol{R}, E=0) = \sqrt{1 - |f_0|^2 + |\boldsymbol{d}|^2}. \tag{3.30}$$

In the weak proximity limit, where $\underline{f} \ll 1$, this can be written as [11]

$$D(\boldsymbol{R}, E=0)_{wpl} = 1 - \frac{1}{2}|f_0(\boldsymbol{R}, 0)|^2 + \frac{1}{2}|\boldsymbol{d}(\boldsymbol{R}, 0)|^2. \tag{3.31}$$

Here, we see how the presence of triplet- and singlet-state components affect the density of states at zero energy, allowing us to more easily interpret the results we get. For example, a pronounced peak in the density of states at $E = 0$ often indicates the presence of triplets, and LRTs in particular, while a gap around $E = 0$ indicates the presence of singlets. It should be noted that the singlets and triplets can cancel each other out in the density of states. Furthermore, this approach does not let us separate between LRTs and SRTs. Therefore, it is useful to plot the absolute values of the singlet and d-vector components in order to properly analyze the extent of the spin mixing and rotation.

3.3.2 Charge current

The charge current density must obey the continuity equation given by

$$\partial_t \rho_q(\boldsymbol{r}) = -\nabla \cdot \boldsymbol{J}_q(\boldsymbol{r}), \tag{3.32}$$

where $\rho_q(\boldsymbol{r})$ denotes the charge density, and $\boldsymbol{J}_q(\boldsymbol{r})$ denotes the charge current density. Wanting to express this equation in the Green's function formalism, we write the charge density in terms of field operators

$$\rho_q(\boldsymbol{r}) = e\Sigma_\sigma \langle \psi_\sigma^\dagger(\boldsymbol{r})\psi_\sigma(\boldsymbol{r})\rangle. \tag{3.33}$$

This expression can now be inserted into the continuity equation, which can be manipulated in order to give us the following expression for the normalized charge current density [66]

$$\boldsymbol{j}_q(\boldsymbol{R}) = \frac{eD_F}{4}\int dE \mathrm{Tr}[\hat{\tau}_z(\hat{g}^K\tilde{\nabla}\hat{g}^K)], \tag{3.34}$$

where the normalized charge current density is related to the charge current density by $\boldsymbol{j}_q(\boldsymbol{R}) = \boldsymbol{J}_q(\boldsymbol{r})/N_0$. We recall that $\hat{g}^K$ can be expressed in terms of $\hat{g}^R$ using (2.17), giving us an expression for the charge current density in terms of the retarded Green's function matrix

$$\boldsymbol{j}_q(\boldsymbol{R}) = \frac{eD_F}{4}\int dE \tanh\left(\frac{E}{2T}\right)\mathrm{Tr}[\hat{\tau}_z(\hat{g}^R\tilde{\nabla}\hat{g}^R + (\hat{\tau}_z\hat{g}^R\tilde{\nabla}\hat{g}^R\hat{\tau}_z)^\dagger)]. \tag{3.35}$$

3.4 The bulk superconductor

In order to better understand SF proximity systems, it is instructional to first consider an isolated superconductor. We therefore look at a bulk superconductor, and its solution to the Usadel equation. By a bulk superconductor, we mean a superconductor with an

infinite extension in each direction of propagation. In a superconductor, the Green's function is constant in space, and we consider the SO effects to be localized within the ferromagnet. The Usadel equation in (2.34) thus reduces to a simple commutator equation

$$[E\hat{\tau}_3 - \hat{\Delta}, \hat{g}^R] = 0. \tag{3.36}$$

We notice that this equation is independent of dimensionality, such that the solutions for 1D, 2D and 3D are all the same. The solution can be shown to be [61]

$$\hat{g}_{SC} = \begin{pmatrix} \frac{E}{\sqrt{E^2-|\Delta|^2}} & \frac{\Delta}{\sqrt{E^2-|\Delta|^2}} i\underline{\sigma}_y \\ \frac{\Delta^*}{\sqrt{E^2-|\Delta|^2}} i\underline{\sigma}_y & -\frac{E}{\sqrt{E^2-|\Delta|^2}} \end{pmatrix}. \tag{3.37}$$

By defining the angle $\theta_{SC} = \text{atanh}(|\Delta|/E)$, and writing the superconducting gap in terms of its magnitude and phase, $\Delta = |\Delta|e^{i\phi}$, we can rewrite the solution to

$$\hat{g}_{SC} = \begin{pmatrix} \cosh(\theta_{SC}) & \sinh(\theta_{SC}) i\underline{\sigma}_y e^{i\phi} \\ \sinh(\theta_{SC}) i\underline{\sigma}_y e^{-i\phi} & -\cosh(\theta_{SC}) \end{pmatrix}. \tag{3.38}$$

Here, we have written the solution in terms of hyperbolic functions, where $\cosh(\theta_{SC}) = \frac{E}{\sqrt{E^2-|\Delta|^2}}$ and $\sinh(\theta_{SC}) = \frac{\Delta}{\sqrt{E^2-|\Delta|^2}}$. Inserting this solution into the density of states in (3.29) gives

$$D_{SC}(E) = \frac{|E|}{\sqrt{E^2-|\Delta|^2}} H(E^2 - |\Delta|^2), \tag{3.39}$$

where $H(x)$ denotes the heaviside function, indicating that there is a gap where $D_{SC}(E) = 0$ for $E < \Delta$. Furthermore, $D_{SC}(E)$ features so-called *coherence peaks* at $E = \Delta$. The density of states for the bulk of a superconductor is plotted in figure 3.2, together with the density of states for a normal metal, for comparison.

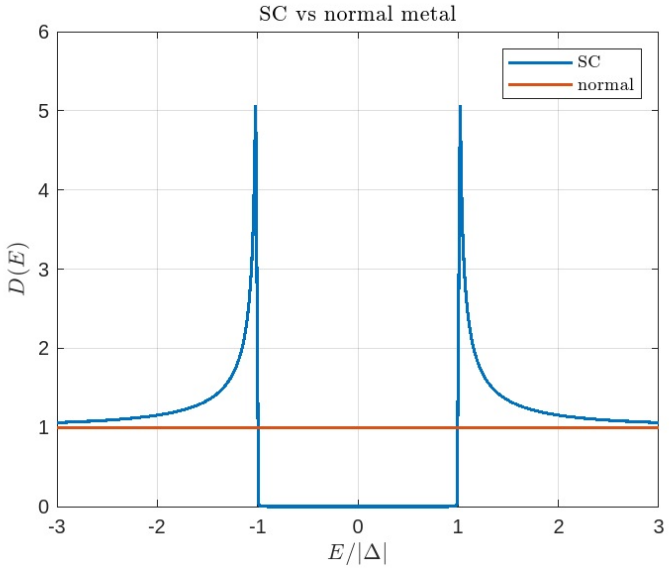

Figure 3.2: The normalized density of states for a bulk superconductor (SC) and a normal metal.

3.5 SO coupling in SF systems

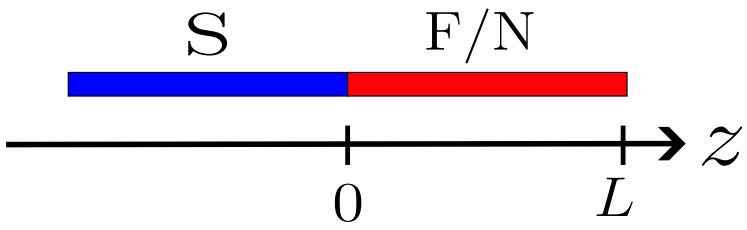

Figure 3.3: Visualization of our proximity system. The blue region represents a superconducting reservoir, while the red region represents the ferromagnet/normal metal, with length L.

In order to verify our findings in section 3.1 we have solved the general Usadel equation in 2.34 numerically. The main tools used to solve this equation numerically are covered in section 6.2. In this section, we consider 1D systems in the form shown in figure 3.3. That is, we are dealing with nanowire-like metals in contact with a superconducting reservoir to the left. The length of the metal is set to be equal to the superconducting coherence length, $L = \xi$, where we use the relation $\xi = \sqrt{D_F/|\Delta|}$ for the coherence length [82].

Figure 3.4(a) shows the density of states for an SN system, compared to an SF system. The SN system features a gap in the density of states around $E = 0$, while the SF system is identical to the normal metal in figure 3.2 close to $E = 0$. We can understand these results by looking at the expression for the density of states in (3.31). This tells us that the gap in the SN system is due to the presence of singlet states in the normal metal, due to the proximity effect. This is expected, as the normal metal features no exchange field, and therefore will not destroy the singlet state correlations. The SF system, on the other hand, can be seen to have no singlet states. We thus see that the exchange field has destroyed the singlet states, and most of the proximity effect, making the density of states look like a normal metal around $E = 0$.

Figure 3.5(a) shows the density of states for SF systems with $\theta_{SO} = \pi/4$ and $\theta_{SO} = 0$, respectively. This plot thus demonstrates the effect of the SO angle on the density of states. In section 3.1 we predicted that a finite SO angle is necessary in order to produce LRTs for SO fields in the form in 3.12. This is shown to be correct, as $\theta_{SO} = \pi/4$ gives a clear peak at $E = 0$ in the density of states, indicating the presence of LRTs, while $\theta_{SO} = 0$ gives a gap in the density of states. The plot in figure 3.5(b) verifies that this peak is due to LRTs in the ferromagnet. In this figure, we have plotted the absolute value of the LRT (d_{LRT}), SRT (d_{SRT}) and singlet (f_0) components for a system with length $L = 5\xi$, at $E = 0$. This figure hence demonstrates the long range effect of LRTs, along with demonstrating how singlet and SRT components are destroyed in the case where there is no spin-rotation. We note that the singlet component in the $\theta_{SO} = \pi/4$ case seems to have a long range penetration, which seems odd at first glance. This can be explained by noting that spin-rotation and spin-mixing go both ways, according to the weak proximity equation in (3.24). By this, we mean that we can also generate singlet components from SRTs, which in turn can be generated from LRTs. This means that we may have generation of singlet components far into the ferromagnet, since the LRTs will be present at these depths.

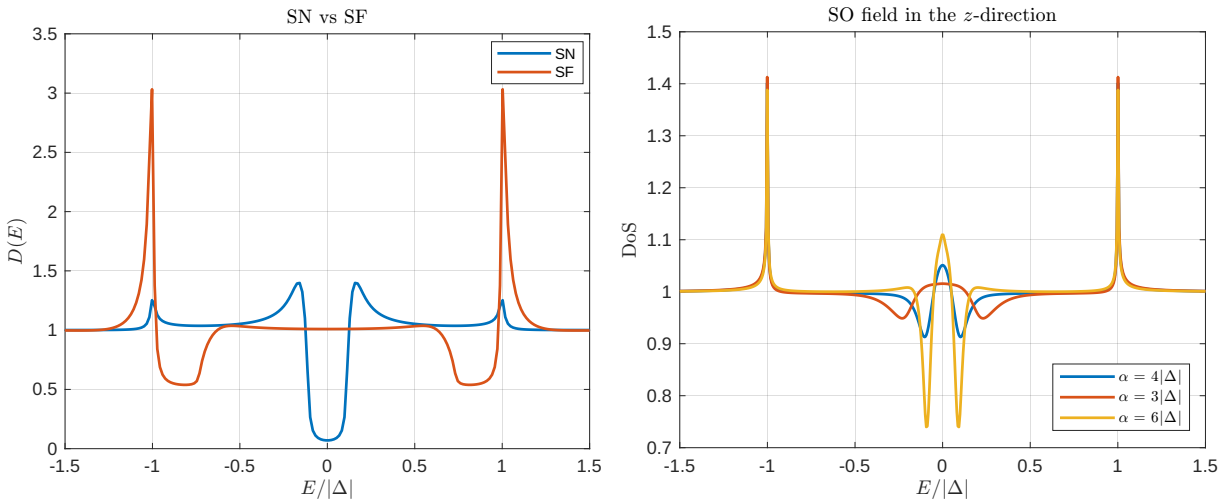

(a) (b)

Figure 3.4: (a) The normalized density of states for a superconductor - normal metal (SN) proximity system and a superconductor - ferromagnet (SF) proximity system. The length and relative resistance is $L = \xi$ and $\zeta = 3$ in both systems. The exchange field is $\boldsymbol{h} = |\Delta|[\cos(\pi/6), -\sin(\pi/6), 0]$ in the ferromagnet. (b) Density of states for an SF proximity system with SO field in the z-direction, for various coupling strengths. The exchange field is $\boldsymbol{h} = |\Delta|\hat{\boldsymbol{z}}$ and the length is $L = 2\xi$.

Finally, we show that spin rotation is possible for a pure Rashba coupling in the z-direction in figure 3.4(b). Here, we have plotted the density of states for an SF system with exchange field $\boldsymbol{h} = |\Delta|\hat{\boldsymbol{z}}$ and SO field $\underline{\boldsymbol{A}} = \alpha(\underline{\sigma}_x - \underline{\sigma}_y)\hat{\boldsymbol{z}}$, with $L = 2\xi$, for various coupling constants. We see that the peaks around zero energy indicate LRTs, and that the peak is more prominent for stronger coupling constants.

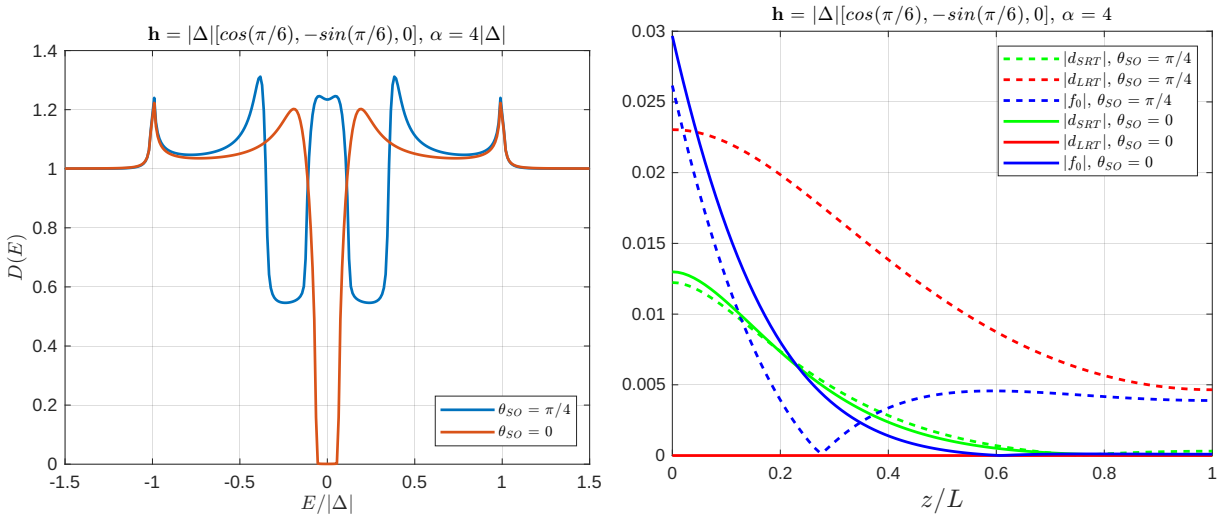

(a) (b)

Figure 3.5: (a) The normalized density of states for a superconductor-ferromagnet proximity system with SO coupling. One system with SO angle $\theta_{SO} = \pi/4$ and one with $\theta_{SO} = 0$. $L = \xi$, $\zeta = 3$, $\boldsymbol{h} = |\Delta|[\cos(\pi/6), -\sin(\pi/6), 0]$ and $\alpha = 4|\Delta|$. (b) The absolute value of the LRT, SRT and singlet components plotted along the ferromagnet at $E = 0$, for the two systems considered in (a).

4 Curvature in 1D

We will now add geometric curvature to our systems. The geometric curvature will not only be shown to have similar effects on our systems as SO-coupling, but also introduce new possible mechanics. The idea that curving a material in space can change its ability to transport particles so drastically seems odd at first glance. One of the most lucid ways to explain why this works is to consider a 1D ferromagnetic wire, with its exchange field pointing along the direction of propagation. The Cooper pairs entering this wire from a superconductor attached to either side will decay rapidly as singlets or short-range triplets. If we now curve this wire, the exchange field orients itself along the tangential direction of the curve for a large class of materials [83]. This curved wire can now be mapped to a straight wire, with an exchange field that rotates according to the curvature, as shown in figure 4.1. The Cooper pairs entering the wire from the superconductor now see a spatially rotating exchange field as they move along the wire. As discussed in Bergeret & Tokatly (2014) [33], a spatially varying exchange field can be shown to be equivalent to a general SO-field when it comes to producing long-range triplets. Furthermore, geometric curvature can also induce SO-coupling in the material through symmetry breaking and strain.

In order to understand how curvatures affect transportation of superconductive correlations in 2D materials, it is useful to first gain some intuition for how curvatures influence 1D materials. Having some results established for 1D systems will also make it easier to interpret and understand results from 2D systems.

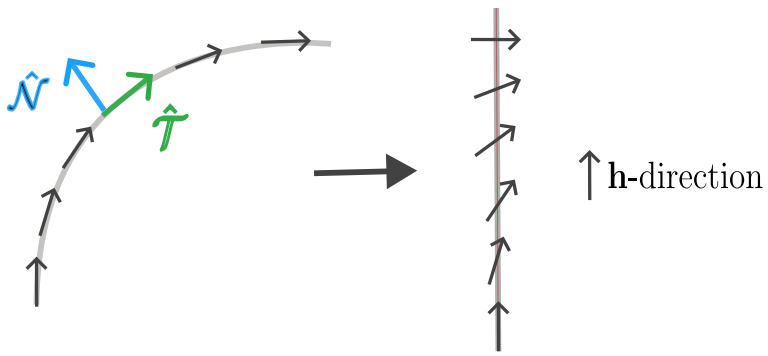

Figure 4.1: A curved nanowire with an exchange field pointing along the tangential direction mapped to a straight nanowire with a rotating exchange field.

4.1 An introduction to tensor notation

In order to describe the geometries of curved surfaces it is natural to employ a coordinate system that follows the surface implicitly. Such choices of coordinate systems generally distinguish themselves from the usual choice of Cartesian coordinates in that the basis vectors may vary in space. That is, a basis vector in some point a on the surface might not point in the same direction at another point b. Furthermore, it is important for our equations to express the same physical properties, regardless of what coordinate system we are employing. It is for these reasons that we utilize the tensor formalism in our treatment of geometric curvature. Tensors are quantities that transform in specific ways

under coordinate transformations. Expressing equations in terms of tensors thus gives us control over how these equations transform with respect to a change in coordinates. This allows us to compose equations in ways that look the same, regardless of frame of reference, giving our equations the quality we are looking for in order to describe dynamics on surfaces.

To begin this discussion, let us consider a general 3D coordinate vector, $\boldsymbol{R}(x_1, x_2, x_3)$, that traces out the whole 3D space. This vector takes on different forms depending on our choice of coordinates, and our choice of coordinates depends on the geometries we would like to describe. For example, we have $\boldsymbol{R}(x, y, z) = x\hat{\boldsymbol{x}} + y\hat{\boldsymbol{y}} + z\hat{\boldsymbol{z}}$ in Cartesian coordinates and $\boldsymbol{R}(r, \theta, z) = r\cos(\theta)\hat{\boldsymbol{x}} + r\sin(\theta)\hat{\boldsymbol{y}} + z\hat{\boldsymbol{z}}$ in cylindrical coordinates. From this vector we would like to define a set of basis vectors, $\{\boldsymbol{e}_i\}$. We do this by defining the i^{th} basis vector as [84]

$$\boldsymbol{e}_i = \partial_i \boldsymbol{R}(x_1, x_2, x_3), \tag{4.1}$$

where ∂_i denotes the partial derivative with respect to the i^{th} coordinate. This definition has an intuitive explanation. As we change only the i^{th} variable in $\boldsymbol{R}$, we would like to move in the direction of the i^{th} basis vector. This is exactly what the definition in (4.1) ensures. This definition raises several possible problems. First of all this set of basis vectors is not necessarily normalized, nor orthogonal. Furthermore, the inner product between two arbitrary vectors, $\boldsymbol{A} = a^i\boldsymbol{e}_i$ and $\boldsymbol{B} = b^i\boldsymbol{e}_i$, seemingly depends on our choice of coordinates. To see this, consider the same basis vector as in (4.1), but in another coordinate system, defined by a set of coordinates x_i'. The relation between $\boldsymbol{e}_i$ and $\boldsymbol{e}_i'$ is thus

$$\boldsymbol{e}_i' = \frac{\partial \boldsymbol{R}}{\partial x_i'} = \frac{\partial \boldsymbol{R}}{\partial x_i}\frac{\partial x_i}{\partial x_i'} = \frac{\partial x_i}{\partial x_i'}\boldsymbol{e}_i. \tag{4.2}$$

This issue can be resolved if we compare the inner products between $\boldsymbol{A}$ and $\boldsymbol{B}$ in two different coordinate systems. We see that

$$\boldsymbol{A} \cdot \boldsymbol{B} = a^i b^j \boldsymbol{e}_i \cdot \boldsymbol{e}_j, \tag{4.3}$$

whereas the inner product in the primed coordinate system is

$$\boldsymbol{A}' \cdot \boldsymbol{B}' = a'^i b'^j \boldsymbol{e}_i' \cdot \boldsymbol{e}_j' = a'^i b'^j \frac{\partial x_i}{\partial x_i'}\frac{\partial x_j}{\partial x_j'}\boldsymbol{e}_i \cdot \boldsymbol{e}_j. \tag{4.4}$$

We see that in order for the inner product to be independent of our choice of coordinates, the coefficients with raised indices, a^i and b^i, must transform as

$$a'^i = \frac{\partial x_i'}{\partial x_i} a^i \tag{4.5}$$

under a change of coordinates.

We define vectors that follow the transformation rule outlined in (4.5) as *contravariant* vectors, while vectors that follow the transformation rule in (4.2) are called *covariant* vectors. Contravariant vectors are denoted by having raised indices, while covariant vectors have lowered indices. This explains the positioning of the indices so far. Following our argumentation so far, a general vector can be written as a product of covariant and contravariant vectors

$$\boldsymbol{A} = A^i \boldsymbol{e}_i = A_i \boldsymbol{e}^i. \tag{4.6}$$

We now suddenly have two sets of basis vectors, a set of covariant basis vectors $\{\boldsymbol{e}_i\}$, and a set of contravariant basis vectors $\{\boldsymbol{e}^i\}$. Both are valid choices of basis vectors for a general coordinate vector $\boldsymbol{R}$, and as shown this far, both are needed in order for our inner products to be physically meaningful. Both sets are therefore utilized, and we call this doubled set of basis vectors a dual set of basis vectors, where $\{\boldsymbol{e}_i\}$ and $\{\boldsymbol{e}^i\}$ are *dual basis vectors*. Dual basis vectors are related by

$$\boldsymbol{e}_i \boldsymbol{e}^i = \delta_i^j, \tag{4.7}$$

where δ_i^j denotes the Kronecker delta. Thus, this dual set of contravariant and covariant basis vectors form an orthonormal set of basis vectors, which resolves the problems previously discussed, related to orthonormality. From (4.7) and (4.6) we see that we can write general vectors on covariant and contravariant form as

$$A_i = \boldsymbol{A} \cdot \boldsymbol{e}_i \quad \text{and} \quad A^i = \boldsymbol{A} \cdot \boldsymbol{e}^i. \tag{4.8}$$

In order to utilize this set of basis vectors we need to be able to convert between covariant and contravariant vectors. To do this, we return to the inner product, and see that we can write this in two different ways. Using the two different expressions in (4.6) we get

$$\boldsymbol{A} \cdot \boldsymbol{B} = (A^i \boldsymbol{e}_i) \cdot (B^j \boldsymbol{e}_j) = (A_i \boldsymbol{e}^i) \cdot (B^j \boldsymbol{e}_j) = A_j B^j. \tag{4.9}$$

This suggests that

$$A_i = \boldsymbol{e}_i \cdot \boldsymbol{e}_j A^j = g_{ij} A^j, \tag{4.10}$$

where we have defined the important *metric tensor*, defined by

$$g_{ij} = \boldsymbol{e}_i \cdot \boldsymbol{e}_j. \tag{4.11}$$

Similarly, we can show that

$$A^i = \boldsymbol{e}^i \cdot \boldsymbol{e}^j A_j = g^{ij} A_j. \tag{4.12}$$

Combining (4.10) and (4.12), we see that $A^i = g^{ij} A_j = g^{ij} g_{jk} A^k$, which implies that

$$g^{ij} g_{jk} = \delta_k^i. \tag{4.13}$$

Thus, g^{ij} is shown to be the inverse of the metric tensor. The operations outlined in (4.10) and (4.12) are referred to lowering and raising of indices, respectively, and are frequently encountered in calculations involving covariant and contravariant vectors.

The metric tensor is thus central to our formalism, as it allows us to convert between covariant and contravariant vectors and evaluate inner products. This indicates that the metric tensor is linked to the measurement of physical distances, hence its name. From its definition, we see that g_{ij} is symmetrical, such that $g_{ij} = g_{ji}$. Furthermore, the metric tensor becomes diagonal for orthogonal coordinate systems. This indicates that orthogonal coordinate systems are preferred to use if possible, as they simplify the inner product and the covariant-contravariant vector relation.

For orthogonal systems we can also introduce a new type of vector, the *physical* vector. The i^{th} component of the physical vector A is given by $A_{(i)}$. Its definition can be found by considering the inner product between two general vectors

$$\boldsymbol{A} \cdot \boldsymbol{B} = g^{ii} A_i B_i = A_{(i)} B_{(i)}. \tag{4.14}$$

Here, we have used that the metric tensor is diagonal for orthogonal systems. From this definition, we can see that

$$A_{(i)} = \frac{A_i}{\sqrt{g_{ii}}} = A_i / h_i, \tag{4.15}$$

where $h_i = \sqrt{g_{ii}} = |\boldsymbol{e}_i|$ is referred to as a scale factor. h_i has the role of ensuring that the physical vector component $A_{(i)}$ has the right dimension. For example, in polar coordinates

$$\boldsymbol{e}_r = \cos(\theta)\hat{\boldsymbol{x}} + \sin(\theta)\hat{\boldsymbol{y}} \quad \text{and} \quad \boldsymbol{e}_\theta = -r\sin(\theta)\hat{\boldsymbol{x}} + r\cos(\theta)\hat{\boldsymbol{y}} \tag{4.16}$$

have different dimensions due to the factor r. Thus, $\boldsymbol{e}_\theta$ is divided by $h_\theta = r$ in order to get the correct physical dimensions, hence the name *physical* vectors. This definition is useful when wanting to describe vectors as they actually appear in physical systems.

4.1.1 The coordinate covariant derivative

We now need a way to define differentiation in this formalism. In the dual basis there are two ways of taking the derivative. The first is with respect to the component of a covariant vector x_i. This derivative can be shown to transform contravariantly under a coordinate transformation. Conversely, taking the derivative with respect to the component of a contravariant vector x^i transforms covariantly. This motivates us to define covariant derivatives, denoted by ∂_i, and contravariant derivatives, denoted by ∂^i, as

$$\partial_i A = \frac{\partial A}{\partial x^i} \quad \text{and} \quad \partial^i A = \frac{\partial A}{\partial x_i}. \tag{4.17}$$

These derivatives obey the rules that we have already established for general covariant and contravariant vectors.

If we now try to take, for example, the covariant derivative with respect to a general vector $\boldsymbol{A}$ in the dual basis, we get

$$\partial_i \boldsymbol{A} = (\partial_i A_j)\boldsymbol{e}^j + A_j(\partial_i \boldsymbol{e}^j). \tag{4.18}$$

Due to the fact that the coordinate system has the potential to change as we move around in space, we get additional terms in our derivatives. In order to keep the tensorial form of the derivative, we would like to absorb this new term into our definition of the derivative of a vector. Continuing from (4.18), we see that

$$\begin{aligned} \partial_i \boldsymbol{A} &= (\partial_i A_j)\boldsymbol{e}^j + A_k(\partial_i \boldsymbol{e}^k) \\ &= (\partial_i A_j - \Gamma^k_{ij} A_k)\boldsymbol{e}^j \\ &= (\mathcal{D}_i A_j)\boldsymbol{e}^j \end{aligned} \tag{4.19}$$

Here we have defined a new quantity, Γ^k_{ij}, known as the *Christoffel symbol*, or the *affine connection*, as

$$\partial_i \boldsymbol{e}^j = -\Gamma^j_{ik}\boldsymbol{e}^k \quad \text{or} \quad \partial_i \boldsymbol{e}_j = \Gamma^k_{ij}\boldsymbol{e}_k. \tag{4.20}$$

We have also absorbed the additional terms in (4.18) into a new derivative, known as the *coordinate covariant derivative*, $\mathcal{D}_i$ [85]. This derivative takes different forms depending on whether we are differentiating a covariant or contravariant vector. We get two definitions

$$\mathcal{D}_i A_j = \partial_i A_j - \Gamma^k_{ij} A_k, \tag{4.21}$$

$$\mathcal{D}_i A^j = \partial_i A^j + \Gamma^j_{ik} A_k. \tag{4.22}$$

The Christoffel symbols completely encapsulate the effect of a changing coordinate system on the derivative, and are therefore central quantities when dealing with dynamics in changing coordinate systems. Most of the effects of curvature on our systems can therefore be written in terms of Christoffel symbols. We therefore offer another, equivalent way, to calculate these symbols

$$\Gamma^k_{ij} = \frac{1}{2} g^{kl} \left(\partial_j g_{li} + \partial_i g_{lj} - \partial_l g_{ij} \right). \tag{4.23}$$

As can be seen from these definitions, the Christoffel symbols are symmetrical in their lower indices, i.e. $\Gamma^k_{ij} = \Gamma^k_{ji}$. The number of Christoffel symbols also scale with the dimensionality of the system D, as D^D. Thus we have 1 Christoffel symbol in 1D, 8 symbols in 2D and 27 symbols in 3D.

Using the vector definition in (4.6), the gradient vector can now be found to be

$$\nabla = \boldsymbol{e}^i \frac{\partial}{\partial q^i} = \boldsymbol{e}^i \partial_i = \boldsymbol{e}_i \partial^i. \tag{4.24}$$

The divergence is given by

$$\nabla \cdot \boldsymbol{A} = (\boldsymbol{e}^i \partial_i) \cdot \boldsymbol{A} = g^{ij} \mathcal{D}_i A_j, \tag{4.25}$$

where we used (4.19) and (4.24). Inserting these expressions into the Usadel equation in (2.34), and applying tensor notation, we get

$$iD_F g^{ij} \left(\partial_i (\hat{g}^R \partial_j \hat{g}^R) - \Gamma^k_{ij} \hat{g}^R \partial_k \hat{g}^R \right) = [E\hat{\tau}_z + \hat{\Delta} + g^{ij} h_i \hat{\sigma}_j, \hat{g}^R]. \tag{4.26}$$

Equation (4.26) is thus the general expression for the Usadel equation in tensor notation.

The cross product in general notation is given by $\boldsymbol{A} \times \boldsymbol{B} = \epsilon_{ijk} \hat{\boldsymbol{x}}_i A_j B_k$, where $\hat{\boldsymbol{x}}_i$ denotes the i^{th} orthonormalized basis vector. To write this on tensor form, we have to write the Levi-Civita symbol as a tensor. The Levi-Civita tensor is given by $\mathcal{E}_{ijk} = \epsilon_{ijk}\sqrt{|g|}$, and its contravariant form is $\mathcal{E}^{ijk} = \epsilon^{ijk}/\sqrt{|g|}$ [86]. The cross product on tensor form is now found to be

$$\boldsymbol{A} \times \boldsymbol{B} = \mathcal{E}_{ijk} \boldsymbol{e}^i A^j B^k = \mathcal{E}^{ijk} \boldsymbol{e}_i A_j B_k. \tag{4.27}$$

From this, the curl can be shown to be

$$\begin{aligned} \nabla \times \boldsymbol{A} &= \mathcal{E}^{ijk} \boldsymbol{e}_i \mathcal{D}_j A_k \\ &= \mathcal{E}^{ijk} \boldsymbol{e}_i (\partial_j A_k - \Gamma^l_{jk} A_l) \\ &= \mathcal{E}^{ijk} \boldsymbol{e}_i \partial_j A_k, \end{aligned} \tag{4.28}$$

where we have used that the Christoffel symbol is symmetric under permutation of the two lower indices j and k, while the Levi-Civita symbol is anti-symmetric under permutation of the same symbols. The terms including the Christoffel symbol thus vanish from the curl. Here, we take precaution to note that the curl, as defined in (4.28), involves derivatives of covariant vectors. The expressions for the curl that one will see in most textbooks are written in normal form, such as the expression for the curl in spherical coordinates, given by [76]

$$\nabla\times\boldsymbol{A} = \frac{1}{\sin(\theta)r}\left(\partial_\theta(\sin(\theta)A_\phi) - \partial_\phi A_\theta\right)\hat{\boldsymbol{r}} + \frac{1}{r}\left(\frac{1}{\sin(\theta)}\partial_\phi A_r - \partial_r(rA_\phi)\right)\hat{\boldsymbol{\theta}} + \frac{1}{r}\left(\partial_r(rA_\theta) - \partial_\theta A_r\right)\hat{\boldsymbol{\phi}}. \tag{4.29}$$

In order to retrieve these expressions from the definition in (4.28), one simply has to write the equation in terms of the physical vectors

$$\nabla \times \boldsymbol{A} = \epsilon^{ijk}\frac{1}{\sqrt{|g|}}\hat{\boldsymbol{x}}_i h_i \partial_j (h_k A_{(k)}). \tag{4.30}$$

4.2 Curvilinear coordinates

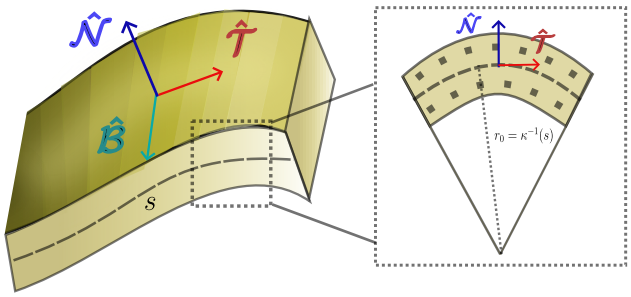

Figure 4.2: A curved surface, represented in curvilinear coordinates. This figure demonstrates how curvature stretches the material where $n > 0$ and compresses the material where $n < 0$, giving rise to strain.

The standard coordinate system used to describe curvatures in the 1D limit is curvilinear coordinates. In one dimension, curvature can be described by a general curvature $\boldsymbol{\gamma}(s)$. This curvature is said to be one dimensional, as it only depends on a single parameter s. The curvilinear coordinate system is defined by the set of basis vectors [67]

$$\hat{\boldsymbol{\mathcal{T}}}(s) = \partial_s \boldsymbol{\gamma}(s), \tag{4.31}$$
$$\hat{\boldsymbol{\mathcal{N}}}(s) = \partial_s \hat{\boldsymbol{\mathcal{T}}}(s)/|\partial_s \hat{\boldsymbol{\mathcal{T}}}(s)|, \tag{4.32}$$
$$\hat{\boldsymbol{\mathcal{B}}}(s) = \hat{\boldsymbol{\mathcal{T}}}(s) \times \hat{\boldsymbol{\mathcal{N}}}(s), \tag{4.33}$$

where $\hat{\boldsymbol{\mathcal{T}}}(s)$ is the *tangential* vector to the curve $\boldsymbol{\gamma}(s)$, $\hat{\boldsymbol{\mathcal{N}}}(s)$ is the *normal* vector, pointing normally to the tangential vector, and $\hat{\boldsymbol{\mathcal{B}}}(s)$ is the *binormal* vector, as shown in figure 4.2. From the definition in (4.31), $\hat{\boldsymbol{\mathcal{T}}}(s)$ is not necessarily a unit vector. In order to ensure that

it is, we need to choose the right parameterization for $\boldsymbol{\gamma}$. To find the parameterization of $\boldsymbol{\gamma}$ that makes $\hat{\boldsymbol{\mathcal{T}}}(s)$ a unit vector for all s, consider first a general parameterization, $\boldsymbol{\gamma}(t)$. We want to find a parameterization s, such that $|\partial_s \boldsymbol{\gamma}| = |\frac{\partial t}{\partial s}\partial_t \boldsymbol{\gamma}| = 1$. It follows that $\frac{\partial s}{\partial t} = |\partial_t \boldsymbol{\gamma}|$. By integrating this equation, we see that the parameterization s is indeed the arc-length of the curve $\boldsymbol{\gamma}$, given by

$$s = \int_0^{t'} |\partial_t \boldsymbol{\gamma}| dt. \tag{4.34}$$

Thus, in order for the curvilinear basis vectors to be unit vectors, the curve γ needs to be parameterized by its arc-length, s. We call curves that are parameterized in this manner *unit-speed* curves, as their derivative is equal to unity at all points [87].

$\hat{\boldsymbol{\mathcal{T}}}(s)$, $\hat{\boldsymbol{\mathcal{N}}}(s)$, and $\hat{\boldsymbol{\mathcal{B}}}(s)$ are all related by the *Frenet-Serret* formulas. The Frenet-Serret formulas are given by the set of equations

$$\begin{pmatrix} \partial_s \hat{\boldsymbol{\mathcal{T}}} \\ \partial_s \hat{\boldsymbol{\mathcal{N}}} \\ \partial_s \hat{\boldsymbol{\mathcal{B}}} \end{pmatrix} = \begin{pmatrix} 0 & \kappa(s) & 0 \\ -\kappa(s) & 0 & \tau(s) \\ 0 & -\tau(s) & 0 \end{pmatrix} \begin{pmatrix} \hat{\boldsymbol{\mathcal{T}}} \\ \hat{\boldsymbol{\mathcal{N}}} \\ \hat{\boldsymbol{\mathcal{B}}} \end{pmatrix}. \tag{4.35}$$

Here, we have defined the curvature of the system as $\kappa(s) = |\partial_s \hat{\boldsymbol{\mathcal{T}}}(s)|$. Thus, $\kappa(s) = 0$ for a straight line, while $\kappa(s)$ increases as $\hat{\boldsymbol{\mathcal{T}}}(s)$ varies more rapidly along the curve. This justifies our definition of the curvature. $\tau(s) = |\partial_s \hat{\boldsymbol{\mathcal{B}}}(s)|$ refers to the torsion of the curve. Torsion in a curve arises, for example, when twisting the endpoints of the curve in opposite directions, around its own axis. Conjoined with the regular curvature $\kappa(s)$, this gives rise to helical structures. Torsion complicates the computation of the metric tensor and the Christoffel symbols substantially. These computations are covered by for example Salamone (2023) [50]. Furthermore, there is no clear equivalence to torsion in 2D curvature, for the geometries that we are interested in. Because of this, we are not interested in systems with torsion in this thesis, and will therefore let $\tau(s) = 0$ in the following sections. The Frenet-Serret equations thus reduce to

$$\partial_s \hat{\boldsymbol{\mathcal{T}}} = \kappa(s) \hat{\boldsymbol{\mathcal{N}}}, \tag{4.36}$$

$$\partial_s \hat{\boldsymbol{\mathcal{N}}} = -\kappa(s) \hat{\boldsymbol{\mathcal{T}}}, \tag{4.37}$$

$$\partial_s \hat{\boldsymbol{\mathcal{B}}} = 0. \tag{4.38}$$

We are now ready to construct the the 3D coordinate vector, as

$$\boldsymbol{R}(s, b, n) = \boldsymbol{\gamma}(s) + b\hat{\boldsymbol{\mathcal{B}}}(s) + n\hat{\boldsymbol{\mathcal{N}}}(s). \tag{4.39}$$

Using the Frenet-Serret equations, the three covariant basis vectors in our coordinate system are thus

$$\boldsymbol{e}_s = \eta(s, n)\hat{\boldsymbol{\mathcal{T}}}(s), \quad \boldsymbol{e}_b = \hat{\boldsymbol{\mathcal{B}}}, \quad \boldsymbol{e}_n = \hat{\boldsymbol{\mathcal{N}}}. \tag{4.40}$$

Here, we have defined $\eta(s, n) = 1 - n\kappa(s)$. We note that the basis vectors in (4.40) are orthogonal, but not normalized. The metric tensor is thus

$$g_{ij} = \begin{pmatrix} \eta(s,n)^2 & 0 & 0 \\ 0 & 1 & 0 \\ 0 & 0 & 1 \end{pmatrix}, \tag{4.41}$$

using the definition from (4.11). We now recognise the choice of basis vectors in (4.31)-(4.33) as the physical vectors, defined in (4.15), thus illuminating how physical vectors can be more intuitive to work with in certain systems.

We now need to determine the Christoffel symbols for this metric. The contravariant basis vectors are found to be

$$\boldsymbol{e}^s = \eta(s,n)^{-1}\hat{\boldsymbol{\mathcal{T}}}(s), \quad \boldsymbol{e}^b = \hat{\boldsymbol{\mathcal{B}}}, \quad \boldsymbol{e}^n = \hat{\boldsymbol{\mathcal{N}}}. \tag{4.42}$$

Using the definition in (4.20), we see that $\Gamma^k_{ij} = \partial_i \boldsymbol{e}_j \cdot \boldsymbol{e}^k$. Taking the derivative of the covariant basis vectors with respect to s, n and b, and applying the Frenet-Serret equations, we find the Christoffel symbols to be [67]

$$\Gamma^s_{ss} = -\eta(s,n)^{-1} n \partial_s \kappa(s), \tag{4.43}$$
$$\Gamma^n_{ss} = \eta(s,n)\kappa(s), \tag{4.44}$$
$$\Gamma^s_{sn} = \Gamma^s_{ns} = -\eta(s,n)^{-1}\kappa(s). \tag{4.45}$$

The rest of the Christoffel symbols are zero.

4.2.1 Dimensionality in Christoffel symbols

This far, we have not yet made any assumptions about the dimensionality of the system. We have only made assumptions about the dimensionality of the curvature, as well as removing torsion. That is, this coordinate system may very well describe the bulk of some 3D material that is curved along some 1D curvature. This description implies that the coordinate system has a finite extension in the normal and binormal direction. We may thus restrict the dimensionality of our system by fixing the value of b or n, along with removing the corresponding derivatives. For example, letting $n \to 0$ corresponds to a thin film material, curved in one direction. If we also let $b \to 0$, we are left with a wire-like structure.

At the end of section 4.1.1 we mentioned that the number of Christoffel symbols depend on the dimensionality of the system. This point is subtler than it seems at first glance. Since Christoffel symbols typically appear in equations as implicit sums over indices, one has to be careful not to sum over the wrong number of indices. For example, let us say we want to find the derivative of a 3D vector that is confined to a 2D surface. A way to visualize this could be to consider a 3D exchange field vector, on a thin film surface. The exchange field cannot move off the surface of course, but it is allowed to point out of the plane. The coordinate covariant derivative in the i^{th} direction of the j^{th} covariant component of the vector is thus

$$\mathcal{D}_i h_j = \partial_i h_j - \Gamma^k_{ij} A_k. \tag{4.46}$$

Here, the values of k and j should be taken over all 3 directions, while i should only take on values corresponding to the 2 directions determined by the 2D surface. Thus, we may potentially have $2 \times 3 \times 3 = 18$ Christoffel symbols in the coordinate covariant derivative although our system is technically 2 dimensional. This is because we have a vector on the surface that is allowed to point in all 3 spatial directions. When summing over multiple indices it is therefore easy to lose track of what coordinates each index should take on. Because of this, we will make sure to explicitly state what coordinates to sum over, whenever deemed necessary.

4.3 Curvature induced strain

At the end of section 3.1 we mentioned that geometric curvature can give rise to SO coupling due to strain. To describe this mechanic more in-depth, we have to first find a way to define strain. There are multiple ways of defining strain, and in this thesis we will use the definition of *engineering strain*, also known as *Cauchy strain*, for 1D. This strain is given by [67]

$$\epsilon = \frac{\Delta L}{L_0} = \frac{L(n) - L_0}{L_0}, \tag{4.47}$$

that is, the difference between the strained length $L(n)$ and the original length L_0, divided by the original length. The strained length thus depends on the distance n from the center of the wire. From this definition we see that the strain is positive where the wire is elongated, and negative when it is compressed. Let us now assume that we are dealing with a constant curvature. A constant curvature means that the wire is forming a circle with radius r_0, such that the curvature is given by $\kappa = \frac{1}{r_0}$. Here r_0 denotes the radius from the center of the circle, to the center of the wire, as shown in figure 4.3. The strain is thus given by

$$\epsilon = \frac{(r_0 + n)\theta - r_0\theta}{r_0\theta} = n\kappa(s), \tag{4.48}$$

where we argue that the s-dependence in $\kappa(s)$ comes from the fact that we can approximate any arbitrary curve by piecewise circles. Thus the expression for strain in (4.48) should also hold for an arbitrary curve, with an s-dependence. This result shows that the strain is proportional to the curvature, as expected. This strain induces an electric potential, due to a shift in band energies [88], which is given by

$$\mathcal{V} = \lambda n \kappa \tag{4.49}$$

for small strains [89]. Here, λ is a constant, denoting the energy scale. We then find the resulting electric field by taking the gradient of $\mathcal{V}$

$$e\boldsymbol{E} = -\nabla\mathcal{V} = -\boldsymbol{e}^i\partial_i\mathcal{V} = \frac{\lambda n}{\eta(s,n)}\partial_s\kappa(s)\hat{\boldsymbol{\mathcal{T}}} + \lambda\kappa(s)\hat{\boldsymbol{\mathcal{N}}}. \tag{4.50}$$

This expression can be averaged over the normal direction component, n, to give us

$$e\langle\boldsymbol{E}\rangle_n = -\lambda\kappa(s)\hat{\boldsymbol{\mathcal{N}}}. \tag{4.51}$$

Thus, the curvature has given rise to an electric field pointing in the normal direction, that is proportional to the curvature. This electric field should, following the discussion in section 3.1, give rise to an SO field of the following form [67]

$$\underline{\boldsymbol{A}}_n = \alpha_n(\hat{\boldsymbol{\mathcal{N}}} \times \underline{\boldsymbol{\sigma}}), \tag{4.52}$$

where $\alpha_n = -\frac{g\lambda\kappa(s)}{4m}$ denotes the curvature-induced SO coupling constant. It is important to note that this SO field varies in space, due to both the s-dependent curvature and the Christoffel symbols that appear when taking its derivative. The fact that the SO field is proportional to the geometric curvature is interesting, as this facilitates the possibility of creating materials with a tunable SO coupling. That is, through curvature we may dynamically tune the SO coupling strength, allowing us to dynamically convert between systems with qualitatively different behaviours.

4.4 Curved nanowire

We now consider a specific system in order to investigate how curvature affects the transport of superconductive correlations in 1D. We will consider a ferromagnetic nanowire under constant curvature, in contact with a superconducting reservoir in both ends. This type of curvature corresponds to a section of a circle, with radius r_0. The system is sketched in figure 4.3. For such a system we apply curvilinear coordinates, where the curvature can be shown to be $\kappa = \frac{1}{r_0}$. In order to simulate the dimensionality of the nanowire, we let $n \to 0$ and $b \to 0$. Thus the derivatives in the normal- and binormal- direction both vanish, and the number of Christoffel symbols produced by the Laplacian reduce to 1, according to the discussion in section 4.2.1. Since we are interested in studying solely the effects of curvature on the system, we will ignore the effects of any SO coupling, also from strain, by setting $\hat{\boldsymbol{A}} = 0$.

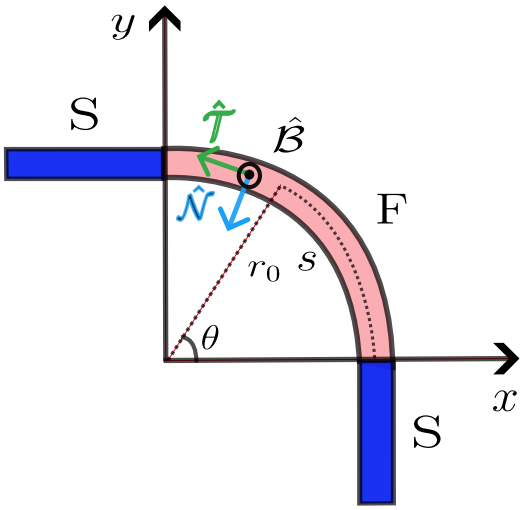

Figure 4.3: A curved ferromagnetic nanowire with superconductors in both ends.

First, let us find an appropriate expression for $\hat{\boldsymbol{\mathcal{T}}}(s)$, $\hat{\boldsymbol{\mathcal{N}}}(s)$, and $\hat{\boldsymbol{\mathcal{B}}}(s)$. To do this, let us define our 3D coordinate vector $\boldsymbol{R}$ in a cylindrical coordinate system, since this is the best choice to describe circles in 3D. The coordinate vector is thus given by

$$\boldsymbol{R}(\theta, r, z) = r\cos(\theta)\hat{\boldsymbol{x}} + r\sin(\theta)\hat{\boldsymbol{y}} + z\hat{\boldsymbol{z}}. \tag{4.53}$$

Since we are interested in describing a curve along a circle with radius r_0, let us define the normal component n such that we are confined to the circle when $n \to 0$. This gives us $r = r_0 - n$, which means that the normal vector will point inwards, to the center of the circle. Furthermore, we recall that $\boldsymbol{R}$ should be parameterized in terms of the arc-length s. For a circle with radius r_0, $s = \theta r_0$. Finally, we realize that the binormal component is simply given by $b = z$. Inserting these reparameterizations into (4.53), we get

$$\boldsymbol{R}(s, n, b) = (r_0 - n)\cos(s/r_0)\hat{\boldsymbol{x}} + (r_0 - n)\sin(s/r_0)\hat{\boldsymbol{y}} + b\hat{\boldsymbol{z}}. \tag{4.54}$$

The covariant basis vectors are thus

$$\boldsymbol{e}_s = \eta(s,n)(-\sin(s\kappa)\hat{\boldsymbol{x}} + \cos(s\kappa)\hat{\boldsymbol{y}}), \tag{4.55}$$
$$\boldsymbol{e}_n = -\cos(s\kappa)\hat{\boldsymbol{x}} - \sin(s\kappa)\hat{\boldsymbol{y}}, \tag{4.56}$$
$$\boldsymbol{e}_b = \hat{\boldsymbol{z}}, \tag{4.57}$$

where we have identified the curvature as $\kappa = r_0^{-1}$. Using (4.40) and taking the limit $n \to 0$, now gives us

$$\hat{\boldsymbol{\mathcal{T}}} = -\sin(s\kappa)\hat{\boldsymbol{x}} + \cos(s\kappa)\hat{\boldsymbol{y}}, \tag{4.58}$$
$$\hat{\boldsymbol{\mathcal{N}}} = -\cos(s\kappa)\hat{\boldsymbol{x}} - \sin(s\kappa)\hat{\boldsymbol{y}}, \tag{4.59}$$
$$\hat{\boldsymbol{\mathcal{B}}} = \hat{\boldsymbol{z}}. \tag{4.60}$$

The Usadel equation for a 1D system, with $\hat{\boldsymbol{\mathcal{T}}}$ as the direction of propagation can be found from (4.26) by restricting the indices involved in partial derivatives to s. We get

$$iD_F g^{ss}\left(\partial_s(\hat{g}^R\partial_s\hat{g}^R) - \Gamma^s_{ss}\hat{g}^R\partial_s\hat{g}^R\right) = [E\hat{\tau}_z + \hat{\Delta} + g^{ij}h_i\hat{\sigma}_j, \hat{g}^R]. \tag{4.61}$$

In the limit $n \to 0$, we have $g^{ss} = \eta(s,n)^{-2} = 1$ and $\Gamma^s_{ss} = 0$. Equation (4.61) thus simplifies to

$$iD_F\partial_s(\hat{g}^R\partial_s\hat{g}^R) = [E\hat{\tau}_z + \hat{\Delta} + h_i\hat{\sigma}_i, \hat{g}^R], \tag{4.62}$$

where the Pauli matrices are given by $\hat{\sigma}_i = \mathrm{diag}(\underline{\sigma}_i, \underline{\sigma}_i^*) = \mathrm{diag}(\underline{\boldsymbol{\sigma}}\cdot\boldsymbol{e}_i, \underline{\boldsymbol{\sigma}}^*\cdot\boldsymbol{e}_i)$ in our coordinate system. This gives us

$$\underline{\sigma}_s = \begin{pmatrix} 0 & -ie^{-is\kappa} \\ ie^{is\kappa} & 0 \end{pmatrix}, \quad \underline{\sigma}_n = \begin{pmatrix} 0 & -e^{-is\kappa} \\ -e^{is\kappa} & 0 \end{pmatrix}, \quad \underline{\sigma}_b = \begin{pmatrix} 1 & 0 \\ 0 & -1 \end{pmatrix}. \tag{4.63}$$

Therefore, the only way in which curvature affects (4.62) is through the ferromagnetic self-energy. As we will see, this effect alone is enough to influence the transport of superconductive correlations in our system substantially. The Pauli matrices in (4.63) correspond to a rotating exchange field along the $\hat{\boldsymbol{\mathcal{T}}}$- and $\hat{\boldsymbol{\mathcal{N}}}$- direction. We therefore expect spin-rotation to occur whenever there is a finite exchange field in the tangential or normal direction. To see this, we once again turn to spin-parameterization in the weak proximity limit. Starting now from (3.24) and (3.25), we let $\alpha = 0$, take our direction of propagation to be $\hat{\boldsymbol{\mathcal{T}}}$ and write the equations in tensor form. For equation (3.24), this gives us

$$D_F g^{ss}\mathcal{D}_s\mathcal{D}_s(\boldsymbol{e}^i d_i) = -2i(E\boldsymbol{d} + f_0\boldsymbol{h}). \tag{4.64}$$

The left-hand side of (4.64) can be evaluated by applying the product rule for differentiation several times. We get

$$\begin{aligned} D_F\mathcal{D}_s\mathcal{D}_s(d_i\boldsymbol{e}^i) &= D_F\partial_s(\partial_s(d_i\boldsymbol{e}^i)) \\ &= D_F((\partial_s^2 d_i)\boldsymbol{e}^i + 2(\partial_s d_i)(\partial_s\boldsymbol{e}^i) + d_i\partial_s(\partial_s\boldsymbol{e}^i)) \\ &= D_F((\partial_s^2 d_i)\boldsymbol{e}^i - 2(\partial_s d_i)\Gamma^i_{sk}\boldsymbol{e}^k - d_i((\partial_s\Gamma^i_{sk})\boldsymbol{e}^k - \Gamma^i_{sk}\Gamma^k_{sl}\boldsymbol{e}^l)) \\ &= D_F(\partial_s^2 d_i - 2(\partial_s d_k)\Gamma^k_{si} - d_k(\partial_s\Gamma^k_{si} - \Gamma^k_{sl}\Gamma^l_{si}))\boldsymbol{e}^i. \end{aligned} \tag{4.65}$$

In the first step, we used the fact that $\Gamma^s_{ss} = 0$, such that the coordinate covariant derivatives reduce to normal derivatives. In the last step, we used the fact that we can relabel summed indices as we like, in order to pull $\boldsymbol{e}^i$ outside the parentheses. Taking the inner product with $\boldsymbol{e}_\alpha$ on both sides in (4.64) gives

$$D_F(\partial_s^2 d_\alpha - 2(\partial_s d_k)\Gamma^k_{s\alpha} - d_k(\partial_s \Gamma^k_{s\alpha} - \Gamma^k_{sl}\Gamma^l_{s\alpha})) = -2i(Ed_\alpha + f_0 h_\alpha). \tag{4.66}$$

Letting $\alpha = s$, n, b now gives us 3 different equations, each for one component of the d-vector. Writing each of these equations out, and inserting the Christoffel symbols in (4.43)-(4.45) gives us [34]

$$D_F(\partial_s^2 d_s - 2\kappa\partial_s d_n - \kappa^2 d_s) = -2i(Ed_s + f_0 h_s), \tag{4.67}$$
$$D_F(\partial_s^2 d_n + 2\kappa\partial_s d_s - \kappa^2 d_n) = -2i(Ed_n + f_0 h_n), \tag{4.68}$$
$$D_F\partial_s^2 d_b = -2i(Ed_b + f_0 h_b), \tag{4.69}$$
$$D_F\partial_s^2 f_0 = -2i(Ef_0 + \boldsymbol{h}\cdot\boldsymbol{d}), \tag{4.70}$$

where we have added the equation for the singlet component as well, in (4.70). We see that these equations describe the possibility for spin-rotation through spin-precession, as discussed in section 3.2.1. In order to analyze these equations further, we need to choose a direction for the exchange field. As discussed by Sheka (2015) [83], the exchange field will naturally follow the tangential direction for a large class of materials. We thus have $\boldsymbol{h} = h\hat{\boldsymbol{T}}$, which means that $d_{srt} = d_s$. Equation (4.67) then tells us that we will generate d_n components through precession. We have thus shown that the rotating exchange field, introduced through (4.63), will cause spin-rotation in the 1D nanowire, in the weak proximity limit.

4.4.1 Numerical results

In this section, we investigate the curved nanowire further, through numerical calculations. Assuming that the exchange field will follow the tangential direction, we let $\boldsymbol{h} = |\Delta|[-\sin(s\kappa), \cos(s\kappa), 0]$. In figure 4.4(a) we have plotted the density of states for an SF nanowire system, under constant curvature, for curvatures $\kappa L = \pi/4$ and $\kappa L = 0$, with length $L = 2\xi$. This plot shows a small raise at zero energy, indicating the presence of triplets. To confirm this, we plot the evolution of the absolute value of the LRT-, SRT- and singlet- component into the ferromagnet, in figure 4.4(b). This plot shows that the curvature induces a d-vector component in the normal direction, corresponding to the LRT component. Furthermore, we see that the absolute value of d_n initially increases from $s = 0$, indicating that the spin-rotation happens spatially as we move along the curvature.

In figure 4.6 we have plotted $|d_N|$, $|d_T|$ and $|f_0|$ as a function of both curvature and the arc length, in order to study what curvatures yield the most triplet components. Here, we have set $L = 5\xi$ in order to study the long-range effect of the LRTs. In figure 4.6(a) we see that a larger curvature yields more LRTs near the interface, but that this value decreases rapidly, in an oscillatory manner. Looking at figure 4.6(b), the LRTs seem to oscillate with a phase difference of approximately π with respect to the SRTs, and the frequency of these oscillations increases with higher curvature. This makes sense looking at equations (4.67)-(4.68), as we expect the spin rotation effect to get stronger with higher curvature. Interestingly, only a small curvature is needed to generate LRTs.

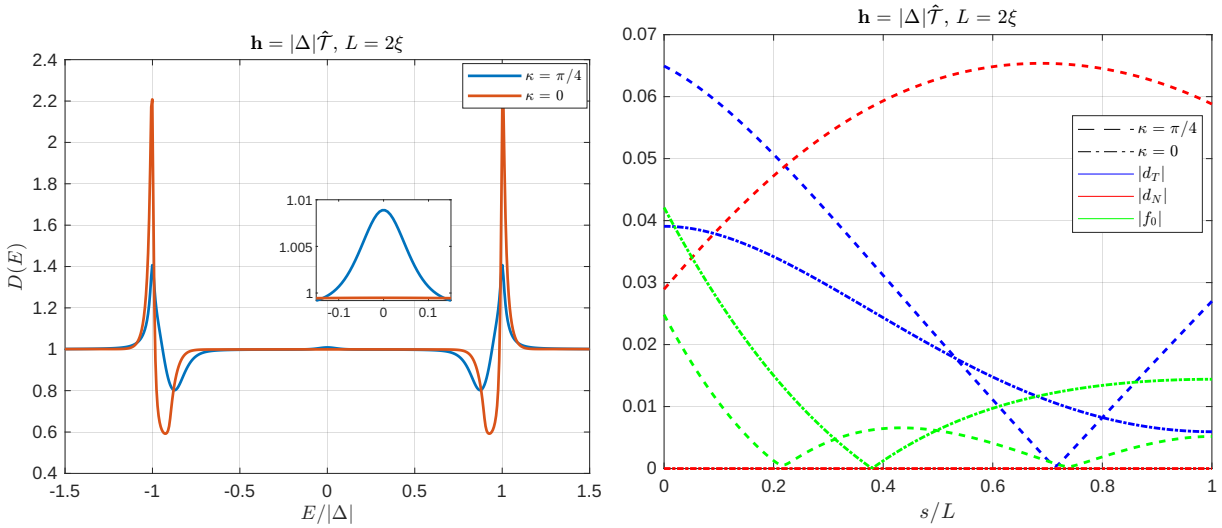

(a) (b)

Figure 4.4: (a) Density of states as a function of the energy $E/|\Delta|$ in an SF proximity system, with the superconductor at $L = 0$, to the left of the ferromagnet, for $\kappa = \pi/4$ and $\kappa = 0$ with $L = 2\xi$, $\boldsymbol{h} = |\Delta|\hat{\boldsymbol{\mathcal{T}}}$ and $\zeta = 3$. Zoom in on zero energy to see a raise in the density of states for $\kappa = \pi/4$. (b) The absolute value of d_N, d_T and f_0 as a function of the arc length s/L for the same systems as (a).

Furthermore, the LRTs generated at this curvature seem to have a stronger long-range effect than those at higher curvatures. This demonstrates the friction-like behaviour of curvature, as we see in (4.67)-(4.68). That is, curvature acts as friction in these systems, costing the superconducting correlations more energy the higher the curvature is. Hence, we see that although the LRT generation is stronger for higher curvature, so is the energy dissipation. Thus, a finite, but smaller curvature is favoured for generating LRTs over longer distances.

Another interesting system to consider under constant curvature is a Josephson junction-like SFS system. In figure 4.5 we have plotted the absolute value of the charge current density as a function of the dimensionless curvature κL, for $L = 2\xi$ and $L = 4\xi$. This plot demonstrates a curvature induced 0-π transition, indicating that we can reverse the current direction in an SFS junction by varying curvature alone. For further discussion on this phenomena, see Salamone et al. (2021) [54].

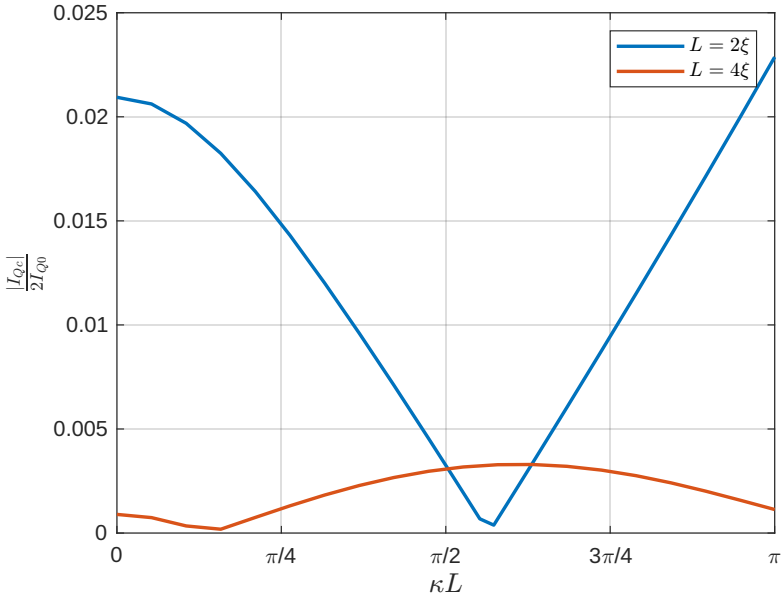

Figure 4.5: Curvature induced 0-π transition in an SFS system for lengths $L = 2\xi$ and $L = 4\xi$. The exchange field is $\boldsymbol{h} = |\Delta|\hat{\boldsymbol{\mathcal{T}}}$ and the phase difference is $\phi = \pi/2$.

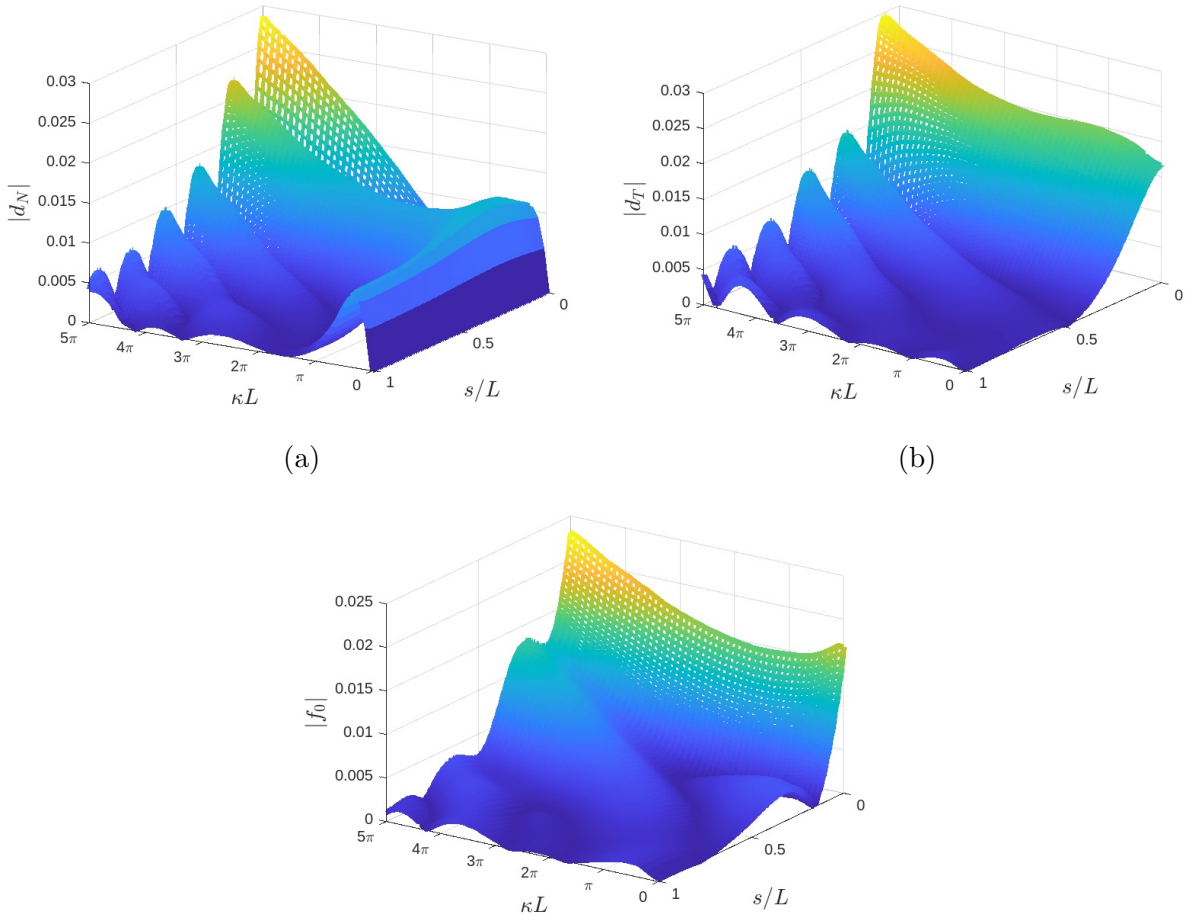

Figure 4.6: The absolute value of (a) d_N, (b) d_T and (c) f_0 as a function of curvature κL and arc length s/L at energy $E = 0$, for $L = 5\xi$, $\boldsymbol{h} = |\Delta|\hat{\boldsymbol{\mathcal{T}}}$ and $\zeta = 3$.

5 Differential geometry of surfaces

From this section on, we turn our attention to 2D systems. We will develop a formalism that is able to describe the transport of superconducting correlations on two dimensional curved surfaces. In 1D we used the curvilinear coordinate system. However, this is insufficient in higher dimensions. The main reason for this is that curvilinear coordinates are only able to describe curvature along a single dimension. If we want to describe two dimensional curvatures, such as spherical surfaces, we therefore need a different formalism. This chapter is inspired by the book *Elemental Differential Geometry* by Andrew Pressley [87].

5.1 The fundamental forms

The properties of 2D surfaces can be described effectively by the two fundamental forms. The first fundamental form describes the geometry of the surface, capturing the notions of distances, angles and areas on the surface. The second fundamental form is related to how the normal vector changes along the surface, and thus captures the effects of curvature on the surface.

We begin by parametrizing the 3-dimensional space as

$$\boldsymbol{R}(u,v,n) = \boldsymbol{\mathcal{S}}(u,v) + n\hat{\boldsymbol{\mathcal{N}}}(u,v), \tag{5.1}$$

where $\boldsymbol{\mathcal{S}}(u,v)$ corresponds to the parametrization of the surface and $\hat{\boldsymbol{\mathcal{N}}}$ is defined as the normalized normal vector to the tangential plane. To define the tangential plane we define a tangent vector to a curve on the surface, through some point $\boldsymbol{p}$. A general curve on the surface $\boldsymbol{\mathcal{S}}(u,v)$ is found by parameterizing the variables u, v accordingly. Hence, for a curve $\boldsymbol{\gamma}(t) = \boldsymbol{\mathcal{S}}(u(t),v(t))$ we find that the tangent vector to this curve at some point $\boldsymbol{p}$ on the surface is given by

$$\partial_t \boldsymbol{\gamma}(t)|_{\boldsymbol{p}} = \partial_t u \boldsymbol{\mathcal{S}}_u|_{\boldsymbol{p}} + \partial_t v \boldsymbol{\mathcal{S}}_v|_{\boldsymbol{p}}, \tag{5.2}$$

where we have denoted partial differentiation with a subscript, $\frac{\partial f}{\partial x} = \partial_x f = f_x$ and chosen t as our variable for the parameterization. Since $\boldsymbol{\gamma}(t)$ is an arbitrary curve through $\boldsymbol{p}$ in $\boldsymbol{\mathcal{S}}(u(t),v(t))$ we can choose infinitely many unique curves through $\boldsymbol{p}$ with infinitely many unique tangential vectors. By inspection we see that all these tangential vectors form a plane spanned by the basis vectors $\boldsymbol{\mathcal{S}}_u$ and $\boldsymbol{\mathcal{S}}_v$, and we define this plane as the tangential plane at the point $\boldsymbol{p}$ of the surface $\boldsymbol{\mathcal{S}}(u(t),v(t))$. It is therefore natural to use $\boldsymbol{\mathcal{S}}_u$ and $\boldsymbol{\mathcal{S}}_v$ as basis vectors for the tangential plane.

We are, however, in general interested in basis vectors that describe the entire 3-dimensional space surrounding the 2-dimensional surface. We therefore define the basis vectors as usual by $\boldsymbol{e}_i = \partial_i \boldsymbol{R}(u,v,n)$. This gives us

$$\begin{aligned}
\boldsymbol{e}_u &= \partial_u \boldsymbol{R}(u,v,n) = \boldsymbol{\mathcal{S}}_u(u,v) + n\hat{\boldsymbol{\mathcal{N}}}_u(u,v),\\
\boldsymbol{e}_v &= \partial_v \boldsymbol{R}(u,v,n) = \boldsymbol{\mathcal{S}}_v(u,v) + n\hat{\boldsymbol{\mathcal{N}}}_v(u,v),\\
\boldsymbol{e}_n &= \partial_n \boldsymbol{R}(u,v,n) = \hat{\boldsymbol{\mathcal{N}}}(u,v).
\end{aligned} \tag{5.3}$$

Here, the subscript on the basis vectors $\boldsymbol{e}_i$ is used to denote covariant vectors, as per usual, and not as a partial derivative. In most literature on differential geometry of $2D$

surfaces, all motion is assumed to be confined to the surface. This means that the basis vectors are defined in the limit $n \to 0$, and the metric and Christoffel symbols are derived in this limit. This simplifies the calculations significantly. However, in this thesis we wish to develop a formalism that can also describe motion perpendicularly to the surface, such as the motion across stacked thin films. We therefore consider n to be a finite variable in our calculations.

5.1.1 The first fundamental form

One of the first things one might be interested in calculating when considering a 2D surface is the arc lengths of the curves on this surface. While this may seem like an arbitrary place to start analyzing surfaces, we shall see that in our attempt to formulate an expression for the arc length s, we will discover and define quantities that will be essential to the rest of our theory. We thus begin by considering the expression for the arc length s, of an arbitrary curve $\boldsymbol{\gamma}(t)$ given by

$$s = \int ||\partial_t \boldsymbol{\gamma}(t)|| dt. \tag{5.4}$$

From this expression we see that we require the inner product of $\dot{\boldsymbol{\gamma}}$ with itself to find s. Using equation (5.2) we see that

$$(\partial_t \boldsymbol{\gamma}(t)) \cdot (\partial_t \boldsymbol{\gamma}(t)) = (\partial_t u)^2 ||\boldsymbol{\mathcal{S}}_u||^2 + 2(\partial_t u)(\partial_t v)\boldsymbol{\mathcal{S}}_u \cdot \boldsymbol{\mathcal{S}}_v + (\partial_t v)^2 ||\boldsymbol{\mathcal{S}}_v||^2, \tag{5.5}$$

which is often written in the form

$$d\boldsymbol{\gamma}(t) \cdot d\boldsymbol{\gamma}(t) = Edu^2 + 2Fdudv + Gdv^2 \tag{5.6}$$

in the literature, after defining the following parameters

$$E = ||\boldsymbol{\mathcal{S}}_u||^2, \quad F = \boldsymbol{\mathcal{S}}_u \cdot \boldsymbol{\mathcal{S}}_v, \quad G = ||\boldsymbol{\mathcal{S}}_v||^2. \tag{5.7}$$

Equations (5.6) and (5.7) are referred to as the first fundamental form and describes the length of paths on the surface. From this definition, we see that E, F and G together form the *two dimensional metric*,

$$\mathcal{G} = \begin{pmatrix} E & F \\ F & G \end{pmatrix}. \tag{5.8}$$

By two dimensional metric, we mean a metric in which the third dimension has been removed.

5.1.2 The second fundamental form

The second fundamental form arises from defining the curvature of the surface. One way to define curvature is to investigate how much the normal vector changes when moving an infinitesimal length ds along the surface. For a surface without any curvature, such as the xy-plane, we see that the normal vector along the z-direction is constant. For a very curved surface however, one will observe that the normal vector changes very rapidly while moving along this surface. This tells us that the more the normal vector $\hat{\boldsymbol{\mathcal{N}}}$ changes along some path on the surface, the more the surface is curving along that path. We

see that this way of defining curvature is in conjunction with the curvilinear formalism, looking at the second Frenet-Serret equation in (4.35),

$$\partial_s \hat{\boldsymbol{\mathcal{N}}} = -\kappa(s)\hat{\boldsymbol{\mathcal{T}}} + \tau(s)\hat{\boldsymbol{\mathcal{B}}}. \tag{5.9}$$

Looking at equation (5.9) we see that in order to extract information about the curvature, we should project $\partial_s \hat{\boldsymbol{\mathcal{N}}}$ along the basis vectors for the tangential plane. This leads us to defining the following parameters

$$\hat{\boldsymbol{\mathcal{N}}}_u \cdot \boldsymbol{\mathcal{S}}_u = -L, \quad \hat{\boldsymbol{\mathcal{N}}}_u \cdot \boldsymbol{\mathcal{S}}_v = \hat{\boldsymbol{\mathcal{N}}}_v \cdot \boldsymbol{\mathcal{S}}_u = -M, \quad \hat{\boldsymbol{\mathcal{N}}}_v \cdot \boldsymbol{\mathcal{S}}_v = -N. \tag{5.10}$$

The parameters L, M and N describe the second fundamental form. The negative signs in equation (5.10) are due to convention, and the fact that the second fundamental form is more often expressed in the form

$$\hat{\boldsymbol{\mathcal{N}}} \cdot \boldsymbol{\mathcal{S}}_{uu} = L, \quad \hat{\boldsymbol{\mathcal{N}}} \cdot \boldsymbol{\mathcal{S}}_{uv} = \hat{\boldsymbol{\mathcal{N}}} \cdot \boldsymbol{\mathcal{S}}_{vu} = M, \quad \hat{\boldsymbol{\mathcal{N}}} \cdot \boldsymbol{\mathcal{S}}_{vv} = N. \tag{5.11}$$

The connection between equations (5.10) and (5.11) can be seen by differentiating both of the equations $\hat{\boldsymbol{\mathcal{N}}} \cdot \boldsymbol{\mathcal{S}}_u = 0$ and $\hat{\boldsymbol{\mathcal{N}}} \cdot \boldsymbol{\mathcal{S}}_v = 0$ with respect to u and v. Doing this, we also establish the equality $\hat{\boldsymbol{\mathcal{N}}}_u \cdot \boldsymbol{\mathcal{S}}_v = \hat{\boldsymbol{\mathcal{N}}}_v \cdot \boldsymbol{\mathcal{S}}_u$ used in equation (5.10). The second fundamental form is often expressed in the form

$$\hat{\boldsymbol{\mathcal{N}}} \cdot d^2\boldsymbol{\mathcal{S}} = Ldu^2 + 2Mdudv + Ndv^2 \tag{5.12}$$

similarly to the first fundamental form.

5.2 The metric

We are now equipped to start our derivation of the metric tensor for our coordinate system. To start our calculations we recall that we can obtain the components of the metric tensor g_{ij} by considering the norm of the differential coordinate displacement, given by

$$(dR)^2 = g_{ij}dx^i dx^j. \tag{5.13}$$

Using equation (5.3) gives

$$d\boldsymbol{R} = (\boldsymbol{\mathcal{S}}_u + n\hat{\boldsymbol{\mathcal{N}}}_u)du + (\boldsymbol{\mathcal{S}}_v + n\hat{\boldsymbol{\mathcal{N}}}_v)dv + \hat{\boldsymbol{\mathcal{N}}}dn. \tag{5.14}$$

Squaring equation (5.14) we find the following expression for the metric g_{ij},

$$\begin{pmatrix} E - 2nL + n^2\hat{\boldsymbol{\mathcal{N}}}_u \cdot \hat{\boldsymbol{\mathcal{N}}}_u & F - 2nM + n^2\hat{\boldsymbol{\mathcal{N}}}_v \cdot \hat{\boldsymbol{\mathcal{N}}}_u & n\hat{\boldsymbol{\mathcal{N}}}_u \cdot \hat{\boldsymbol{\mathcal{N}}} \\ F - 2nM + n^2\hat{\boldsymbol{\mathcal{N}}}_v \cdot \hat{\boldsymbol{\mathcal{N}}}_u & G - 2nN + n^2\hat{\boldsymbol{\mathcal{N}}}_v \cdot \hat{\boldsymbol{\mathcal{N}}}_v & n\hat{\boldsymbol{\mathcal{N}}}_v \cdot \hat{\boldsymbol{\mathcal{N}}} \\ n\hat{\boldsymbol{\mathcal{N}}}_u \cdot \hat{\boldsymbol{\mathcal{N}}} & n\hat{\boldsymbol{\mathcal{N}}}_v \cdot \hat{\boldsymbol{\mathcal{N}}} & 1 \end{pmatrix} \tag{5.15}$$

where we have used both the first and second fundamental forms. In order to evaluate the inner products involving $\hat{\boldsymbol{\mathcal{N}}}$ and its derivatives we first note that any change in $\hat{\boldsymbol{\mathcal{N}}}$ under an infinitesimal movement ds along the surface must be confined to the tangential plane at that point. This means that we can write the quantities $\hat{\boldsymbol{\mathcal{N}}}_{u,v}$ as a linear combination of the basis vectors $\boldsymbol{\mathcal{S}}_{u,v}$. We thus write

$$\begin{aligned} \hat{\boldsymbol{\mathcal{N}}}_u &= a\boldsymbol{\mathcal{S}}_u + b\boldsymbol{\mathcal{S}}_v, \\ \hat{\boldsymbol{\mathcal{N}}}_v &= c\boldsymbol{\mathcal{S}}_u + d\boldsymbol{\mathcal{S}}_v, \end{aligned} \tag{5.16}$$

where a, b, c and d are coefficients to be decided. Taking the inner product of each equation with respect to both $\boldsymbol{\mathcal{S}}_u$ and $\boldsymbol{\mathcal{S}}_v$ we get the following set of equations

$$\begin{aligned} L &= -aE - bF, \quad M = -aF - bG, \\ M &= -cE - dF, \quad N = -cF - dG. \end{aligned} \tag{5.17}$$

We now define the matrices

$$\mathcal{F} = \begin{pmatrix} L & M \\ M & N \end{pmatrix}, \quad \mathcal{W} = -\begin{pmatrix} a & b \\ c & d \end{pmatrix}, \tag{5.18}$$

to make our notation tidier. We now see that we can write $\mathcal{F} = \mathcal{W}\mathcal{G}$ giving us

$$\mathcal{W} = \mathcal{G}^{-1}\mathcal{F} = \frac{1}{|\mathcal{G}|}\begin{pmatrix} LG - FM & MG - FN \\ ME - FL & NE - FM \end{pmatrix}, \tag{5.19}$$

where $|\mathcal{G}| = EG - F^2$ and we have used that $\mathcal{W}$ is self-adjoint. We call $\mathcal{W}$ the *Weintgarten matrix* or the *shape operator* [37], describing differentiation of the normal vector. We recall from section 5.1.2 that the derivative of the normal vector at any point is closely related to the curvature in that point. As we shall see later, the Weintgarten matrix is directly related to how we define curvatures within this formalism.

The metric in (5.15) can now be written as

$$g = \begin{pmatrix} \eta_{11} & \eta_{12} & 0 \\ \eta_{21} & \eta_{22} & 0 \\ 0 & 0 & 1 \end{pmatrix}, \tag{5.20}$$

where we have defined

$$\eta_{11} = E - 2nL + n^2(\mathcal{W}_{11}L + \mathcal{W}_{12}M), \tag{5.21}$$
$$\eta_{12} = \eta_{21} = F - 2nM + n^2(\mathcal{W}_{11}M + \mathcal{W}_{12}N), \tag{5.22}$$
$$\eta_{22} = G - 2nN + n^2(\mathcal{W}_{21}M + \mathcal{W}_{22}N). \tag{5.23}$$

We note that we can write $\eta = \mathcal{G} - 2n\mathcal{F} + n^2\mathcal{W}\mathcal{F}$ using the definitions in (5.18). In the limit $n \to 0$ η_{ij} reduces to $\mathcal{G}_{ij}$, as expected.

5.3 Curvatures in the 2D plane

The curvature of the system along some path is, as previously discussed, related to how the normal vector $\hat{\boldsymbol{\mathcal{N}}}$ changes along that path. This tells us that information about the curvature should be embedded in the Weintgarten matrix, $\mathcal{W}$. We define the *mean curvature* of the system, H, from the trace of $\mathcal{W}$ and the *Gaussian curvature* of the system, K, as the determinant of $\mathcal{W}$. We thus get

$$H = \frac{GL + EN - 2FM}{2|g|}, \tag{5.24}$$
$$K = \frac{LN - M^2}{|g|}. \tag{5.25}$$

By diagonalizing $\mathcal{W}$ we may define another set of curvatures to describe the surface. We define the *principal curvatures*, κ_1 and κ_2, of the surface as the solutions to the eigenvalue equations

$$\mathcal{W}\boldsymbol{w}_1 = \kappa_1 \boldsymbol{w}_1, \quad \mathcal{W}\boldsymbol{w}_2 = \kappa_2 \boldsymbol{w}_2, \tag{5.26}$$

where the eigenvectors $\boldsymbol{w}_{1,2}$ are referred to as the *principal vectors* of the surface. We thus see that we can express H and K in terms of the principal curvatures as follows

$$H = \frac{1}{2}(\kappa_1 + \kappa_2), \quad K = \kappa_1 \kappa_2. \tag{5.27}$$

Since the principal vectors are orthogonal and span the tangential plane, along with marking the direction of the curves on the surface, they make good candidates for basis vectors. Therefore, coordinate systems that diagonalize $\mathcal{W}$ are generally preferred. As can be seen from its definition, the Gaussian curvature gives information about the dimensionality of the curvature of the surface. For example, a cylinder, which is effectively a 1-dimensional curve spanned in the binormal direction, has a Gaussian curvature of 0, while the unit sphere, which cannot be described by a single curve, has a Gaussian curvature of 1.

5.4 The Christoffel symbols

As we have done previously, we define the Christoffel symbols as $\Gamma^{\gamma}_{\alpha\beta}\boldsymbol{e}^{\gamma} = \partial_{\beta}\boldsymbol{e}_{\alpha}$, i.e. the Christoffel symbols measure how our coordinate system changes as we move along the surface. Writing out this definition, we get the following set of equations

$$\partial_u \boldsymbol{e}_u = \Gamma^1_{11}\boldsymbol{e}_u + \Gamma^2_{11}\boldsymbol{e}_v + \Gamma^3_{11}\hat{\boldsymbol{\mathcal{N}}}, \tag{5.28}$$
$$\partial_v \boldsymbol{e}_u = \Gamma^1_{12}\boldsymbol{e}_u + \Gamma^2_{12}\boldsymbol{e}_v + \Gamma^3_{12}\hat{\boldsymbol{\mathcal{N}}}, \tag{5.29}$$
$$\partial_v \boldsymbol{e}_v = \Gamma^1_{22}\boldsymbol{e}_u + \Gamma^2_{22}\boldsymbol{e}_v + \Gamma^3_{22}\hat{\boldsymbol{\mathcal{N}}}, \tag{5.30}$$
$$\hat{\boldsymbol{\mathcal{N}}}_u = \Gamma^1_{13}\boldsymbol{e}_u + \Gamma^2_{13}\boldsymbol{e}_v + \Gamma^3_{13}\hat{\boldsymbol{\mathcal{N}}}, \tag{5.31}$$
$$\hat{\boldsymbol{\mathcal{N}}}_v = \Gamma^1_{23}\boldsymbol{e}_u + \Gamma^2_{23}\boldsymbol{e}_v + \Gamma^3_{23}\hat{\boldsymbol{\mathcal{N}}}, \tag{5.32}$$
$$\hat{\boldsymbol{\mathcal{N}}}_n = \Gamma^1_{33}\boldsymbol{e}_u + \Gamma^2_{33}\boldsymbol{e}_v + \Gamma^3_{33}\hat{\boldsymbol{\mathcal{N}}}. \tag{5.33}$$

The equations (5.28)-(5.30) are commonly referred to as the *Gauss equations* in the limit where $n \to 0$. Since the normal vector should not change when moving in the normal direction, equation (5.33) is thus 0 and we get

$$\Gamma^i_{33} = 0 \quad \text{for} \quad i = 1, 2, 3. \tag{5.34}$$

The rest of the Christoffel symbols can be determined by taking the inner product of equations (5.28)-(5.32) with respect to both $\boldsymbol{\mathcal{S}}_u$, $\boldsymbol{\mathcal{S}}_v$ and $\hat{\boldsymbol{\mathcal{N}}}$. This will give us a system of equations per equation in (5.28)-(5.32) that can be solved to find the Christoffel symbols. To demonstrate how this is done we will calculate the Christoffel symbols in (5.31) using this method.

Using the definitions in (5.3), we write out (5.31) to

$$\hat{\boldsymbol{\mathcal{N}}}_u = \Gamma^1_{13}(\boldsymbol{\mathcal{S}}_u + n\hat{\boldsymbol{\mathcal{N}}}_u) + \Gamma^2_{13}(\boldsymbol{\mathcal{S}}_v + n\hat{\boldsymbol{\mathcal{N}}}_v) + \Gamma^3_{13}\hat{\boldsymbol{\mathcal{N}}}. \tag{5.35}$$

Taking the inner product between (5.35) and $\hat{\boldsymbol{\mathcal{N}}}$ we immediately see that $\Gamma^3_{13} = 0$ since $\hat{\boldsymbol{\mathcal{N}}}_{u,v}$ lies in the tangential plane. Taking the inner product with respect to $\boldsymbol{\mathcal{S}}_u$ and $\boldsymbol{\mathcal{S}}_v$ gives us the following system of equations

$$\begin{aligned} -L &= \Gamma^1_{13}(E - nL) + \Gamma^2_{13}(F - nM), \\ -M &= \Gamma^1_{13}(F - nM) + \Gamma^2_{13}(G - nN). \end{aligned} \tag{5.36}$$

The equations in (5.36) can be written more compactly in matrix notation, using the matrix definitions in (5.18), as

$$\begin{pmatrix} -L \\ -M \end{pmatrix} = (\mathcal{G} - n\mathcal{F}) \begin{pmatrix} \Gamma^1_{13} \\ \Gamma^2_{13} \end{pmatrix}. \tag{5.37}$$

We then find the Christoffel symbols by multiplying with the inverse of $(\mathcal{G} - n\mathcal{F})$, giving us

$$\begin{pmatrix} \Gamma^1_{13} \\ \Gamma^2_{13} \end{pmatrix} = \frac{1}{|\mathcal{G}|\omega(n, \kappa_1, \kappa_2)} \begin{pmatrix} G - nM & nM - F \\ nM - F & E - nL \end{pmatrix} \begin{pmatrix} -L \\ -M \end{pmatrix}, \tag{5.38}$$

where we have defined $\omega(n, \kappa_1, \kappa_2)$ such that

$$|\mathcal{G} - n\mathcal{F}| = |\mathcal{G}|\omega(n, \kappa_1, \kappa_2) = |\mathcal{G}|(1 - n\kappa_1)(1 - n\kappa_2). \tag{5.39}$$

Here κ_1 and κ_2 denote the two principal curvatures. We briefly note that ω quite resembles the prefactor $\eta(n, \kappa) = 1 - n\kappa(s)$ that frequently appears in the metric and Christoffel symbols of 1D curvilinear coordinates. We also note that the determinant of the metric can be calculated to be

$$|g| = |\mathcal{G}| \left(Kn^2 - 2Hn + 1\right)^2 = |\mathcal{G}|\omega(n, \kappa_1, \kappa_2)^2, \tag{5.40}$$

which is assuring to find, as we expect the inverse of the determinant of the metric to appear in front of all the Christoffel symbols. Multiplying out equation (5.38) gives us

$$\Gamma^1_{13} = \frac{-\mathcal{W}_{11} + nK}{\omega(n, \kappa_1, \kappa_2)} \quad \text{and} \quad \Gamma^2_{13} = \frac{-\mathcal{W}_{21}}{\omega(n, \kappa_1, \kappa_2)}, \tag{5.41}$$

which concludes the derivation of these 3 Christoffel symbols. The rest of the symbols in equations (5.28) -(5.30) and (5.32) can be found with the same technique, from which we find the following results

$$\Gamma^i_{j3} = \frac{-W_{ij} + \delta_{ij}nK}{\omega(n, \kappa_1, \kappa_2)}, \quad \Gamma^3_{i3} = 0 \quad \text{for} \quad i, j = 1, 2, \tag{5.42}$$

$$\Gamma^1_{\alpha\beta} = \frac{1}{|g|\omega}((G - nN)(\boldsymbol{\mathcal{S}}_{\alpha\beta} + n\hat{\boldsymbol{\mathcal{N}}}_{\alpha\beta}) \cdot \boldsymbol{\mathcal{S}}_u - (F - nM)(\boldsymbol{\mathcal{S}}_{\alpha\beta} + n\hat{\boldsymbol{\mathcal{N}}}_{\alpha\beta}) \cdot \boldsymbol{\mathcal{S}}_v), \tag{5.43}$$

$$\Gamma^2_{\alpha\beta} = \frac{1}{|g|\omega}((E - nL)(\boldsymbol{\mathcal{S}}_{\alpha\beta} + n\hat{\boldsymbol{\mathcal{N}}}_{\alpha\beta}) \cdot \boldsymbol{\mathcal{S}}_v - (F - nM)(\boldsymbol{\mathcal{S}}_{\alpha\beta} + n\hat{\boldsymbol{\mathcal{N}}}_{\alpha\beta}) \cdot \boldsymbol{\mathcal{S}}_u), \tag{5.44}$$

$$\Gamma^3_{\alpha\beta} = f_{\alpha\beta} - n\mathcal{W}_{\alpha\gamma} f_{\gamma\beta} \quad \text{for} \quad \alpha, \beta, \gamma = 1, 2. \tag{5.45}$$

We can express the inner products in (5.43) and (5.44) in terms of the fundamental forms as follows. Consider the inner product $\boldsymbol{\mathcal{S}}_u \cdot \boldsymbol{\mathcal{S}}_u = F$. Differentiating this with respect to u gives

$$\partial_u(\boldsymbol{\mathcal{S}}_u \cdot \boldsymbol{\mathcal{S}}_u) = 2\boldsymbol{\mathcal{S}}_{uu} \cdot \boldsymbol{\mathcal{S}}_u = E_u. \tag{5.46}$$

Repeating this procedure for the rest of the inner products, we get

$$\boldsymbol{\mathcal{S}}_{uu} \cdot \boldsymbol{\mathcal{S}}_u = \frac{1}{2}E_u, \quad \boldsymbol{\mathcal{S}}_{uu} \cdot \boldsymbol{\mathcal{S}}_v = F_u - \frac{1}{2}E_v, \tag{5.47}$$

$$\boldsymbol{\mathcal{S}}_{uv} \cdot \boldsymbol{\mathcal{S}}_u = \frac{1}{2}E_v, \quad \boldsymbol{\mathcal{S}}_{uv} \cdot \boldsymbol{\mathcal{S}}_v = \frac{1}{2}G_u, \tag{5.48}$$

$$\boldsymbol{\mathcal{S}}_{vv} \cdot \boldsymbol{\mathcal{S}}_v = \frac{1}{2}G_v, \quad \boldsymbol{\mathcal{S}}_{vv} \cdot \boldsymbol{\mathcal{S}}_u = F_v - \frac{1}{2}G_u, \tag{5.49}$$

$$\hat{\boldsymbol{\mathcal{N}}}_{uu} \cdot \boldsymbol{\mathcal{S}}_u = -L_u + \frac{1}{2}\mathcal{W}_{11}E_u + \mathcal{W}_{12}(F_u - \frac{1}{2}E_v), \tag{5.50}$$

$$\hat{\boldsymbol{\mathcal{N}}}_{uu} \cdot \boldsymbol{\mathcal{S}}_v = -M_u + \frac{1}{2}\mathcal{W}_{11}E_v + \frac{1}{2}\mathcal{W}_{12}G_u, \tag{5.51}$$

$$\hat{\boldsymbol{\mathcal{N}}}_{uv} \cdot \boldsymbol{\mathcal{S}}_v = -M_v + \mathcal{W}_{11}(F_v - \frac{1}{2}G_u) + \frac{1}{2}\mathcal{W}_{12}G_v, \tag{5.52}$$

$$\hat{\boldsymbol{\mathcal{N}}}_{vu} \cdot \boldsymbol{\mathcal{S}}_u = -M_u + \frac{1}{2}\mathcal{W}_{21}E_u + \mathcal{W}_{22}(F_u - \frac{1}{2}E_v), \tag{5.53}$$

$$\hat{\boldsymbol{\mathcal{N}}}_{vv} \cdot \boldsymbol{\mathcal{S}}_u = -M_v + \frac{1}{2}\mathcal{W}_{21}E_v + \frac{1}{2}\mathcal{W}_{22}G_u, \tag{5.54}$$

$$\hat{\boldsymbol{\mathcal{N}}}_{vv} \cdot \boldsymbol{\mathcal{S}}_v = -N_v + \mathcal{W}_{21}(F_v - \frac{1}{2}G_u) + \frac{1}{2}\mathcal{W}_{22}G_v. \tag{5.55}$$

In the limit where $n \to 0$ the Christoffel symbols simplify substantially. This limit corresponds to the case where the vector is confined to the surfaces, meaning it cannot move along the normal vector, and is therefore very interesting to consider. The Christoffel symbols simplify as follows

$$\Gamma^1_{11} = \frac{1}{2|g|}(GE_u - 2FF_u + FE_v), \quad \Gamma^1_{12} = \frac{1}{2|g|}(GE_v - FG_u), \tag{5.56}$$

$$\Gamma^2_{11} = \frac{1}{2|g|}(2EF_u - EE_v - FE_u), \quad \Gamma^2_{12} = \frac{1}{2|g|}(EG_u - FE_v), \tag{5.57}$$

$$\Gamma^1_{22} = \frac{1}{2|g|}(2GF_v - GG_u - FG_v), \quad \Gamma^2_{22} = \frac{1}{2|g|}(EG_v - 2FF_v + FG_u), \tag{5.58}$$

$$\Gamma^1_{13} = -\mathcal{W}_{11}, \quad \Gamma^1_{23} = -\mathcal{W}_{12}, \quad \Gamma^2_{13} = -\mathcal{W}_{21}, \quad \Gamma^2_{23} = -\mathcal{W}_{22}, \tag{5.59}$$

and the rest of the Christoffel symbols vanish. In this thesis, we will only consider transport confined to a 2D surface, and will therefore use these expressions for the Christoffel symbols.

5.5 Examples of surfaces

To gain some intuition for how this formalism is used we will consider some examples of simple types of surfaces. For each surface, we will calculate the fundamental forms, then use these to investigate the curvatures of the surface and verify that we get the expected metric.

5.5.1 Flat surface

First we will consider a flat surface. There are multiple ways of parameterizing a flat surface. One can for example use either Cartesian coordinates or polar coordinates. In this section we will use Cartesian coordinates. We thus write our coordinate vector as $\boldsymbol{R}(x, y, z) = x\hat{\boldsymbol{x}} + y\hat{\boldsymbol{y}} + z\hat{\boldsymbol{z}}$. Choosing the xy-plane as our surface we see that

$$\boldsymbol{\mathcal{S}}(u, v) = u\hat{\boldsymbol{x}} + v\hat{\boldsymbol{y}} \quad \text{and} \quad z\hat{\boldsymbol{z}} = n\hat{\boldsymbol{\mathcal{N}}} \tag{5.60}$$

in our formalism. The basis vectors are thus found to be $\boldsymbol{\mathcal{S}}_x = \hat{\boldsymbol{x}}$, $\boldsymbol{\mathcal{S}}_y = \hat{\boldsymbol{y}}$ and $\hat{\boldsymbol{\mathcal{N}}} = \hat{\boldsymbol{z}}$. Calculating the first and second fundamental form is thus trivial, and gives us

$$E = G = 1 \quad \text{and} \quad F = L = M = N = 0. \tag{5.61}$$

By inserting this into the metric g we get the identity matrix as expected. We also find that both the Gaussian and the mean curvature reduce to 0, giving us no curvature on the surface, which is also expected.

5.5.2 Spherical surface

Next we will consider a spherical surface of radius R. We parameterize the surface as

$$\boldsymbol{\mathcal{S}}(u, v) = R(\sin(u)\cos(v)\hat{\boldsymbol{x}} + \sin(u)\sin(v)\hat{\boldsymbol{y}} + \cos(u)\hat{\boldsymbol{z}}). \tag{5.62}$$

We then find the tangential basis vectors and the normal vector to be

$$\boldsymbol{\mathcal{S}}_u = R(\cos(u)\cos(v)\hat{\boldsymbol{x}} + \cos(u)\sin(v)\hat{\boldsymbol{y}} - \sin(u)\hat{\boldsymbol{z}}), \tag{5.63}$$
$$\boldsymbol{\mathcal{S}}_v = R(-\sin(u)\sin(v)\hat{\boldsymbol{x}} + \sin(u)\cos(v)\hat{\boldsymbol{y}}), \tag{5.64}$$
$$\hat{\boldsymbol{\mathcal{N}}} = \sin(u)\cos(v)\hat{\boldsymbol{x}} + \sin(u)\sin(v)\hat{\boldsymbol{y}} + \cos(u)\hat{\boldsymbol{z}}, \tag{5.65}$$

where we found the expression for $\hat{\boldsymbol{\mathcal{N}}}$ by normalizing the cross product between $\boldsymbol{\mathcal{S}}_u$ and $\boldsymbol{\mathcal{S}}_v$. As usual we write the coordinate vector as $\boldsymbol{R}(u, v, r) = \boldsymbol{\mathcal{S}}(u, v) + r\hat{\boldsymbol{\mathcal{N}}}(u, v)$. We now find the first fundamental form by taking the appropriate inner products, giving us

$$E = R^2, \quad F = 0 \quad \text{and} \quad G = \sin^2(u)R^2. \tag{5.66}$$

In order to find the second fundamental form we first calculate the second derivatives of $\boldsymbol{\mathcal{S}}$,

$$\boldsymbol{\mathcal{S}}_{uu} = -\sin(u)\cos(v)\hat{\boldsymbol{x}} - \sin(u)\sin(v)\hat{\boldsymbol{y}} - \cos(u)\hat{\boldsymbol{z}}, \tag{5.67}$$
$$\boldsymbol{\mathcal{S}}_{vv} = -\sin(u)\cos(v)\hat{\boldsymbol{x}} - \sin(u)\sin(v)\hat{\boldsymbol{y}}, \tag{5.68}$$
$$\boldsymbol{\mathcal{S}}_{uv} = -\cos(u)\sin(u)\hat{\boldsymbol{x}} + \cos(u)\cos(v)\hat{\boldsymbol{y}}, \tag{5.69}$$

then take the inner product with $\hat{\boldsymbol{\mathcal{N}}}$ to find

$$L = -R, \quad M = 0 \quad \text{and} \quad N = -\sin^2(u)R. \tag{5.70}$$

Inserting this into the Weintgarten matrix we get

$$\mathcal{W} = \begin{pmatrix} -\frac{1}{R} & 0 \\ 0 & -\frac{1}{R} \end{pmatrix} \tag{5.71}$$

from which we can easily identify the principal curvatures as $\kappa_1 = \kappa_2 = -\frac{1}{R}$ and the Gaussian and mean curvatures as $K = \frac{1}{R^2}$ and $H = -\frac{1}{R}$. These results seem reasonable in comparison with a 1D curve with no torsion, for which the curvature is $\frac{1}{R}$[1]. I.e. the curvature of a spherical surface can be said to be the composition of two separate, circular curves with the same radius. This seems like a reasonable result.

Inserting the fundamental forms into the metric we get

$$g_{\text{sphere}} = \begin{pmatrix} (R+r)^2 & 0 & 0 \\ 0 & \sin^2(u)(R+r)^2 & 0 \\ 0 & 0 & 1 \end{pmatrix}, \tag{5.72}$$

which is the expected result for a spherical coordinate system.

5.5.3 Tunnel

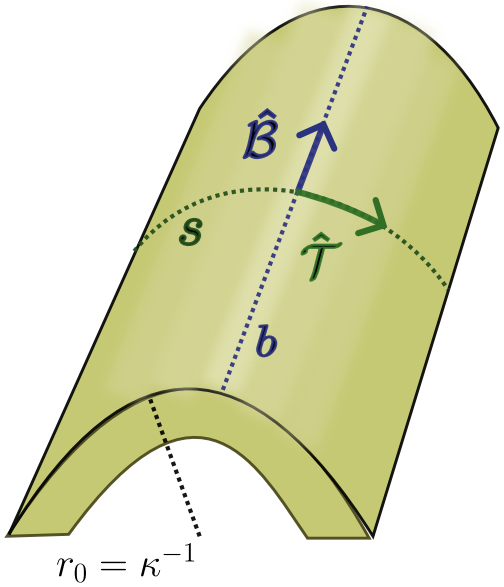

Figure 5.1: A tunnel surface, consisting of a 1D curve, with curvature $\kappa = r_0^{-1}$, stretched in the binormal direction.

We will now consider a system that hopefully makes the comparison with the curvilinear formalism that describes 1D curves, more lucid. Here we define a tunnel as a geometric figure which consists of a single curve stretched out in the binormal direction, as displayed in figure 5.1. We define the coordinate vector similarly to how we did in the 1D case,

$$\boldsymbol{R}(s, b, n) = \boldsymbol{r}(s) + b\hat{\boldsymbol{\mathcal{B}}} + n\hat{\boldsymbol{\mathcal{N}}}. \tag{5.73}$$

[1] the sign difference here is due to a difference in conventions in how we define the curvature

We have thus defined our surface as $\boldsymbol{\mathcal{S}}(s,b) = \boldsymbol{r}(s) + b\hat{\boldsymbol{\mathcal{B}}}$. We find the basis vectors to be $\boldsymbol{\mathcal{S}}_s = \hat{\boldsymbol{\mathcal{T}}}(s)$ and $\boldsymbol{\mathcal{S}}_b = \hat{\boldsymbol{\mathcal{B}}}$, where we assume that the parameterization of the curve $\boldsymbol{r}(s)$ is chosen such that $\hat{\boldsymbol{\mathcal{T}}}(s)$ is normalized. Doing this, the first fundamental form gives

$$E = 1, \quad F = 0 \quad \text{and} \quad G = 1. \tag{5.74}$$

To find the coefficients of the second fundamental form we use $\partial_s \hat{\boldsymbol{\mathcal{T}}}(s) = \kappa(s)\hat{\boldsymbol{\mathcal{N}}}(s)$ [2] to find that $L = \kappa(s)$. Here $\kappa(s)$ is the definition of curvature in the curvilinear coordinate system. $N = 0$ and $M = 0$ follows from orthogonality.

Inserting these values, we see that the Gaussian curvature is 0. This is as expected when considering a surface with curvature in only one dimension. The mean curvature, which is thus equal to the principal curvature, is equal to $\kappa(s)$. This verifies that our definition of curvature is consistent with the definition of curvature in torsion-less curvilinear coordinates. The metric is now found to be

$$g_{\text{tunnel}} = \begin{pmatrix} (1 - n\kappa(s))^2 & 0 & 0 \\ 0 & 1 & 0 \\ 0 & 0 & 1 \end{pmatrix} \tag{5.75}$$

which is exactly the same as the metric in the torsion-less curvilinear system.

5.5.4 Isotropic bump

Here, we consider a 2D surface, with a bump in the z-direction. The bump is modelled by some general isotropic function $f(r)$. By isotropic, we here mean that it is invariant under rotation around the z-axis. We parameterize the surface as

$$\boldsymbol{\mathcal{S}} = r\cos(\theta)\hat{\boldsymbol{x}} + r\sin(\theta)\hat{\boldsymbol{y}} + f(r)\hat{\boldsymbol{z}}. \tag{5.76}$$

In this example we will consider the 2D limit $n \to 0$ for simplicity. The basis vectors are thus given by

$$\boldsymbol{\mathcal{S}}_r = \cos(\theta)\hat{\boldsymbol{x}} + \sin(\theta)\hat{\boldsymbol{y}} + f'(r)\hat{\boldsymbol{z}}, \tag{5.77}$$

$$\boldsymbol{\mathcal{S}}_\theta = -r\sin(\theta)\hat{\boldsymbol{x}} + r\cos(\theta)\hat{\boldsymbol{y}}, \tag{5.78}$$

$$\hat{\boldsymbol{\mathcal{N}}} = (\boldsymbol{\mathcal{S}}_r \times \boldsymbol{\mathcal{S}}_\theta)/|\boldsymbol{\mathcal{S}}_r \times \boldsymbol{\mathcal{S}}_\theta| = E^{-\frac{1}{2}}(-\cos(\theta)f'(r)\hat{\boldsymbol{x}} - \sin(\theta)f'(r)\hat{\boldsymbol{y}} + \hat{\boldsymbol{z}}), \tag{5.79}$$

where the primed function denotes differentiation with respect to r. From this, we get

$$E = 1 + (f'(r))^2, \quad F = 0, \quad G = r^2, \tag{5.80}$$

$$L = f''(r)E^{-\frac{1}{2}}, \quad M = 0, \quad N = rf'(r)E^{-\frac{1}{2}}. \tag{5.81}$$

We see here that this coordinate system is orthogonal, which means that our choice of coordinates is decent. From this, the Weintgarten matrix is given by

$$\mathcal{W} = \begin{pmatrix} \frac{f''(r)}{E^{\frac{3}{2}}} & 0 \\ 0 & \frac{f'(r)}{rE^{\frac{1}{2}}} \end{pmatrix}, \tag{5.82}$$

[2] we justify the use of the Frenet-Serret equations here by noting that our parametrization of the surface is identical to the torsion-less curvilinear coordinates

from which we see that the basis vectors in (5.77)-(5.79) coincide with the principal vectors of the surface. Hence, the principal curvatures are given by the diagonal entries of $\mathcal{W}$. The Gaussian and mean curvature are found to be

$$H = \frac{1}{2r\sqrt{E}}\left(f'(r) + \frac{rf''(r)}{E}\right) \quad \text{and} \quad K = \frac{f''(r)f'(r)}{rE^2}. \tag{5.83}$$

Since we let $n \to 0$, the metric is seen to be

$$g = \begin{pmatrix} 1 + (f'(r))^2 & 0 & 0 \\ 0 & r^2 & 0 \\ 0 & 0 & 1 \end{pmatrix}. \tag{5.84}$$

For the purpose of solving the Usadel equation for this geometry, we also calculate the Christoffel symbols of this system. We get

$$\Gamma^r_{\alpha\beta} = \frac{1}{E}\begin{pmatrix} f'(r)f''(r) & 0 & -f''(r)/(\sqrt{E}) \\ 0 & -r & 0 \\ -f''(r)/(\sqrt{E}) & 0 & 0 \end{pmatrix}, \tag{5.85}$$

$$\Gamma^\theta_{\alpha\beta} = \frac{1}{r}\begin{pmatrix} 0 & 1 & 0 \\ 1 & 0 & -f'(r)/E^{\frac{3}{2}} \\ 0 & -f'(r)/E^{\frac{3}{2}} & 0 \end{pmatrix}, \tag{5.86}$$

$$\Gamma^n_{\alpha\beta} = \frac{1}{\sqrt{E}}\begin{pmatrix} f''(r) & 0 & 0 \\ 0 & rf'(r) & 0 \\ 0 & 0 & 0 \end{pmatrix}. \tag{5.87}$$

Writing this in terms of the first and second principal curvatures, we get

$$\Gamma^r_{\alpha\beta} = \begin{pmatrix} \kappa_1\kappa_2 rE & 0 & -\kappa_1 \\ 0 & -r/E & 0 \\ -\kappa_1 & 0 & 0 \end{pmatrix}, \tag{5.88}$$

$$\Gamma^\theta_{\alpha\beta} = \begin{pmatrix} 0 & r^{-1} & 0 \\ r^{-1} & 0 & -\kappa_2 \\ 0 & -\kappa_2 & 0 \end{pmatrix}, \tag{5.89}$$

$$\Gamma^n_{\alpha\beta} = \begin{pmatrix} \kappa_1 E & 0 & 0 \\ 0 & \kappa_2 r^2 & 0 \\ 0 & 0 & 0 \end{pmatrix}. \tag{5.90}$$

6 Usadel in 2D curved space

In this chapter, we turn our interest to the 2D Usadel equation for a curved surface. Most work done on the Usadel equation in two dimensions has either been numerical in the general case [90] [56], or analytical in simplifying limits [91] [57]. In this chapter, we will consider the Usadel equation on curved surfaces. Since we are predominantly interested in the effects of curvature on the system, we will ignore all kinds of SO coupling in our derivations and numerical solutions, setting $\hat{\boldsymbol{A}} = 0$. Starting from the Usadel equation in (2.34), we write this equation in tensor form

$$iD_F g^{ij}\mathcal{D}_i(\hat{g}^R\mathcal{D}_j\hat{g}^R) = [E\hat{\tau}_z + \hat{\Delta} + g^{ij}h_i\hat{\sigma}_j, \hat{g}^R], \tag{6.1}$$

where g^{ij} is the inverse of the metric tensor, and should not be confused with the Green's function matrix $\hat{g}^R$. Writing out the coordinate covariant derivatives gives us

$$iD_F g^{ij}(\partial_i(\hat{g}^R\partial_j\hat{g}^R) - \Gamma^k_{ij}\hat{g}^R\partial_k\hat{g}^R) = [E\hat{\tau}_z + \hat{\Delta} + g^{ij}h_i\hat{\sigma}_j, \hat{g}^R], \tag{6.2}$$

where we note that the indices i, j, k are summed over the two directions of propagation in our system. This equation will be expressed in the the spin-parameterized weak proximity limit, for different forms of surfaces, and solved numerically using the finite element method for PDEs.

6.1 Weak proximity limit

It is difficult to interpret analytical results from (6.2) as it is written. We therefore want to write this equation in the spin-parameterization in (3.19), under the weak proximity limit, in order to get a better understanding for the system. Starting from the equations

$$D_F\nabla^2\boldsymbol{d} = -2i(E\boldsymbol{d} + f_0\boldsymbol{h}), \tag{6.3}$$
$$D_F\nabla^2 f_0 = -2i(Ef_0 + \boldsymbol{h}\cdot\boldsymbol{d}), \tag{6.4}$$

derived in section 3.2.1, we write these equations on tensor form, as

$$D_F g^{ij}\mathcal{D}_i\mathcal{D}_j(\boldsymbol{e}^\alpha d_\alpha) = -2i(E\boldsymbol{d} + f_0\boldsymbol{h}), \tag{6.5}$$
$$D_F g^{ij}\mathcal{D}_i\mathcal{D}_j f_0 = -2i(Ef_0 + g^{\alpha\beta}h_\alpha d_\beta). \tag{6.6}$$

In accordance with the discussion in 4.2.1, it is important to note that the indices that originate from the gradients should only be summed over 2 directions, while the indices that originate from the d- and h-vector should be summed over 3 directions. In order to clearly separate these two types of indices, we denote indices that should be summed over twice by the Latin letters i, j and k, while the Greek indices α, β and γ should be summed over three times. Writing out the coordinate covariant derivatives in (6.5), we get

$$\begin{aligned} D_F g^{ij}\mathcal{D}_i\mathcal{D}_j(\boldsymbol{e}^\alpha d_\alpha) &= D_F g^{ij}(\partial_i\partial_j(\boldsymbol{e}^\alpha d_\alpha) - \Gamma^k_{ij}\partial_k(\boldsymbol{e}^\alpha d_\alpha)) \\ &= D_F g^{ij}(\partial_i\partial_j(\boldsymbol{e}^\alpha d_\alpha) - (\Gamma^k_{ij}(\partial_k d_\alpha) - \Gamma^k_{ij}\Gamma^\beta_{k\alpha}d_\beta)\boldsymbol{e}^\alpha). \end{aligned} \tag{6.7}$$

Following the same steps as in (4.65) for the term $\partial_i\partial_j(\boldsymbol{e}^\alpha d_\alpha)$, we finally get

$$D_F g^{ij}(\partial_i\partial_j d_\alpha - 2\Gamma^\beta_{j\alpha}\partial_i d_\beta - \Gamma^k_{ij}\partial_k d_\alpha - d_\beta(\partial_i\Gamma^\beta_{j\alpha} - \Gamma^\beta_{i\gamma}\Gamma^\gamma_{j\alpha} - \Gamma^k_{ij}\Gamma^\beta_{k\alpha})) = -2i(Ed_\alpha + f_0 h_\alpha), \quad (6.8)$$

which gives us one equation of motion for each of the three d-vector components if we let $\alpha = u, v, n$. For the singlet component, we get

$$D_F g^{ij}(\partial_i\partial_j f_0 - \Gamma^k_{ij}\partial_k f_0) = -2i(Ef_0 + g^{\alpha\beta}h_\alpha d_\beta). \quad (6.9)$$

The form of these equations is qualitatively very similar to their 1D versions in (4.66) and (4.70). The differences from the 1D system therefore lie in the possible new geometries one can explore in 2D, along with being able to consider phenomena that are inaccessible in 1D, such as magnetic flux, skyrmions and geodesics on surfaces. In order to obtain any concrete information from (6.8) and (6.9), we need to consider specific geometries, such that we can calculate the Christoffel symbols explicitly.

6.2 Numerical tools

In order to solve the 2D Usadel equation we require numerical computations. The Riccati parameterization is the most commonly used tool to simplify the implementation of the Usadel equation. In this thesis we will use this parameterization throughout all numerical computations. Furthermore, there are multiple methods for numerically solving PDEs, such as the finite difference method [92], finite element method [93] and the finite volume method [94]. In this thesis the finite element method is chosen, as this method allows for flexibility in the choice of geometry, which is a necessary advantage for our systems. We therefore use the PDE toolbox provided by MATLAB, which implicitly uses the finite element method. The numerical simulations have been run on the supercomputer Saga provided by UNINETT Sigma2 - the National Infrastructure for High Performance Computing and Data Storage in Norway. The MATLAB code for the systems considered in section 6.3 and 6.4 can be provided upon request.

6.2.1 Riccati parameterization

When implementing the Usadel equation for the retarded Green's function matrix, it is useful to parameterize $\hat{g}^R$ in specific ways. The Usadel equation in (2.34) is a set of 16 equations, due to the size of $\hat{g}^R$. However, due to the normalization conditions in (2.27) and the symmetries of $\hat{g}^R$, constraints are put on the number of degrees of freedom in the Green's function matrix. If we parameterize $\hat{g}^R$ in a way that preserves these properties, we can thus reduce the number of equations in (2.34). The most used parameterization for computational purposes is the Riccati parameterization, where $\hat{g}^R$ is written in terms of a 2×2 matrix, $\underline{\gamma}$, and its tilde-conjugate $\underline{\tilde{\gamma}}$. In the Riccati parameterization, $\hat{g}^R$ is given by

$$\hat{g}^R = \begin{pmatrix} \underline{N} & 0 \\ 0 & -\underline{\tilde{N}} \end{pmatrix} \begin{pmatrix} 1 + \underline{\gamma\tilde{\gamma}} & 2\underline{\gamma} \\ 2\underline{\tilde{\gamma}} & 1 + \underline{\tilde{\gamma}\gamma} \end{pmatrix}, \quad (6.10)$$

where $\underline{N} = (1 - \underline{\gamma\tilde{\gamma}})$. Inserting this expression for $\hat{g}^R$ into the Usadel equation, we get [11]

$$iD_F(\nabla^2\underline{\gamma} + 2(\nabla\underline{\gamma})\cdot(\underline{\tilde{N}}\underline{\tilde{\gamma}}\nabla\underline{\gamma})) = \underline{\Delta} - \underline{\gamma}\underline{\Delta}^*\underline{\gamma} + \boldsymbol{h}\cdot(\underline{\boldsymbol{\sigma}}\underline{\gamma} - \underline{\gamma}\underline{\boldsymbol{\sigma}}^*) + 2E\underline{\gamma}, \tag{6.11}$$

$$iD_F(\nabla^2\underline{\tilde{\gamma}} + 2(\nabla\underline{\tilde{\gamma}})\cdot(\underline{N}\underline{\gamma}\nabla\underline{\tilde{\gamma}})) = -\underline{\Delta}^* + \underline{\tilde{\gamma}}\underline{\Delta}\underline{\tilde{\gamma}} - \boldsymbol{h}\cdot(\underline{\boldsymbol{\sigma}}^*\underline{\tilde{\gamma}} - \underline{\tilde{\gamma}}\underline{\boldsymbol{\sigma}}) + 2E\underline{\tilde{\gamma}}. \tag{6.12}$$

Here, equation (6.12) is the tilde-conjugated version of (6.11). Since these equations are coupled we have to solve both simultaneously. Thus, equations (6.11)-(6.12) describe a set of 8 coupled nonlinear PDEs. We should also write the Kupriyanov-Lukichev boundary conditions in (2.35) in terms of the gamma-matrices as well. We get [56]

$$\hat{\boldsymbol{n}}\cdot\nabla\underline{\gamma}_i = \mp\frac{1}{L_i\zeta_i}(1 - \underline{\gamma}_i\underline{\tilde{\gamma}}_j)\underline{N}_j(\underline{\gamma}_i - \underline{\gamma}_j), \tag{6.13}$$

$$\hat{\boldsymbol{n}}\cdot\nabla\underline{\tilde{\gamma}}_i = \mp\frac{1}{L_i\zeta_i}(1 - \underline{\tilde{\gamma}}_i\underline{\gamma}_j)\underline{\tilde{N}}_j(\underline{\tilde{\gamma}}_i - \underline{\tilde{\gamma}}_j), \tag{6.14}$$

where the positive sign should be used for when material j is to the left of material i, and the negative sign should be used when material j is to the right. $\hat{\boldsymbol{n}}$ here refers to the normal vector of the interface.

6.2.2 The finite element method

In this thesis, the numerical calculations of 2D systems are done using MATLAB's PDE toolbox. This toolbox applies the finite element method when solving PDEs. In this section, we therefore give a brief introduction to the finite element method, along with some details concerning the implementation of PDEs in MATLAB. This introduction to the finite element method is inspired by Amundsen's master thesis (2016) [66].

To start our discussion of the finite element method, let us consider the Poisson equation, in the form

$$\nabla^2 u + f(\boldsymbol{r}) = 0, \quad \text{for} \quad u \in \Omega, \tag{6.15}$$

where $f(\boldsymbol{r})$ is some general function, defined on some domain Ω. In order for this PDE to be well defined we need to establish some boundary conditions (BCs) on the boundary of the domain, $\partial\Omega$. Finite element theory distinguishes between two general types of boundary conditions, *Dirichlet boundary conditions* and *Neumann boundary conditions*. Dirichlet BCs are given by the general form $u = q(\boldsymbol{r})$, and Neumann BCs are given by $\hat{\boldsymbol{n}}\cdot\nabla u = q(\boldsymbol{r})$, where the vector $\hat{\boldsymbol{n}}$ is normal to the boundary surface. From these forms, we see that the Kupriyanov-Lukichev BCs are on the Neumann form. We will therefore consider Neumann BCs for the rest of this section.

By multiplying equation (6.15) with an arbitrary test function v, and integrating over the domain Ω, we get [93]

$$\int_\Omega d\boldsymbol{r}\nabla u\cdot\nabla v = \int_\Omega d\boldsymbol{r} f(\boldsymbol{r})v + \int_{\partial\Omega} dSq(\boldsymbol{r})v, \tag{6.16}$$

where we have used the divergence theorem and inserted the Neumann BCs. This expression describes the *weak formulation* for Neumann BCs. This formulation of the PDE in (6.15) is the starting point for the finite element method. The solution u is assumed to exist in a Hilbert space $\mathcal{H}$. Since the Hilbert space is spanned by a set of basis functions $l_i(\boldsymbol{r})$, we may expand u and v in terms of linear combinations of these functions. In order

for this expansion to be useful, the Hilbert space $\mathcal{H}$ must be finite in dimension. Since $\mathcal{H}$ is generally infinite in dimension, we therefore approximate this space by truncating it. This approximation is known as the *Galerkin approximation*. The resulting space is the truncated Hilbert space $\mathcal{H}^*$, with dimension N, where the functions u and v can now be expanded as

$$u^*(\boldsymbol{r}) = \sum_{i=1}^{N} u_i^* l_i(\boldsymbol{r}), \quad v(\boldsymbol{r}) = \sum_{i=1}^{N} v_i l_i(\boldsymbol{r}). \tag{6.17}$$

Here, u^* is the approximate solution to the PDE under the Galerkin approximation. Inserting these expressions into the weak formulation in (6.16), we get

$$\sum_{i=1}^{N} u_i^* \int_\Omega d\boldsymbol{r} \nabla l_i(\boldsymbol{r}) \cdot \nabla l_j(\boldsymbol{r}) = \int_\Omega d\boldsymbol{r} f(\boldsymbol{r}) l_j(\boldsymbol{r}) + \int_{\partial\Omega} dS q(\boldsymbol{r}) l_j(\boldsymbol{r}). \tag{6.18}$$

This can be written on matrix form. By defining the matrix

$$\boldsymbol{K}_{ji} = \int_\Omega d\boldsymbol{r} \nabla l_i(\boldsymbol{r}) \cdot \nabla l_j(\boldsymbol{r}), \tag{6.19}$$

and the vector

$$\boldsymbol{F}_j = \int_\Omega d\boldsymbol{r} f(\boldsymbol{r}) l_j(\boldsymbol{r}) + \int_{\partial\Omega} dS q(\boldsymbol{r}) l_j(\boldsymbol{r}), \tag{6.20}$$

we get

$$\boldsymbol{K}\boldsymbol{u}^* - \boldsymbol{F} = 0. \tag{6.21}$$

Here, $\boldsymbol{K}$ is referred to as the *stiffness matrix* and $\boldsymbol{F}$ the *force vector*, from their usage in structural mechanics.

Let us now recall that our starting point for this derivation was the linear PDE in (6.15). This equation can be made nonlinear by letting the function f depend on the solution u and its gradient ∇u, such that the equation now takes the form

$$\nabla^2 u + f(\boldsymbol{r}, u, \nabla u) = 0, \quad u \in \Omega. \tag{6.22}$$

Following the steps we just outlined to arrive at (6.21), we see that the force vector now depends on $\boldsymbol{u}^*$. This dependency on $\boldsymbol{u}^*$ means that we must solve the equation

$$\boldsymbol{K}\boldsymbol{u}^* - \boldsymbol{F}(\boldsymbol{u}^*) = 0 \tag{6.23}$$

to find the solution $\boldsymbol{u}^*$. This equation is generally nonlinear, and because of this the Newton-Raphson method [95] is used to find an approximation to $\boldsymbol{u}^*$. Given the vector equation $\boldsymbol{f}(\boldsymbol{x}) = 0$, the Newton-Raphson method approximates the solution $\boldsymbol{u}^*$ by the iteration scheme given by

$$\boldsymbol{x}_{n+1} = \boldsymbol{x}_n - \boldsymbol{J}^{-1}(\boldsymbol{x}_n)\boldsymbol{f}(\boldsymbol{x}_n), \tag{6.24}$$

where $\boldsymbol{J}(\boldsymbol{x})$ is the Jacobian matrix to $\boldsymbol{f}(\boldsymbol{x})$. For (6.21), this iteration scheme takes the form

$$\boldsymbol{u}_{n+1}^{*(\alpha)} = \boldsymbol{u}_{n}^{*(\alpha)} - (\boldsymbol{K}_{\boldsymbol{T}}^{-1})^{(\alpha\beta)}(\boldsymbol{K}\boldsymbol{u}^{*} - \boldsymbol{F})^{(\beta)}, \tag{6.25}$$

where the matrix $\boldsymbol{K_T}$ is called the tangent stiffness matrix, and is given by

$$\boldsymbol{K}_{\boldsymbol{T}}^{(\alpha\beta)} = \delta_{\alpha\beta}\boldsymbol{K} - \frac{\partial \boldsymbol{F}^{(\alpha)}}{\partial \boldsymbol{u}^{*(\beta)}}. \tag{6.26}$$

The matrix equation in (6.21) can now be solved to find the coefficients $\boldsymbol{u}^*$. In order to do this $\boldsymbol{K}$ and $\boldsymbol{F}$ must be determined, which can only be done once we have chosen a suitable basis for $\mathcal{H}^*$. The Stone-Weierstrass theorem [96] states that we can use polynomials to approximate any continuous function on a closed domain as accurately as we like. The usual choice for this basis is therefore polynomials. The domain Ω is then divided into a set of subdomains Ω_e, referred to as *elements*. Each domain is assigned a set of points where the solution to the PDE is computed. These points are referred to as *nodes*. The basis functions in a subdomain are determined by interpolation through the nodes of the subdomain. In order for the solution to be continuous across the subdomain boundaries there has to be nodes on the edges and vertices of bordering subdomains, as can be seen in figure 6.1. The partition of the domain Ω into subdomains is referred to as a *mesh*. The quality of the approximation u^* to u is inherently dependent upon the quality of the mesh.

In MATLAB, a mesh can be generated from the function *generateMesh()*, given an arbitrary geometry. This function generates triangular (in 2D) or tetrahedral (in 3D) elements. An example of a mesh generated by MATLAB for a quadratic geometry is given in figure 6.1. Unfortunately, there is no flexibility in choosing the shape of the elements. Therefore, one has to choose appropriate sizes for the elements in order to get approximations of sufficient quality. The process of placing nodes and interpolating between them to get basis functions is fully automated by MATLAB. Because of this we will not cover the details of how this is done, in this thesis. Instead, we refer to the work of Amundsen [66] [90] for discussions on this topic.

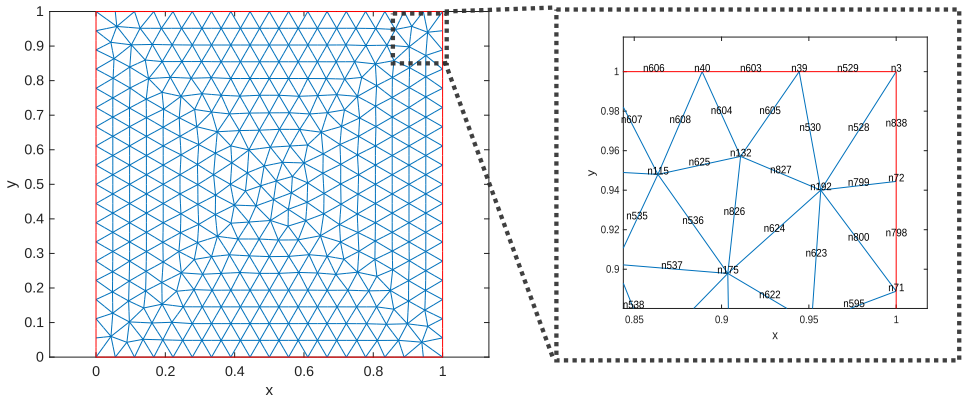

Figure 6.1: An example of a mesh with triangular elements generated using MATLAB. The zoomed in plot displays the placement and labelling of the nodes in the elements. The nodes are labelled by 'n#', where # denotes the number of the node.

The PDE toolbox in MATLAB addresses equations in the form

$$m\partial_t^2 u + d\partial_t u - \nabla \cdot (c\nabla u) + au = f, \tag{6.27}$$

with Neumann boundary conditions in the form

$$\hat{\boldsymbol{n}} \cdot (c\nabla u) + qu = g. \tag{6.28}$$

For a system of M equations in 2D, u, f and g are vectors with M components, where u describes the solution, a and q are $M \times M$ matrices and c is an $M \times M \times 2 \times 2$ tensor. m and d are set to 0 in this thesis since the Usadel equation is independent of time. Notably, f, a and c are allowed to depend on both u and ∇u, meaning that we can write any version of the Usadel equation in this form. Furthermore, equation (6.27) is written on divergence form, given the term $\nabla \cdot (c\nabla u)$. For a system where $M = 1$, this term takes the form

$$\nabla \cdot (c\nabla u) = c_1\partial_x^2 + (c_2 + c_3)\partial_x\partial_y u + c_4\partial_y^2 u + (\partial_x c_1 + \partial_y c_2)\partial_x u + (\partial_x c_3 + \partial_y c_4)\partial_y u, \tag{6.29}$$

where $c = \begin{pmatrix} c_1 & c_3 \\ c_2 & c_4 \end{pmatrix}$. In order to put an equation in divergence form, the components of c should be matched with the equation of interest according to (6.29). For example, in coordinate representations where the metric tensor is the identity matrix we get $c_1 = c_4 = D_F$ and $c_2 = c_3 = 0$ for the Usadel equation. It should be noted that the c in (6.27) and (6.28) is the same one. Hence, once the c is determined in the PDE care should be taken to make sure that the boundary conditions take the correct form for the given c.

The Usadel equation in the Riccati parameterization can now be written in the form of (6.29). Let us define the solution vector

$$\Gamma = [\gamma_1, \gamma_2, \gamma_3, \gamma_4, \tilde{\gamma}_1, \tilde{\gamma}_2, \tilde{\gamma}_3, \tilde{\gamma}_4]^T, \tag{6.30}$$

where $\gamma = \begin{pmatrix} \gamma_1 & \gamma_3 \\ \gamma_2 & \gamma_4 \end{pmatrix}$. The Usadel equation in a general geometry then takes the form

$$g^{ij}\partial_i\partial_j\Gamma^\alpha = Q^\alpha(\gamma, \tilde{\gamma}, \nabla\gamma, \nabla\tilde{\gamma}), \tag{6.31}$$

with boundary conditions

$$\hat{\boldsymbol{n}} \cdot \nabla\Gamma^\alpha = B^\alpha(\gamma, \tilde{\gamma}). \tag{6.32}$$

Here, the functions Q^α and B^α should be interpreted as conducting the matrix multiplications dictated by the given Usadel equation, and extracting the α^{th} element. The function Q thus determines a and f, while B determines q and g, and the inverse metric g^{ij} determines c. When simulating the curved surfaces numerically, we map the geometries to a corresponding flat geometry. We justify this by observing that the metric and Christoffel symbols in the Usadel equation compensate for this mapping.

6.3 2D tunnel

The 2D tunnel surface, visualized in figure 5.1, consists of a constant 1D curvature extended in the binormal direction. This surface can be described by letting b be a finite parameter in the curved nanowire system introduced in section 4.4. In the torsion-less curvilinear framework, all the Christoffel symbols involving the parameter b are zero. We can therefore find all the relevant Usadel equations for this system simply by replacing the second order derivatives in section 4.4 with Laplacians in 2D, $\partial_s^2 \to \nabla^2 = \partial_s^2 + \partial_b^2$. This gives us

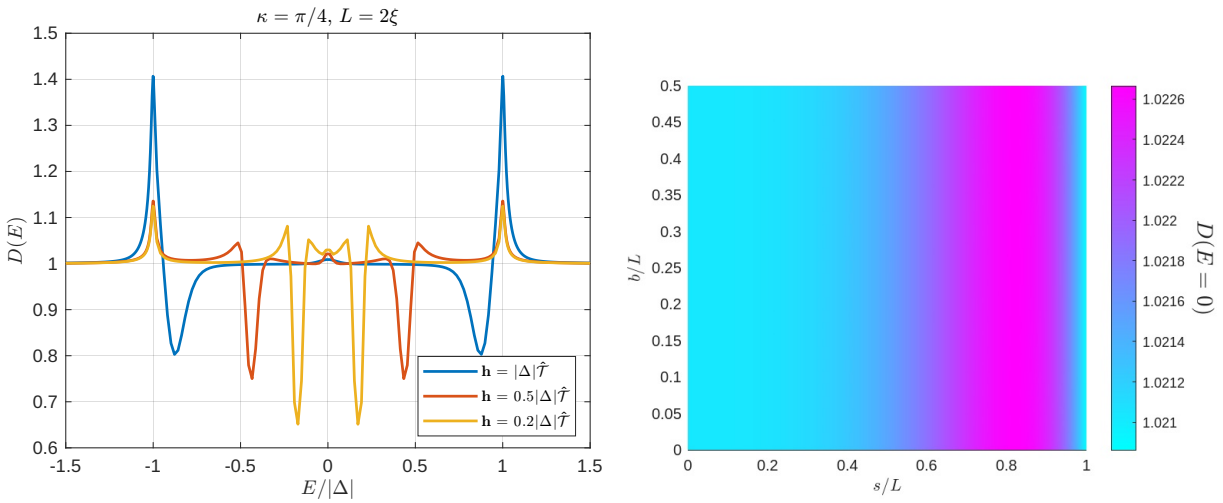

(a) (b)

Figure 6.2: Density of states for a 2D SF tunnel, with curvature $\kappa = \pi/4$, length $L = 2\xi$ and width $W = \xi$. The superconductor is placed at $L = 2\xi$, to the right of the ferromagnet. (a) Density of states as a function of the energy $E/|\Delta|$ for various exchange fields $\boldsymbol{h}$. (b) Spatial dependency of the density of states at 0 energy for $\boldsymbol{h} = 0.5|\Delta|\hat{\boldsymbol{\mathcal{T}}}$.

$$iD_F\partial_i(\hat{g}^R\partial_i\hat{g}^R) = [E\hat{\tau}_z + \hat{\Delta} + h_\alpha\hat{\sigma}_\alpha, \hat{g}^R], \tag{6.33}$$

where we once again see that the effects of curvature enter through the curving of the exchange field, seen in the terms $h_\alpha\hat{\sigma}_\alpha$.

In the spin-parameterized weak proximity limit, we get

$$D_F(\partial_s^2 d_s + \partial_b^2 d_s - 2\kappa\partial_s d_n - \kappa^2 d_s) = -2i(Ed_s + f_0 h_s), \tag{6.34}$$
$$D_F(\partial_s^2 d_n + \partial_b^2 d_n + 2\kappa\partial_s d_s - \kappa^2 d_n) = -2i(Ed_n + f_0 h_n), \tag{6.35}$$
$$D_F(\partial_s^2 d_b + \partial_b^2 d_b) = -2i(Ed_b + f_0 h_b), \tag{6.36}$$
$$D_F(\partial_s^2 f_0 + \partial_b^2 f_0) = -2i(Ef_0 + \boldsymbol{h}\cdot\boldsymbol{d}). \tag{6.37}$$

Thus, the 2D tunnel system should look qualitatively the same as the 1D nanowire system, with respect to spin-rotation, and we expect the transport properties to be similar to the 1D system. Furthermore, this system serves as a benchmark for comparing 2D to 1D systems. That is, when we are solving the Usadel equation numerically, we need ways to make sure our results make sense. Since the tunnel system should yield similar results as the 1D curved nanowire, we can use this system as a benchmark for evaluating the results we see in 2D.

When solving this system numerically, the Riccati parameterization gives us

$$iD_F(\partial_i\partial_i\underline{\gamma} + 2(\partial_i\underline{\gamma})\underline{\tilde{N}}\underline{\tilde{\gamma}}(\partial_i\underline{\gamma})) = h_\alpha(\underline{\sigma}_\alpha\underline{\gamma} - \underline{\gamma}\underline{\sigma}_\alpha^*) + 2E\underline{\gamma}, \tag{6.38}$$

This equation has been solved using the PDE toolbox in MATLAB. The system we have considered is an SF tunnel with constant curvature $\kappa = \pi/4$, length $L = 2\xi$ and width $W = \xi$, where the superconductor is placed at $L = 2\xi$, to the right of the ferromagnet. The density of states for this system has been plotted for various exchange field strengths in figure 6.2(a). Here, we see that the density of states for $\boldsymbol{h} = |\Delta|\hat{\boldsymbol{\mathcal{T}}}$ is almost identical to

the density of states in the 1D nanowire, with the same material parameters, as plotted in figure 4.4. This confirms that the 2D tunnel system behaves the same way as the 1D nanowire system. Furthermore, figure 6.2 also displays peaks at zero energy, indicating the presence of triplets. Following the analysis of spin rotation in the 1D nanowire system, it is natural to assume that these peaks are due to a mixture of d_N and d_T components. This confirms that we also see spin rotation the tunnel system, as we would expect. Figure 6.2 also shows us how an increase in the exchange field strength destroys the features in the density of states around $E = 0$, as mentioned in section 3.5. In figure 6.2(b) we have plotted the spatial dependency of the density of states throughout the ferromagnet, at $E = 0$, for $\boldsymbol{h} = 0.5|\Delta|\hat{\boldsymbol{T}}$. Here, we see that the density of states is invariant under translation in the binormal direction, as expected. Furthermore, the peak increases initially from the interface, before it decays again longer away from the interface. We may understand this in light of the discussion in 4.4.1, where we saw that the generation of LRTs happens gradually with curvature, before the triplets start to decay.

6.4 2D boomerang

The 2D *boomerang* system, visualized in figure 6.3, is based on a constant 1D curve that has extension in its normal direction. Thus, we can describe this system with curvilinear coordinates, while allowing the normal component n to be a finite parameter. Although this system is effectively described by a 1D curvature, the extension in the normal direction introduces some new mechanisms to the transport of quasiparticles in the system that we didn't see in the 2D tunnel system. The reason for this is that the curvature $\kappa = r_0^{-1}$ will vary as we vary the normal component n. This means that the Christoffel symbols Γ^s_{ns}, Γ^s_{sn} and Γ^n_{ss} now contribute to the Laplacian in the Usadel equation.

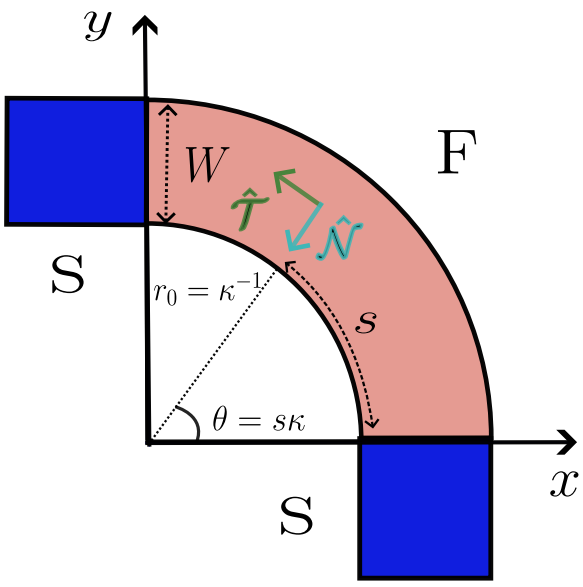

Figure 6.3: A curved superconductor (S) - ferromagnet (F) - superconductor *boomerang* setup with width W, parameterized after the inner arc length s and radius r_0.

Another way to understand why one might expect this system to behave qualitatively differently from the 1D nanowire system is to notice that the path of the quasiparticles

through the ferromagnet is expected to be the path that minimizes energy loss. Normally in flat systems, this is the shortest path between the two superconductors. But since curvature acts as a friction force, we expect the quasiparticles to take the path of least curvature. In this boomerang system, the shortest path is the path with the most curvature, and the path with the least curvature is the longest path. This system therefore allows us to study which path the quasiparticles will take under these constraints, allowing us to study effective geodesics in our systems. One point we have ignored in this reasoning is that the curvature also creates LRTs, which tends to yield a higher current density in the ferromagnet. This mechanic therefore favours transport along steeper curvature, despite the friction effect of the curvature. On the other hand, results from the 1D nanowire indicate that the spin-rotation effect due to curvature is not necessarily linear in curvature. That is, beyond a certain curvature, the LRT generation does not increase as we increase the curvature. Hence, the competition between path distance and steepness of curvature is expected to be relevant only beyond some critical curvature. Furthermore, we have demonstrated that varying curvature may induce a 0-π transition in the junction. Since the boomerang shape has a naturally varying curvature along the normal vector, we expect the current density to change sign along this direction, at some specific curvature.

We consider a system similar to the nanowire system in section 4.4, but with a finite n. By parameterizing the 3D coordinate vector the same way, we get

$$\boldsymbol{R}(s,n,b) = (r_0 - n)\cos(s/r_0)\hat{x} + (r_0 - n)\sin(s/r_0)\hat{y} + b\hat{z}, \tag{6.39}$$

where r_0 is now defined as the radius from the center of the circle to the inner curve of the thin film. Since we are using curvilinear coordinates, the metric is given in (4.41). The Christoffel symbols are given by (4.43)-(4.45), and come out to be

$$\Gamma^s_{ss} = 0, \tag{6.40}$$
$$\Gamma^n_{ss} = \eta(n)\kappa, \tag{6.41}$$
$$\Gamma^s_{sn} = \Gamma^s_{ns} = -\eta(n)^{-1}\kappa, \tag{6.42}$$

where we have defined $\eta = 1 - n\kappa$. We note here that the curvature $\kappa = r_0^{-1}$ now denotes the curvature of the inner edge of the thin film, and is not a general expression for the curvature in this system. The reason that the curvature of the inner edge enters our equations in particular is because we have now parameterized our coordinate system from the 1D formalism, where $n = 0$ confines us to the inner curve, and the parameter s refers to the arc length of the inner curve. This should not worry us, however, as this approach still gives us the correct results. Entering the Christoffel symbols into the Usadel equation, we get

$$D_F(\eta^{-2}\partial_s(\hat{g}^R\partial_s\hat{g}^R) + \partial_n(\hat{g}^R\partial_n\hat{g}^R) - \kappa_n(n)(\hat{g}^R\partial_n\hat{g}^R)) = [E\hat{\tau}_z + h_{(\alpha)}\hat{\sigma}_{(\alpha)}, \hat{g}^R]. \tag{6.43}$$

Here, we have defined $\kappa_n(n) = \eta^{-1}\kappa = (r_0 - n)^{-1}$ as the actual curvature at any distance n from the κ curve. Furthermore, the exchange field terms have been written in terms of the physical vectors, as this the most natural expression for these quantities. The reason for this is that the exchange field will naturally follow the tangential vector, which is equivalent to the physical vector in the s direction in curvilinear coordinates. The physical vector components of the Pauli matrices are equivalent to the covariant vector

components in the 1D limit, since the metric tensor becomes the identity matrix, as discussed in section 4.4. The expressions for $\underline{\sigma}_{(\alpha)}$ are therefore given by 4.63.

In the spin-parameterized weak proximity limit, we get

$$D_F\left[\eta^{-2}\partial_s^2 d_s + \partial_n^2 d_s + \kappa_n(\partial_n d_s) - 2\kappa_n(\partial_s d_n) + 2\kappa_n^2 d_s\right] = -2i(Ed_s + f_0 h_s), \tag{6.44}$$

$$D_F\left[\eta^{-2}\partial_s^2 d_n + \partial_n^2 d_n + 2\eta^{-2}\kappa_n(\partial_s d_s) - \kappa_n(\partial_n d_n) - \kappa_n^2 d_n\right] = -2i(Ed_n + f_0 h_n), \tag{6.45}$$

$$D_F\left[\eta^{-2}\partial_s^2 d_b + \partial_n^2 d_b - \kappa_n(\partial_n d_b)\right] = -2i(Ed_b + f_0 h_b), \tag{6.46}$$

$$D_F\left[\eta^{-2}\partial_s^2 f_0 + \partial_n^2 f_0 - \kappa_n(\partial_n f_0)\right] = -2i(Ef_0 + \boldsymbol{h}\cdot\boldsymbol{d}). \tag{6.47}$$

In comparing these equations with the tunnel system in (6.34)-(6.37), we clearly see that the difference between these two systems lies in the transport along non-tangential direction. While the transport in the tunnel system is invariant under translation along the binormal direction, the boomerang system is not invariant under translation along the normal direction. Hence, these equations confirm our expectations, in that the transport should vary along the normal direction. Furthermore, we notice that (6.44) can be rewritten as

$$D_F\left[\eta^{-2}\partial_s^2 d_s + \partial_n^2 d_s - \kappa(\nabla\times\boldsymbol{d})\cdot\hat{\boldsymbol{\mathcal{B}}} - \kappa_n(\partial_s d_n) + 2\kappa_n^2 d_s\right] = -2i(Ed_s + f_0 h_s), \tag{6.48}$$

using (4.28). Here, the term $\kappa(\nabla\times\boldsymbol{d})\cdot\hat{\boldsymbol{\mathcal{B}}}$ indicates the possibility of having current vortices on the surface.

Solving this system numerically, we first have to find the corresponding Riccati parameterized Usadel equation. Assuming that the exchange field will follow the tangential direction, we get

$$\begin{aligned} iD_F(\eta^{-2}\partial_s^2\underline{\gamma} + \partial_n^2\underline{\gamma} + 2\eta^{-2}(\partial_s\underline{\gamma})\underline{\tilde{N}}\underline{\tilde{\gamma}}(\partial_s\underline{\gamma}) + 2(\partial_n\underline{\gamma})\underline{\tilde{N}}\underline{\tilde{\gamma}}(\partial_n\underline{\gamma}) - \kappa\eta^{-1}\partial_n\underline{\gamma}) \\ = h_T(\underline{\sigma}_{(s)}\underline{\gamma} - \underline{\gamma}\underline{\sigma}^*_{(s)}) + 2E\underline{\gamma}. \end{aligned} \tag{6.49}$$

This equation has been solved numerically using the PDE toolbox provided by MATLAB. The system considered is visualized in figure 6.3. This SFS boomerang system is considered for various inner curvatures $\kappa = r_0^{-1}$. It should be noted that the goal with these computations is not to explore the parameter space, but to demonstrate that this framework for solving 2D surfaces works. In figure 6.4, we have plotted the charge current density vector on the boomerang surface with width $W = \xi$, length $L = 2\xi$, phase difference $\phi = \pi/2$ and exchange field $|\Delta|\hat{\boldsymbol{\mathcal{T}}}$, for $\kappa L = 3.56$. With this inner curvature, the outer curvature of this surface is approximately $\kappa_{outer}L = 1.28$. Hence, according to figure 4.5 we expect there to be a reversal of the charge current around $\kappa_n L = 1.88$. What we observe in figure 6.4 is naturally more complex than this, but a curvature-dependent direction of the current can still be traced out. More interestingly, this system features a vortex-like whirl of the current, as predicted from (6.48). A superconducting vortex is a topological feature, in which the superconducting phase shifts by $n2\pi$ around the vortex center, where n is some integer. In order to demonstrate the presence of vortices on a surface, the pair correlation function must be investigated [56]. Hence the whirl of currents in figure 6.4 can not be said to equate to the presence of superconducting vortices, but could be indicative. Because of this, investigating the correlation function for this system to prove the potential presence of vortices would be a natural continuation of this study.

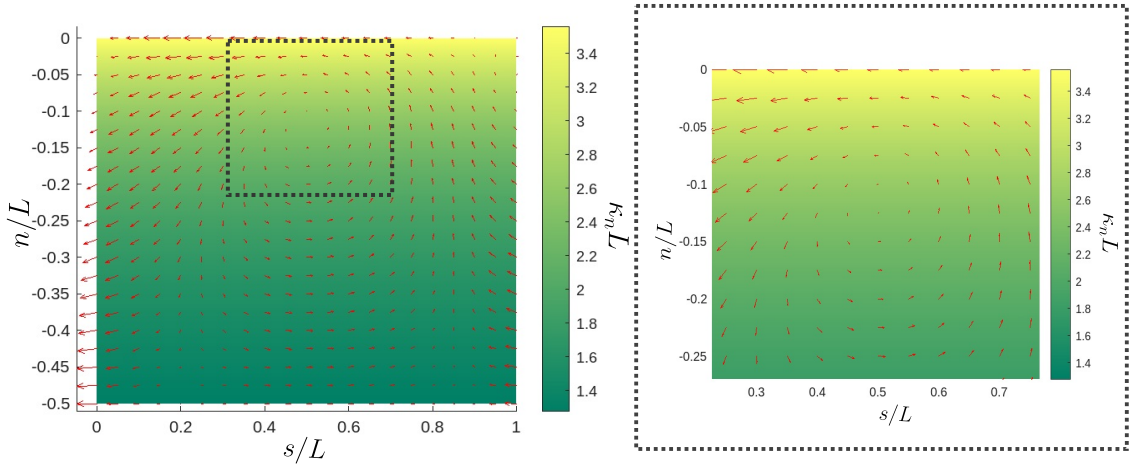

Figure 6.4: The charge current density vector plotted on a boomerang surface with inner curvature $\kappa = 1.78L$ for an SFS system. The length is $L = 2\xi$, width is $W = \xi$, exchange field is $\boldsymbol{h} = |\Delta|\hat{\boldsymbol{\mathcal{T}}}$ and the phase difference is $\varphi = \pi/2$.

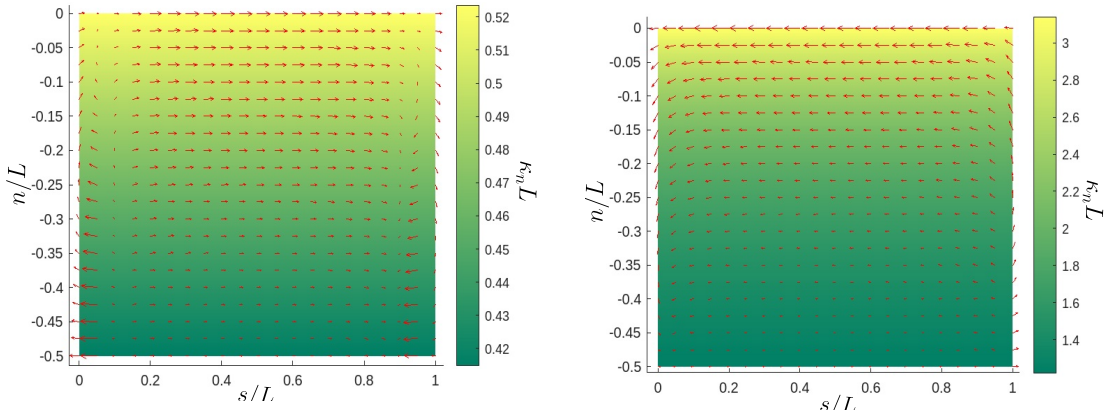

(a) (b)

Figure 6.5: The charge current density vector plotted on two different SFS boomerang systems with exchange field $\boldsymbol{h} = |\Delta|\hat{\boldsymbol{\mathcal{T}}}$ and the phase difference $\varphi = \pi/2$. (a) The length is $L = 4\xi$, the width is $W = 2\xi$ and the inner curvature is $\kappa L = \pi/6$. (b) The length is $L = 2\xi$, the width is $W = \xi$ and the inner curvature is $\kappa L = \pi$.

In figure 6.5, we have plotted the charge current density vector for an SFS boomerang surface with phase difference $\phi = \pi/2$ and exchange field $|\Delta|\hat{\boldsymbol{\mathcal{T}}}$. In figure 6.5(a) the length is $L = 4\xi$, the width is $W = 2\xi$ and the inner curvature is $\kappa L = \pi/6$, and in figure 6.5(b) the length is $L = 2\xi$, the width is $W = \xi$ and the inner curvature is $\kappa L = \pi$. Here, the charge current seems to favor the path along the inner curvature in both cases. The current in the bulk moves in the opposite direction in the two systems, according to the plot in 4.5. Interestingly, the current seems to switch direction close to the interface. This is unphysical, since the total current through any cross section along the normal direction should be constant along the tangential direction. Because of this, there is reason to believe that there is an error in the code used for these plots. This error is likely in the implementation of the boundary conditions for the systems in figure 6.4 and 6.5, as it looks like the currents are physically sound throughout most of the bulk of the ferromagnets, until the boundaries are met. Furthermore, the accuracy of these numerical simulations

should be verified more thoroughly. For example, one should simulate the same system without mapping the geometry to a rectangle in order to verify that this yields the same result. One should also compute this system for various element sizes in order to verify that the Galerkin approximation in the finite element method is sufficiently accurate. Because of this, these plots should not be interpreted as true representations of the physics in these systems, but as indications of the possible dynamics that may arise. The plots should also be interpreted as indications that the formalism and methods developed in this thesis are successful in describing 2D curved systems.

6.5 Isotropic bump

Next we consider an isotropic bump, as described in section 5.5.4. Here, material deformation is described by a bump in the xy-plane modeled by a function $f(r)$ that is invariant under rotation around the z-axis. An example of how this surface might look for a Gaussian function is given in figure 6.6. In section 5.5.4, we found that the metric for this surface is given by

$$g = \text{diag}(\mu, r^2, 1), \tag{6.50}$$

where $\mu = 1 + (f'(r))^2$, and the prime denotes differentiation with respect to r. The Christoffel symbols were found to be

$$\Gamma^r_{\alpha\beta} = \begin{pmatrix} \kappa_1\kappa_2 r\mu & 0 & -\kappa_1 \\ 0 & -r/\mu & 0 \\ -\kappa_1 & 0 & 0 \end{pmatrix}, \tag{6.51}$$

$$\Gamma^\theta_{\alpha\beta} = \begin{pmatrix} 0 & r^{-1} & 0 \\ r^{-1} & 0 & -\kappa_2 \\ 0 & -\kappa_2 & 0 \end{pmatrix}, \tag{6.52}$$

$$\Gamma^n_{\alpha\beta} = \begin{pmatrix} \kappa_1\mu & 0 & 0 \\ 0 & \kappa_2 r^2 & 0 \\ 0 & 0 & 0 \end{pmatrix}, \tag{6.53}$$

where $\kappa_1 = \frac{f''(r)}{\mu^{\frac{3}{2}}}$ and $\kappa_2 = \frac{f'(r)}{r\mu^{\frac{1}{2}}}$ denotes the first and second principal curvature, respectively. Inserting this into the Usadel equation we get

$$iD_F(\mu^{-1}\partial_r(\hat{g}^R\partial_r\hat{g}^R) + r^{-2}\partial_\theta(\hat{g}^R\partial_\theta\hat{g}^R) + ((r\mu)^{-1} - \kappa_1\kappa_2 r)\hat{g}^R\partial_r\hat{g}^R) = [E\hat{\tau}_z + g^{ii}h_i\hat{\sigma}_i, \hat{g}^R]. \tag{6.54}$$

Writing this in the spin-parameterized weak proximity limit form, we take care to write an extra step in the derivation of the three d-vector equations. For the d_r component we get

$$\begin{aligned} &g^{rr}\partial_r^2 d_r + g^{\theta\theta}\partial_\theta^2 d_r - 3g^{rr}\Gamma^r_{rr}\partial_r d_r - 2g^{\theta\theta}\Gamma^\theta_{\theta r}\partial_\theta d_\theta - 2g^{rr}\Gamma^n_{rr}\partial_r d_n - g^{\theta\theta}\Gamma^r_{\theta\theta}\partial_r d_r \\ &- d_r(g^{rr}\partial_r\Gamma^r_{rr} - g^{rr}\Gamma^r_{rr}\Gamma^r_{rr} - g^{\theta\theta}\Gamma^r_{\theta\theta}\Gamma^\theta_{\theta r} - g^{rr}\Gamma^r_{rn}\Gamma^n_{rr} - \Gamma^r_{rr}(g^{rr}\Gamma^r_{rr} + g^{\theta\theta}\Gamma^r_{\theta\theta})) \\ &- d_n(g^{rr}\partial_r\Gamma^n_{rr} - g^{rr}\Gamma^n_{rr}\Gamma^r_{rr} - g^{\theta\theta}\Gamma^n_{\theta\theta}\Gamma^\theta_{\theta r} - \Gamma^n_{rr}(g^{rr}\Gamma^r_{rr} + g^{\theta\theta}\Gamma^r_{\theta\theta})) \\ &= -2i(Ed_r + f_0 h_r), \end{aligned} \tag{6.55}$$

for the d_θ component we get

$$\begin{aligned} &g^{rr}\partial_r^2 d_\theta + g^{\theta\theta}\partial_\theta^2 d_\theta - 2g^{\theta\theta}\Gamma^r_{\theta\theta}\partial_\theta d_r - 2g^{rr}\Gamma^\theta_{r\theta}\partial_r d_\theta - 2g^{\theta\theta}\Gamma^n_{\theta\theta}\partial_\theta d_\theta - (g^{rr}\Gamma^r_{rr} + g^{\theta\theta}\Gamma^r_{\theta\theta})\partial_r d_\theta \\ &- d_\theta(g^{rr}\partial_r\Gamma^\theta_{r\theta} - g^{\theta\theta}\Gamma^\theta_{\theta r}\Gamma^r_{\theta\theta} - g^{rr}\Gamma^\theta_{r\theta}\Gamma^\theta_{r\theta} - g^{\theta\theta}\Gamma^\theta_{\theta n}\Gamma^n_{\theta\theta} - \Gamma^\theta_{r\theta}(g^{rr}\Gamma^r_{rr} + \Gamma^r_{\theta\theta})) \\ &= -2i(Ed_\theta + f_0 h_\theta), \end{aligned} \tag{6.56}$$

and for the d_n component we get

$$\begin{aligned} &g^{rr}\partial_r^2 d_n + g^{\theta\theta}\partial_\theta^2 d_n - 2g^{rr}\Gamma^r_{rn}\partial_r d_r - 2g^{\theta\theta}\Gamma^\theta_{\theta n}\partial_\theta d_\theta - (g^{rr}\Gamma^r_{rr} + g^{\theta\theta}\Gamma^r_{\theta\theta})\partial_r d_n \\ &- d_r(g^{rr}\partial_r\Gamma^r_{rn} - g^{rr}\Gamma^r_{rr}\Gamma^r_{rn} - \Gamma^r_{rn}(g^{rr}\Gamma^r_{rr} + \Gamma^r_{\theta\theta})) - d_n(-g^{rr}\Gamma^n_{rr}\Gamma^r_{rn} - g^{\theta\theta}\Gamma^n_{\theta\theta}\Gamma^\theta_{\theta n}) \\ &= -2i(Ed_\theta + f_0 h_\theta). \end{aligned} \tag{6.57}$$

Inserting the Christoffel symbols into these expressions, we get

$$\begin{aligned} &\mu^{-1}\partial_r^2 d_r + r^{-2}\partial_\theta^2 d_r + ((r\mu)^{-1} - 3\kappa_1\kappa_2 r)\partial_r d_r - 2r^{-3}\partial_\theta d_\theta - 2\kappa_1\partial_r d_n \\ &- d_r(f'''\kappa_2 r\mu^{-\frac{1}{2}} - 4\mu r^2(\kappa_1\kappa_2)^2 + \kappa_1^2(\mu+1) + (\mu r^2)^{-1} + \kappa_1\kappa_2) \\ &- d_n(f'''\mu^{-\frac{3}{2}} - 3\mu r(\kappa_1\kappa_2)^2 + r^{-1}(\kappa_1 - \kappa_2)) = -2i(Ed_r + f_0 h_r) \end{aligned} \tag{6.58}$$

for the d_r component,

$$\begin{aligned} &\mu^{-1}\partial_r^2 d_\theta + r^{-2}\partial_\theta^2 d_\theta - 2\mu^{-\frac{1}{2}}(\nabla\times\boldsymbol{d})\cdot\hat{\mathcal{N}} + ((r\mu)^{-1} - \kappa_1\kappa_2 r)\partial_r d_\theta - 2\kappa_2\partial_\theta d_\theta + d_\theta(\kappa_1\kappa_2 - \kappa_2^2) \\ &= -2i(Ed_\theta + f_0 h_\theta) \end{aligned} \tag{6.59}$$

for the d_θ component, and

$$\begin{aligned} &\mu^{-1}\partial_r^2 d_n + r^{-2}\partial_\theta^2 d_n + 2\mu^{-1}\kappa_1\partial_r d_r - 2r^{-2}\kappa_2\partial_\theta d_\theta + ((r\mu)^{-1} - \kappa_1\kappa_2 r)\partial_r d_n \\ &- d_r(5r\kappa_1^2\kappa_2 - f'''\mu^{-\frac{5}{2}} - \kappa_1(r\mu)^{-1}) - d_n(\kappa_1^2 + \kappa_2^2) = -2i(Ed_n + f_0 h_n) \end{aligned} \tag{6.60}$$

for the d_n component. As we see from these expressions, the transport in this system depends mainly on the principal curvatures, as expected. We have plotted the principal curvatures on a surface with a Gaussian bump in figure 6.6 to display what these curvatures might look like on a surface. Furthermore, the Gaussian bump surface is a popular choice for 2D curvatures [97] [37] [46]. This type of surface is therefore an interesting candidate for further studies.

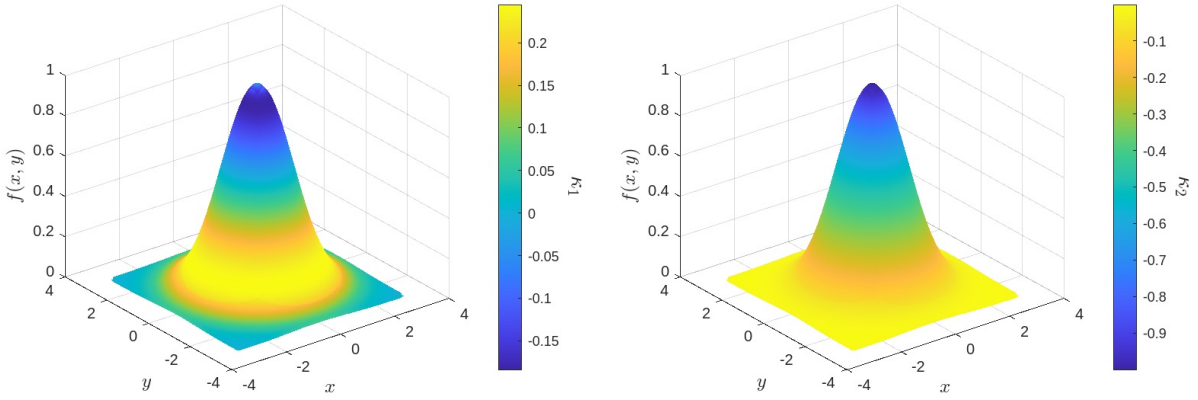

(a) (b)

Figure 6.6: The value of the principal curvatures (a) κ_1 and (b) κ_2 on a surface featuring a Gaussian bump.

7 Summary and outlook

We have demonstrated that curvature has the potential to alter the transport of superconducting correlations in superconductor-ferromagnet systems through spin mixing and spin rotation. The effects of curvature on the systems were shown to be comparable to spin-orbit coupling and a spatially rotating exchange field. We saw that curvature acts as a friction force in the system. Hence, in a wire with constant curvature, increasing the curvature beyond a certain critical value was shown to decrease the coherence length of the long-range triplets, in the ferromagnet. We also demonstrated a curvature driven 0-π transition in a constantly curved SFS Josephson junction.

In order to further the theoretical studies of curved SF proximity systems, we developed a formalism for diffusive transport on 2D curved SF systems using differential geometry. This formalism proved to be different, but analogous to the curvilinear formalism. The main difference from the curvilinear formalism was seen to be the introduction of a second, independent curvature-direction. Hence, we saw that 2D surfaces described by a single, non-varying curvature yielded no new qualitative behaviour with respect to transport of superconducting correlations. We analyzed the SFS boomerang system analytically and numerically. The analytical analysis indicated the possibility of having a 0-π transition along the normal direction of the curvature. This was supported by our numerical simulations, in which we saw that the current changed sign along the normal direction along the curvature. In the same plot, a vortex in the current was observed, indicating the possibility of having curvature induced superconducting vortices. In the boomerang system, the current was seen to be strongest along the inner curvature of the surface. The numerical results for the boomerang system were seen to be unphysical along the superconductor/ferromagnet interfaces, indicating a coding-error in the boundary conditions. Because of this, care should be taken when interpreting the numerical results for this system.

There are many possibilities for future studies of 2D curved SF proximity systems. Many of these possibilities include considering new types of 2D surfaces. For example, a natural continuation of our analytical treatment of the isotropic bump surface would be to solve this system numerically. This could be done for a single Gaussian or cosine bump, or an array of such bumps. Examining the charge current density and direction in such a system could give us more insight into the superconducting correlations' choice of geodesics. This system could also give rise to superconducting vortices. Another natural continuation of this thesis is to write a better code for the boomerang system. The boomerang surface should be studied under a wider array of parameters, and for more physical observables, than considered in this thesis. This would give a better understanding of the dynamics in this system, and possibly shed light on new mechanisms. The systems mentioned could also be studied under an external magnetic field, which could give rise to superconducting vortices and skyrmions, per instance.

In this thesis, the numerical computation of the different geometries was done by mapping these geometries to a rectangular surface and encapsulating the effects of the geometry in the metric and Christoffel symbols. Because of this, we do not lose or alter any information about the system, and our simulations are equivalent to the physical geometries in question. This should be verified by computing the same geometries without mapping them to simplifying geometries, and checking that this yields the same results. Simulating the systems this way, in their true geometry, is made possible by using the finite element method to solve the PDEs.

This thesis has served as an introduction to curved SF proximity systems in 2D. We have seen evidence that curvature is an interesting property in 1D systems, with several theoretical applications, and demonstrated that 2D curvature has the same potential. The unexplored possibilities are therefore manifold for these systems, and hopefully this area of research will receive further attention in the future to come.

Bibliography

[1]P. Quincey, "Natural units in physics, and the curious case of the radian", Physics Education **51**, 065012 (2016).

[2]I. Žutić, J. Fabian, and S. D. Sarma, "Spintronics: fundamentals and applications", Reviews of modern physics **76**, 323 (2004).

[3]A. Aharoni, *Introduction to the theory of ferromagnetism*, Vol. 109 (Clarendon Press, 2000).

[4]C. Kittel and P. McEuen, *Introduction to solid state physics* (John Wiley & Sons, 2018).

[5]S. Thompson, "Magnetoresistive heads: physical phenomena", Encyclopedia of materials: science and technology, 5095 (2001).

[6]M. N. Baibich, J. M. Broto, A. Fert, F. N. Van Dau, F. Petroff, P. Etienne, G. Creuzet, A. Friederich, and J. Chazelas, "Giant magnetoresistance of (001) fe/(001) cr magnetic superlattices", Physical review letters **61**, 2472 (1988).

[7]K. v. Klitzing, G. Dorda, and M. Pepper, "New method for high-accuracy determination of the fine-structure constant based on quantized hall resistance", Physical review letters **45**, 494 (1980).

[8]X.-L. Qi and S.-C. Zhang, "The quantum spin hall effect and topological insulators", Physics Today **63**, 33 (2010).

[9]S. S. Parkin, M. Hayashi, and L. Thomas, "Magnetic domain-wall racetrack memory", science **320**, 190 (2008).

[10]J. Linder and J. W. Robinson, "Superconducting spintronics", Nature Physics **11**, 307 (2015).

[11]S. H. Jacobsen, J. A. Ouassou, and J. Linder, "Critical temperature and tunneling spectroscopy of superconductor-ferromagnet hybrids with intrinsic rashba-dresselhaus spin-orbit coupling", Physical Review B **92**, 024510 (2015).

[12]A. Mazanik and I. Bobkova, "Supercurrent-induced long-range triplet correlations and controllable josephson effect in superconductor/ferromagnet hybrids with extrinsic spin-orbit coupling", Physical Review B **105**, 144502 (2022).

[13]A. Samokhvalov, J. Robinson, and A. Buzdin, "Long-range triplet proximity effect in multiply connected ferromagnet-superconductor hybrids", Physical Review B **100**, 014509 (2019).

[14]H. K. Onnes, "Further experiments with liquid helium. c. on the change of electric resistance of pure metals at very low temperatures etc. iv. the resistance of pure mercury at helium temperatures", in Knaw, proceedings, Vol. 13 (1911), pp. 1910–1911.

[15]S. Hahn, K. Kim, K. Kim, X. Hu, T. Painter, I. Dixon, S. Kim, K. R. Bhattarai, S. Noguchi, J. Jaroszynski, et al., "45.5-tesla direct-current magnetic field generated with a high-temperature superconducting magnet", Nature **570**, 496 (2019).

[16]B. D. Josephson, "Possible new effects in superconductive tunnelling", Physics letters **1**, 251 (1962).

[17]A. Schilling, M. Cantoni, J. Guo, and H. Ott, "Superconductivity above 130 k in the hg–ba–ca–cu–o system", Nature **363**, 56 (1993).

[18]A. K. Saxena, *High-temperature superconductors*, Vol. 125 (Springer Science & Business Media, 2012).

[19]M. Cyrot, "Ginzburg-landau theory for superconductors", Reports on Progress in Physics **36**, 103 (1973).

[20]J. Bardeen, L. N. Cooper, and J. R. Schrieffer, "Microscopic theory of superconductivity", Physical Review **106**, 162 (1957).

[21]P. W. Anderson, "The resonating valence bond state in la2cuo4 and superconductivity", science **235**, 1196 (1987).

[22]S. Kivelson and D. Rokhsar, "Bogoliubov quasiparticles, spinons, and spin-charge decoupling in superconductors", Physical Review B **41**, 11693 (1990).

[23]T. Hashimoto, Y. Ota, A. Tsuzuki, T. Nagashima, A. Fukushima, S. Kasahara, Y. Matsuda, K. Matsuura, Y. Mizukami, T. Shibauchi, et al., "Bose-einstein condensation superconductivity induced by disappearance of the nematic state", Science Advances **6**, eabb9052 (2020).

[24]M. Tinkham, *Introduction to superconductivity* (Courier Corporation, 2004).

[25]R. Holm and W. Meissner, "Messungen mit hilfe von flüssigem helium. xiii: kontaktwiderstand zwischen supraleitern und nichtsupraleitern", Zeitschrift für Physik **74**, 715 (1932).

[26]Y. Asano, *Andreev reflection in superconducting junctions* (Springer, 2021).

[27]M. Eschrig, "Spin-polarized supercurrents for spintronics: a review of current progress", Reports on Progress in Physics **78**, 104501 (2015).

[28]A. I. Buzdin, "Proximity effects in superconductor-ferromagnet heterostructures", Reviews of modern physics **77**, 935 (2005).

[29]M. Eschrig, "Spin-polarized supercurrents for spintronics", Physics Today **64**, 43 (2011).

[30]F. Bergeret, A. F. Volkov, and K. B. Efetov, "Odd triplet superconductivity and related phenomena in superconductor-ferromagnet structures", Reviews of modern physics **77**, 1321 (2005).

[31]J. Linder and A. V. Balatsky, "Odd-frequency superconductivity", Reviews of Modern Physics **91**, 045005 (2019).

[32]R. S. Keizer, S. T. Goennenwein, T. M. Klapwijk, G. Miao, G. Xiao, and A. Gupta, "A spin triplet supercurrent through the half-metallic ferromagnet cro2", Nature **439**, 825 (2006).

[33]F. Bergeret and I. Tokatly, "Spin-orbit coupling as a source of long-range triplet proximity effect in superconductor-ferromagnet hybrid structures", Physical Review B **89**, 134517 (2014).

[34]T. Salamone, H. G. Hugdal, M. Amundsen, and S. H. Jacobsen, "Curvature control of the superconducting proximity effect in diffusive ferromagnetic nanowires", Physical Review B **105**, 134511 (2022).

[35]V. M. Fomin, R. O. Rezaev, and O. G. Schmidt, "Tunable generation of correlated vortices in open superconductor tubes", Nano letters **12**, 1282 (2012).

[36]R. Rezaev, E. Smirnova, O. Schmidt, and V. Fomin, "Topological transitions in superconductor nanomembranes under a strong transport current", Communications Physics **3**, 144 (2020).

[37]D. Makarov, O. M. Volkov, A. Kákay, O. V. Pylypovskyi, B. Budinská, and O. V. Dobrovolskiy, "New dimension in magnetism and superconductivity: 3d and curvilinear nanoarchitectures", Advanced Materials **34**, 2101758 (2022).

[38]O. V. Pylypovskyi, D. Y. Kononenko, K. V. Yershov, U. K. Rößler, A. V. Tomilo, J. Fassbender, J. van den Brink, D. Makarov, and D. D. Sheka, "Curvilinear one-dimensional antiferromagnets", Nano Letters **20**, 8157 (2020).

[39]O. Pylypovskyi, Y. Borysenko, A. Tomilo, D. Kononenko, K. Yershov, U. Roessler, J. Fassbender, J. van den Brink, D. Sheka, and D. Makarov, "Effects of geometry on antiferromagnetic textures: boundaries and geometric curvature", in Aps march meeting abstracts, Vol. 2023 (2023), SS01–016.

[40]P. Gentile, M. Cuoco, O. M. Volkov, Z.-J. Ying, I. J. Vera-Marun, D. Makarov, and C. Ortix, "Electronic materials with nanoscale curved geometries", Nature Electronics **5**, 551 (2022).

[41]Z.-J. Ying, M. Cuoco, C. Ortix, and P. Gentile, "Tuning pairing amplitude and spin-triplet texture by curving superconducting nanostructures", Physical Review B **96**, 100506 (2017).

[42]G. Francica, M. Cuoco, and P. Gentile, "Topological superconducting phases and josephson effect in curved superconductors with time reversal invariance", Physical Review B **101**, 094504 (2020).

[43]O. V. Pylypovskyi, D. D. Sheka, V. P. Kravchuk, K. V. Yershov, D. Makarov, and Y. Gaididei, "Rashba torque driven domain wall motion in magnetic helices", Scientific Reports **6**, 23316 (2016).

[44]K. V. Yershov, V. P. Kravchuk, D. D. Sheka, and Y. Gaididei, "Curvature and torsion effects in spin-current driven domain wall motion", Physical Review B **93**, 094418 (2016).

[45]J. A. Otálora, M. Yan, H. Schultheiss, R. Hertel, and A. Kákay, "Curvature-induced asymmetric spin-wave dispersion", Physical review letters **117**, 227203 (2016).

[46]V. P. Kravchuk, D. D. Sheka, A. Kákay, O. M. Volkov, U. K. Rößler, J. van den Brink, D. Makarov, and Y. Gaididei, "Multiplet of skyrmion states on a curvilinear defect: reconfigurable skyrmion lattices", Physical Review Letters **120**, 067201 (2018).

[47]X. Huo and Y. Liu, "The stability of a skyrmion in a nanotube", New Journal of Physics **21**, 093024 (2019).

[48]G. Williams, M. Hunt, B. Boehm, A. May, M. Taverne, D. Ho, S. Giblin, D. Read, J. Rarity, R. Allenspach, et al., "Two-photon lithography for 3d magnetic nanostructure fabrication", Nano Research **11**, 845 (2018).

[49]O. M. Volkov, A. Kákay, F. Kronast, I. Mönch, M.-A. Mawass, J. Fassbender, and D. Makarov, "Experimental observation of exchange-driven chiral effects in curvilinear magnetism", Physical Review Letters **123**, 077201 (2019).

[50]T. Salamone, "Proximity effects in nanostructures with geometric curvature for superconducting spintronics", PhD thesis (2023).

[51]T. Salamone, H. G. Hugdal, M. Amundsen, and S. H. Jacobsen, "Electrical control of superconducting spin valves using ferromagnetic helices", arXiv preprint arXiv:2404.05798 (2024).

[52]T. Salamone, M. Skjærpe, H. G. Hugdal, M. Amundsen, and S. H. Jacobsen, "Interface probe for antiferromagnets using geometric curvature", Physical Review B **109**, 094508 (2024).

[53]A. J. Skarpeid, H. G. Hugdal, T. Salamone, M. Amundsen, and S. H. Jacobsen, "Non-constant geometric curvature for tailored spin-orbit coupling and chirality in superconductor-magnet heterostructures", Journal of Physics: Condensed Matter (2024).

[54]T. Salamone, M. B. Svendsen, M. Amundsen, and S. Jacobsen, "Curvature-induced long-range supercurrents in diffusive superconductor-ferromagnet-superconductor josephson junctions with a dynamic 0- π transition", Physical Review B **104**, L060505 (2021).

[55]K. D. Usadel, "Generalized diffusion equation for superconducting alloys", Physical Review Letters **25**, 507 (1970).

[56]M. Amundsen and J. Linder, "General solution of 2d and 3d superconducting quasiclassical systems: coalescing vortices and nanoisland geometries", Scientific Reports **6**, 22765 (2016).

[57]M. Alidoust and K. Halterman, "Proximity induced vortices and long-range triplet supercurrents in ferromagnetic josephson junctions and spin valves", Journal of Applied Physics **117** (2015).

[58]P. Lai, G. Zhao, H. Tang, N. Ran, S. Wu, J. Xia, X. Zhang, and Y. Zhou, "An improved racetrack structure for transporting a skyrmion", Scientific reports **7**, 1 (2017).

[59]A. V. Ramallo, "Introduction to the ads/cft correspondence", in Lectures on particle physics, astrophysics and cosmology: proceedings of the third idpasc school, santiago de compostela, spain, january 21–february 2, 2013 (Springer, 2015), pp. 411–474.

[60]E. H. Fyhn and J. Linder, "Superconducting vortices in half-metals", Physical Review B **100**, 224508 (2019).

[61]V. Chandrasekhar, "Proximity-coupled systems: quasiclassical theory of superconductivity", The Physics of Superconductors: Vol. II. Superconductivity in Nanostructures, High-T c and Novel Superconductors, Organic Superconductors, 55 (2004).

[62]A. L. Fetter and J. D. Walecka, *Quantum theory of many-particle systems* (Courier Corporation, 2012).

[63]J. A. Ouassou, "Density of states and critical temperature in superconductor/ferromagnet structures with spin-orbit coupling", Master's thesis (NTNU, 2015).

[64]N. Ptitsina, G. Chulkova, K. Il'in, A. Sergeev, F. Pochinkov, E. Gershenzon, and M. Gershenson, "Electron-phonon interaction in disordered metal films: the resistivity and electron dephasing rate", Physical Review B **56**, 10089 (1997).

[65]J. P. Morten, "Spin and charge transport in dirty superconductors", Norwegian University of Science and Technology (2005).

[66]M. Amundsen, "Quasiclassical theory beyond 1d: supercurrents and topological excitations", Master's thesis (NTNU, 2016).

[67]M. B. M. Svendsen, "Curvature in superconductor-ferromagnet structures", Master's thesis (NTNU, 2021).

[68]G. Eilenberger, "Transformation of gorkov's equation for type ii superconductors into transport-like equations", Zeitschrift für Physik A Hadrons and nuclei **214**, 195 (1968).

[69]J.-X. Zhu, *Bogoliubov-de gennes method and its applications*, Vol. 924 (Springer, 2016).

[70]L. Tagirov and N. García, "Quasiclassical boundary conditions for a contact of two metals", Superlattices and Microstructures **41**, 152 (2007).

[71]Y. V. Nazarov, "Novel circuit theory of andreev reflection", Superlattices and microstructures **25**, 1221 (1999).

[72]P. Fulde and R. A. Ferrell, "Superconductivity in a strong spin-exchange field", Physical Review **135**, A550 (1964).

[73]A. Larkin and Y. N. Ovchinnikov, "Nonuniform state of superconductors", Soviet Physics-JETP **20**, 762 (1965).

[74]F. Bergeret, A. Volkov, and K. Efetov, "Long-range proximity effects in superconductor-ferromagnet structures", Physical review letters **86**, 4096 (2001).

[75]I. Sosnin, H. Cho, V. Petrashov, and A. Volkov, "Superconducting phase coherent electron transport in proximity conical ferromagnets", Physical review letters **96**, 157002 (2006).

[76]D. J. Griffiths, *Introduction to electrodynamics* (Cambridge University Press, 2023).

[77]Y. A. Bychkov and E. I. Rashba, "Oscillatory effects and the magnetic susceptibility of carriers in inversion layers", Journal of physics C: Solid state physics **17**, 6039 (1984).

[78]G. Dresselhaus, "Spin-orbit coupling effects in zinc blende structures", Physical Review **100**, 580 (1955).

[79]M. Sigrist and K. Ueda, "Phenomenological theory of unconventional superconductivity", Reviews of Modern physics **63**, 239 (1991).

[80]F. S. Bergeret and I. V. Tokatly, "Singlet-triplet conversion and the long-range proximity effect in superconductor-ferromagnet structures with generic spin dependent fields", Phys. Rev. Lett. **110**, 117003 (2013).

[81]S. H. Jacobsen and J. Linder, "Giant triplet proximity effect in π-biased josephson junctions with spin-orbit coupling", Physical Review B **92**, 024501 (2015).

[82]W. Belzig, C. Bruder, and G. Schön, "Local density of states in a dirty normal metal connected to a superconductor", Physical Review B **54**, 9443 (1996).

[83]D. D. Sheka, V. P. Kravchuk, and Y. Gaididei, "Curvature effects in statics and dynamics of low dimensional magnets", Journal of Physics A: Mathematical and Theoretical **48**, 125202 (2015).

[84]D. E. Neuenschwander, *Tensor calculus for physics*, Vol. 422 (John Hopkins University Press, 2014).

[85]M. Ricci and T. Levi-Civita, "Méthodes de calcul différentiel absolu et leurs applications", Mathematische Annalen **54**, 125 (1900).

[86]T. Levi-Civita, *The absolute differential calculus (calculus of tensors)* (Courier Corporation, 1977).

[87]A. N. Pressley, *Elementary differential geometry* (Springer Science & Business Media, 2010).

[88]J. Bardeen and W. Shockley, "Deformation potentials and mobilities in non-polar crystals", Physical review **80**, 72 (1950).

[89]C. G. Van de Walle and R. M. Martin, "Theoretical calculations of heterojunction discontinuities in the si/ge system", Physical Review B **34**, 5621 (1986).

[90]M. Amundsen, "Proximity effects in superconducting hybrid structures with spin-dependent interactions", PhD thesis (2020).

[91]M. Alidoust, G. Sewell, and J. Linder, "Non-fraunhofer interference pattern in inhomogeneous ferromagnetic josephson junctions", Physical Review Letters **108**, 037001 (2012).

[92]A. R. Mitchell and D. F. Griffiths, "The finite difference method in partial differential equations", A Wiley-Interscience Publication (1980).

[93]R. D. Cook et al., *Concepts and applications of finite element analysis* (John wiley & sons, 2007).

[94]R. Eymard, T. Gallouët, and R. Herbin, "Finite volume methods", Handbook of numerical analysis **7**, 713 (2000).

[95]T. J. Ypma, "Historical development of the newton–raphson method", SIAM review **37**, 531 (1995).

[96]M. H. Stone, "The generalized weierstrass approximation theorem", Mathematics Magazine **21**, 237 (1948).

[97]K. V. Silva, C. F. de Freitas, and C. Filgueiras, "Geometry-induced quantum dots on surfaces with gaussian bumps", The European Physical Journal B **86**, 1 (2013).

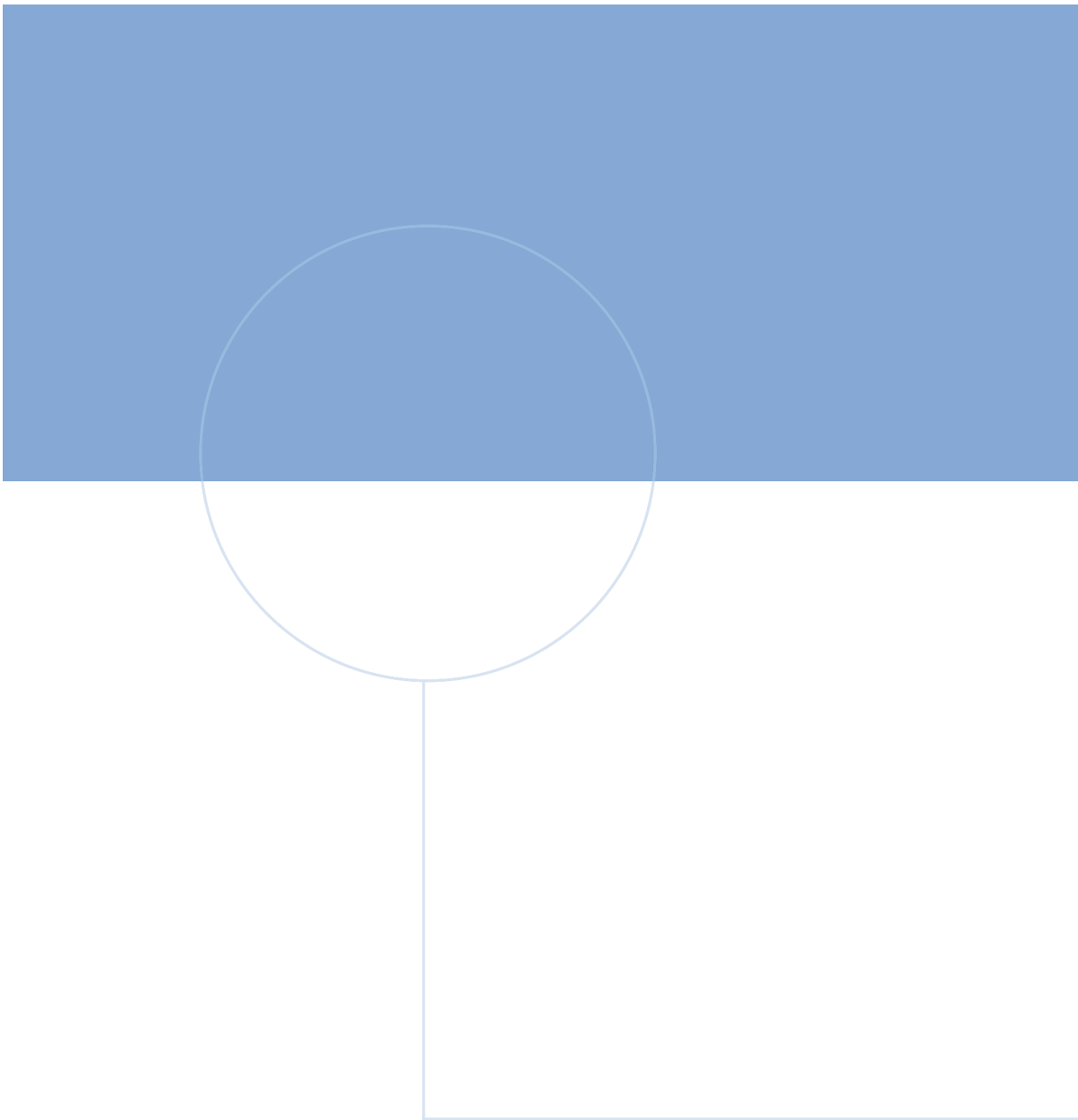

NTNU

Norwegian University of
Science and Technology